UNCLASSIFIED

AD NUMBER
AD483838
LIMITATION CHANGES
TO: **Approved for public release; distribution is unlimited.**
FROM: **Distribution authorized to U.S. Gov't. agencies and their contractors; Critical Technology; 08 DEC 1965. Other requests shall be referred to Air Force Technical Applications Center, Patrick AFB, FL 32925. This document contains export-controlled technical data.**
AUTHORITY
USAF ltr, 25 Jan 1972

THIS PAGE IS UNCLASSIFIED

TR 65-127

TECHNICAL REPORT NO. 65-127

DIGITAL EVALUATION OF A CALIBRATION TECHNIQUE FOR MULTIPLE-ELEMENT ARRAY SYSTEMS

TELEDYNE INDUSTRIES
GEOTECH DIVISION
GARLAND TEXAS

TECHNICAL REPORT NO. 65-127

DIGITAL EVALUATION OF A CALIBRATION TECHNIQUE FOR MULTIPLE-ELEMENT ARRAY SYSTEMS

by

Y. T. Huang

TELEDYNE INDUSTRIES
GEOTECH DIVISION
3401 Shiloh Road
Garland, Texas

8 December 1965

IDENTIFICATION

AFTAC Project No. VT/4051
Project Title: Long-Range Seismic Measurements
ARPA Order No: 104-60
ARPA Code No: 8100
Contractor: Teledyne Industries, Geotech Division
Date of Contract: 1 July 1965
Amount of Contract: $1, 115, 000
Contract No: AF 33(657)-12145, Supplemental Agreement No. 4
Contract Expiration Date: 31 December 1965
Program Manager: R. D. Wolfe, phone 214 278-8102

CONTENTS

ILLUSTRATIONS

ILLUSTRATIONS, Continued

ILLUSTRATIONS, Continued

ILLUSTRATIONS, Continued

ILLUSTRATIONS, Continued

ILLUSTRATIONS, Continued

ILLUSTRATIONS, Continued

ABSTRACT

A quantitative analysis is made using techniques of digital spectral analysis. Two different approaches are compared -- statistical and deterministic.

For the statistical approach, the computer program "BLACKY," which computes power density spectra, was adopted. A program which uses the Numerical Transform Theorem (Huang, 1965a) was written for the CDC 160A digital computer. This program, "NUTRAN," relies on a deterministic consideration of a time series.

The agreement between the field calibration and the estimation of the magnification curve is quite good up to 1.5 cps, considering the simplicity of the mathematical model used in our study. Above this frequency, the scatter is quite erratic, and further refinement of the technique is desirable. The reason for this disagreement comes essentially from a lack of the high signal-to-noise ratio which is the basis of our treatment. Our technical success seems to be limited by our ability to discriminate noise which contaminates the signal arrivals.

DIGITAL EVALUATION OF A CALIBRATION TECHNIQUE FOR MULTIPLE-ELEMENT ARRAY SYSTEMS

1. INTRODUCTION

In the previous report (Huang,1965b), we made a qualitative study of a calibration technique (Whalen, 1965) using the Geotech Analog Spectrum Analyzer. It was found that good agreement existed between the estimated and the field calibrated values of the relative magnification curve for frequencies below 1.5 cps. For the higher frequencies, the agreement was poor.

In order that a more quantitative evaluation of the technique could be made, we performed digital analyses. Two different approaches were taken; one was statistical, the other nonstatistical (or deterministic). Since we base our analyses on a high signal-to-noise ratio, a deterministic approach using numerical transforms seems more logical. On the other hand, since we are unable to determine what is really our signal, as it is invariably contaminated by random noise, a statistical method using power density spectra seems quite desirable. Both results are studied in this report.

It so happened that the events studied in the previous report did not fall on the same dates as the end of the month calibrations, which had more calibration information. However, from the day-to-day fluctuation of the motor constant (G), which was found to be within 5%, we construed that end of the month calibration results could be used reliably throughout the month. Since we had both controlled calibration data and a significant signal from an event on June 2, 1965, we concentrated our efforts on this set of data for more quantitative analyses.

The Jerome, Arizona, station (JR-AZ) is situated on the Verde formation, which is primarily a conglomerate of lake desposits consisting of white limestone, gravel, sand, clay, and evaporites. The Z_3 seismometer (figure 1) is on a thin section of a limestone cap which sits on the mesa of the lake deposits. The Z_1, Z_2, Z_6, and Z_7 seismometers are on a fragmented limestone cap approximately 100 feet thick, and the Z_4 and Z_5 seismometers are on a relatively uniform river bed consisting of unconsolidated, incompetent sands, gravels, and clays.

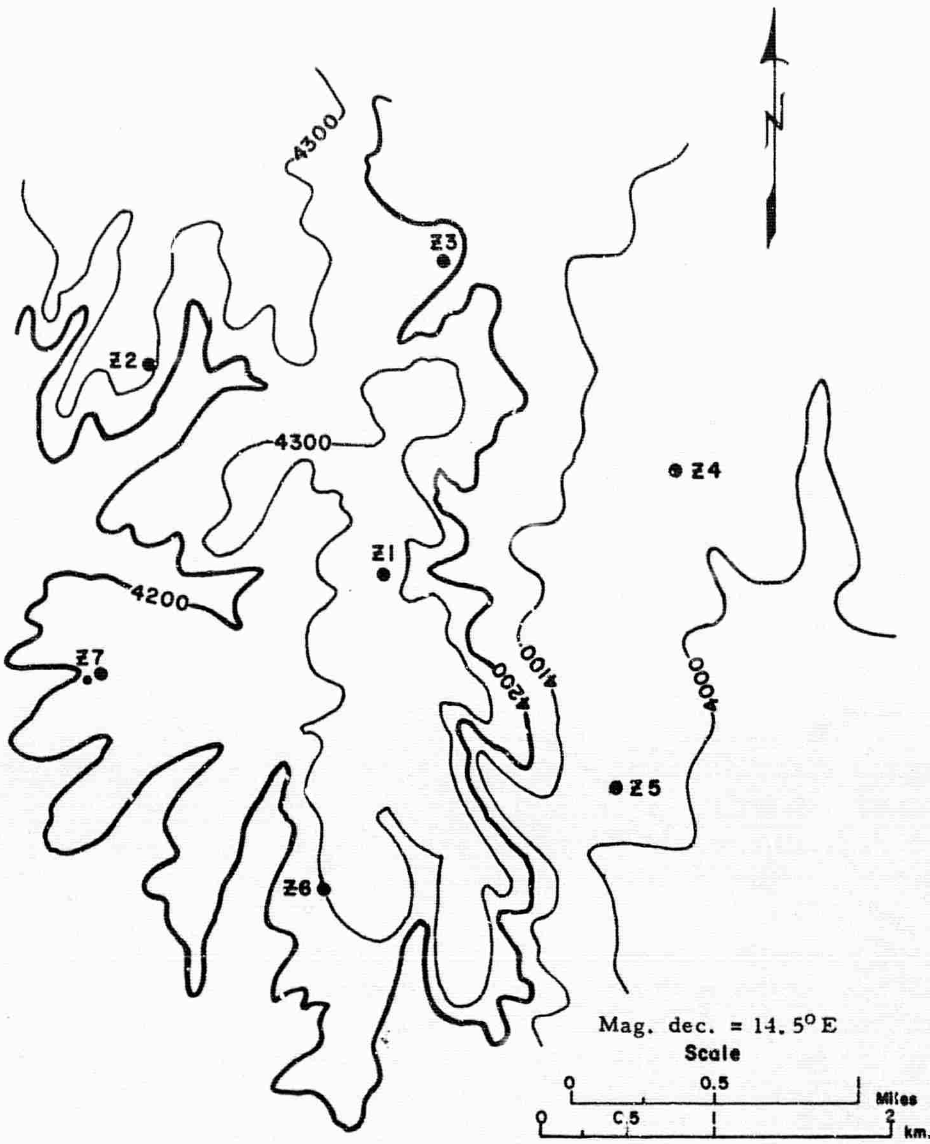

Figure 1. Jerome hexagonal subarray (JR-AZ)

G 342

The Winslow, Arizona, station (WO-AZ) on the other hand, is on the Moenkopi formation which consists of nonmarine, locally gypsiferous, sandy, and silty redbeds interfingering with some calcareous strata. All seven seismometers are situated on this formation (figure 2). These two stations, therefore, made it possible to study the effects of both heterogeneity and homogeneity in local geological structures.

Since our qualitative study indicated the feasibility of taking short record lengths for signal analysis, the current study was confined to 2- and 3-second signal segments. The origin time of the June 2, 1965, Pacific event utilized was 13:57:51z. The epicenter was located at 4.6S, 105.6W (near Northern Easter I. Cordillera) and had a body-wave magnitude (m_b) of 4.8. The epicentral distance from these two stations was approximately 4500 km. which is within the teleseismic window (Carpenter, 1965) for signal transmission.

2. TECHNIQUES OF SPECTRAL ANALYSIS

The mathematical model used for our calibration study was explained in the theoretical considerations of the previous report (Huang, 1965b). The following assumptions were made with regard to our imperfect model:

a. The data contain high signal-to-noise ratios to the extent that noise can be ignored.

b. The effect of dispersion and scattering is very slight from seismograph to seismograph so that station correction for the attenuation is unnecessary.

c. Local geology is isotropic and homogeneous.

The resulting calibration curves are given by

$$A(\omega) = A_c(\omega) \left| \frac{M(\omega)}{M_c(\omega)} \right| , \qquad (1)$$

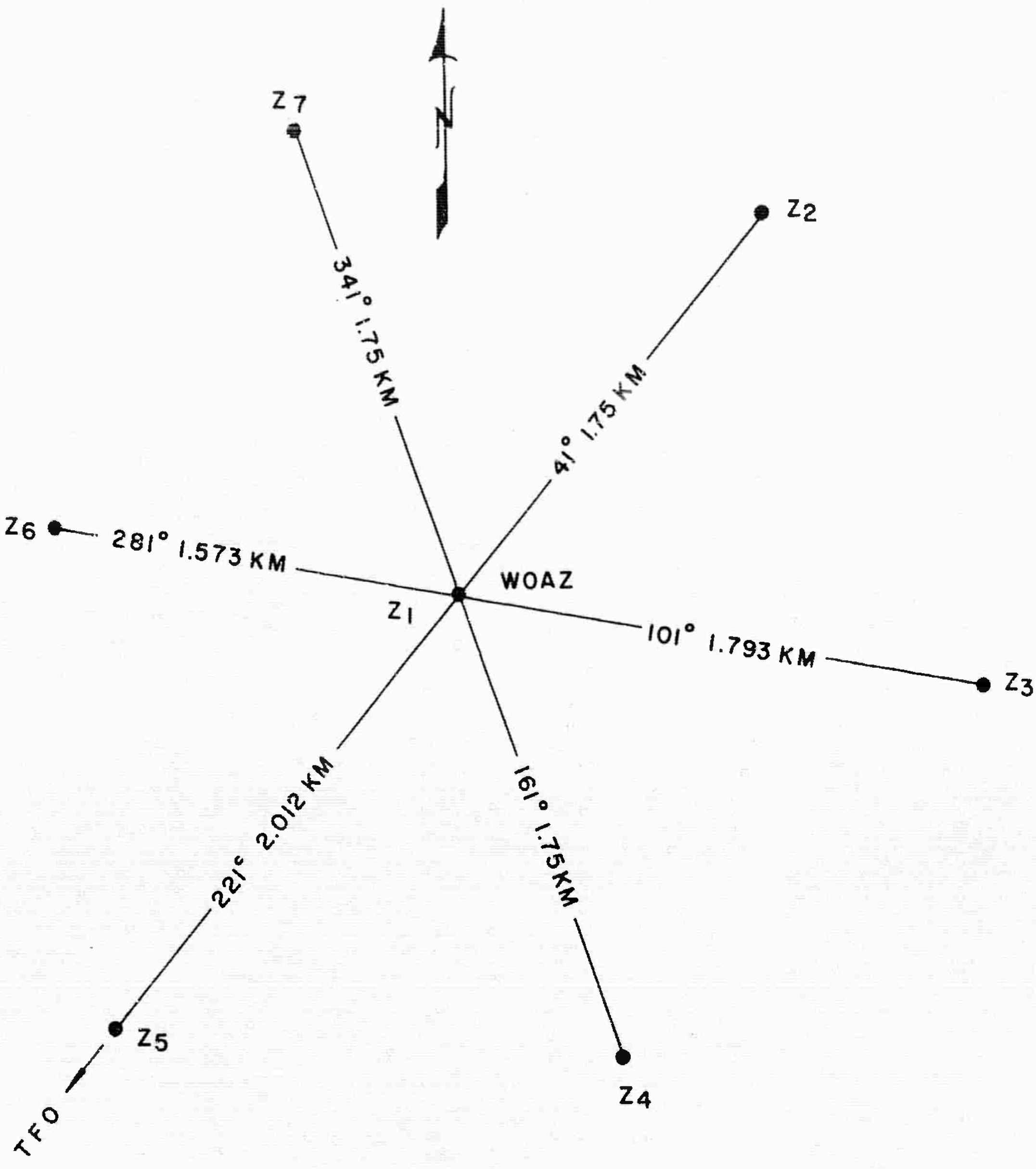

Figure 2. Winslow hexagonal subarray (WO-AZ)

G 343

and

$$B(\omega) = B_c(\omega) + \angle \frac{M(\omega)}{M_c(\omega)} , \qquad (2)$$

where $A(\omega)$ and $B(\omega)$ are the amplitude and phase response curves of the estimated calibration results. $\left| \frac{M(\omega)}{M_c(\omega)} \right|$ and $\angle \frac{M(\omega)}{M_c(\omega)}$ are the amplitude and phase curves of the spectral ratios of the received signals, and $A_c(\omega)$ and $B_c(\omega)$ are the magnification and phase-response curves of the center instrument, which serves as a standard. ω is circular frequency.

From equations (1) and (2), it is obvious that spectral analysis constitutes the core of our evaluation scheme. Digital spectral analysis is used in this report. The magnetic tapes from JR-AZ and WO-AZ, which recorded the Pacific event of June 2, 1965, were digitized using the Geotech digitizing system.

Two computer programs were used; the program "NUTRAN," which performs numerical transforms was written by Paul Kozsuch of Geotech. The program "BLACKY," which was written by personnel of the Seismic Data Laboratory (SDL) of Alexandria, Virginia, performs power dens..y spectral analysis (Blackman and Tukey, 1958). A brief description of these two programs is given below.

2.1 PROGRAM NUTRAN

For a digitized trace of finite length, the numerical transform theorem (Huang, 1965a) can be conveniently applied. This relationship is given by

$$f_i = \frac{1}{m} \sum_{n=0}^{m-1} \sum_{k=0}^{m-1} f_k e^{-j \frac{2\pi n}{m} (k-i)}, \quad i = 0, 1, 2 \text{-----}, m-1, \qquad (3)$$

where j is an imaginary unit.

The relationship is similar to the well-known Fourier Transform Theorem for a continuous function of an infinite length, that is,

$$f(t) = \frac{1}{2\pi} \int_{-\infty}^{\infty} d\omega \int_{-\infty}^{\infty} f(\xi) e^{-j\omega(\xi - t)} d\xi . \tag{4}$$

The complex expression for Fourier analysis is given by

$$f(t) = \sum_{n=-\infty}^{\infty} C'_n e^{-j\frac{\pi n t}{T}} , \tag{5}$$

where the coefficients C'_n are determined by

$$C'_n = \frac{1}{2T} \int_{-T}^{T} f(t) e^{-j\frac{\pi n t}{T}} dt . \tag{6}$$

2T in the expression (6) represents the period.

With a properly chosen digitization rate and filter setup, the digital spectrum can be given by

$$F_n = \frac{1}{m} \sum_{k=0}^{m-1} f_k e^{-j\frac{2\pi n k}{m}} . \tag{7}$$

The frequency spectrum is related to (6) and (7) by

$$F\left(\frac{\omega}{2\pi}\right) = F\left(\frac{n}{2T}\right) = F_n = C'_n \ . \tag{8}$$

Detailed descriptions of the above relationships are given in a separate report (Huang, 1965a). In order to perform a Fourier transform, expression (7) is replaced by

$$F_n = \frac{1}{m} \sum_{i=0}^{m-1} f_k e^{-j\frac{2\pi nk}{m'}} \ , \tag{9}$$

where m' is larger than m.

To perform a spectral stacking, the m' in equation (9) should be taken from a subsection of 2T. The record length 2T and m are related by

$$2T = m\Delta t, \tag{10}$$

where Δt is a digitization increment.

The NUTRAN program listing is contained in Appendix 2. Since a signal is invariably contaminated by random noise, spectral smoothing is performed just before estimation of the calibration results. In order for these results to be comparable to BLACKY outputs, smoothing of the Hanning type (Blackman and Tukey, 1958) is incorporated.

2.2 PROGRAM BLACKY

This program computes power density spectra through Fourier transform of the autocorrelation function.

For a digitized time series X_i, the bias-removed autocorrelation function is given by

$$Y(k) = \frac{1}{n-1} \sum_{i=k+1}^{n} X_{i-k} X_i - \frac{1}{(n-1)^2} \sum_{i=k+1}^{n} X_{i-k} \sum_{i=k+1}^{n} X_i . \qquad (11)$$

The power density spectrum is given by

$$F(\omega) = \frac{\delta\omega}{m} \left[\sum_{k=1}^{m-1} 2W(k)Y(k) \cos \frac{\omega k \pi}{m} + Y(0) \right],$$

where

$$\delta\omega = \begin{cases} \frac{1}{2} & \text{for } \omega = 0 \text{ or } m \\ 1 & \text{otherwise} \end{cases} \qquad (12)$$

and

$$2W(k) = 1 + \cos \frac{k\pi}{m} .$$

Expressions (11) and (12) are approximations of the results given in "The Measurement of Power Spectra" (Blackman and Tukey, 1958). W(k) is the lag window.

3. RESULTS OF SPECTRAL ANALYSIS

In figures 3 and 4, playbacks of the Northern Easter Island Cordillera event at JR-AZ and WO-AZ are shown. These signals, together with the noise preceeding them, were digitized at a rate of 25 samples per second with a low-pass filter set at 8 cps and 18 dB per octave attenuation. The folding frequency falls at 12.5 cps.

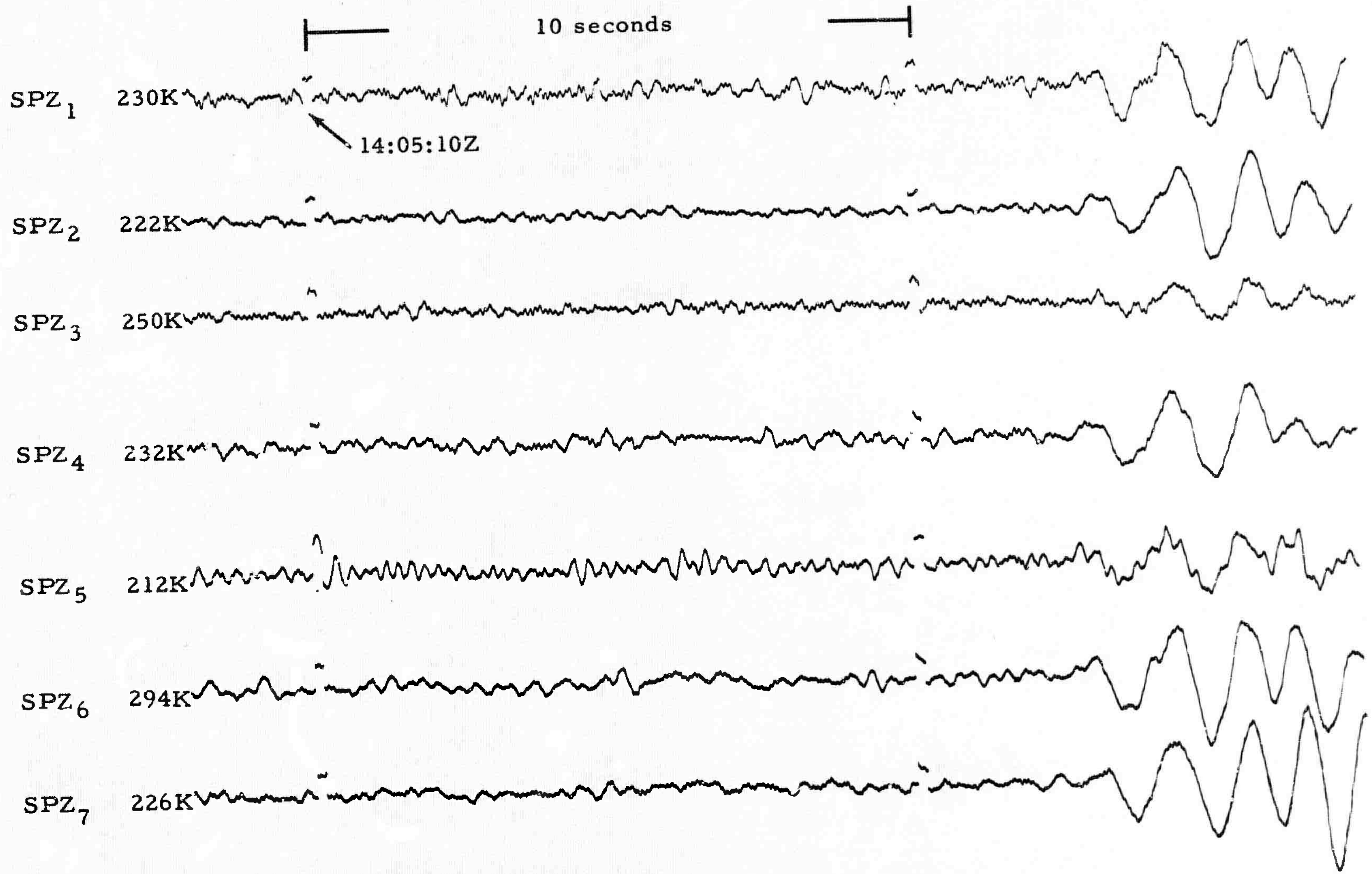

Figure 3. JR-AZ, 2 June 1965. Event from the Northern Easter Island Cordillera. Epicentral data: $\Delta \simeq 39.7^{o}$, $h \simeq 33$km, azimuth $\simeq 170^{o}$, magnitude $\simeq 4.8$

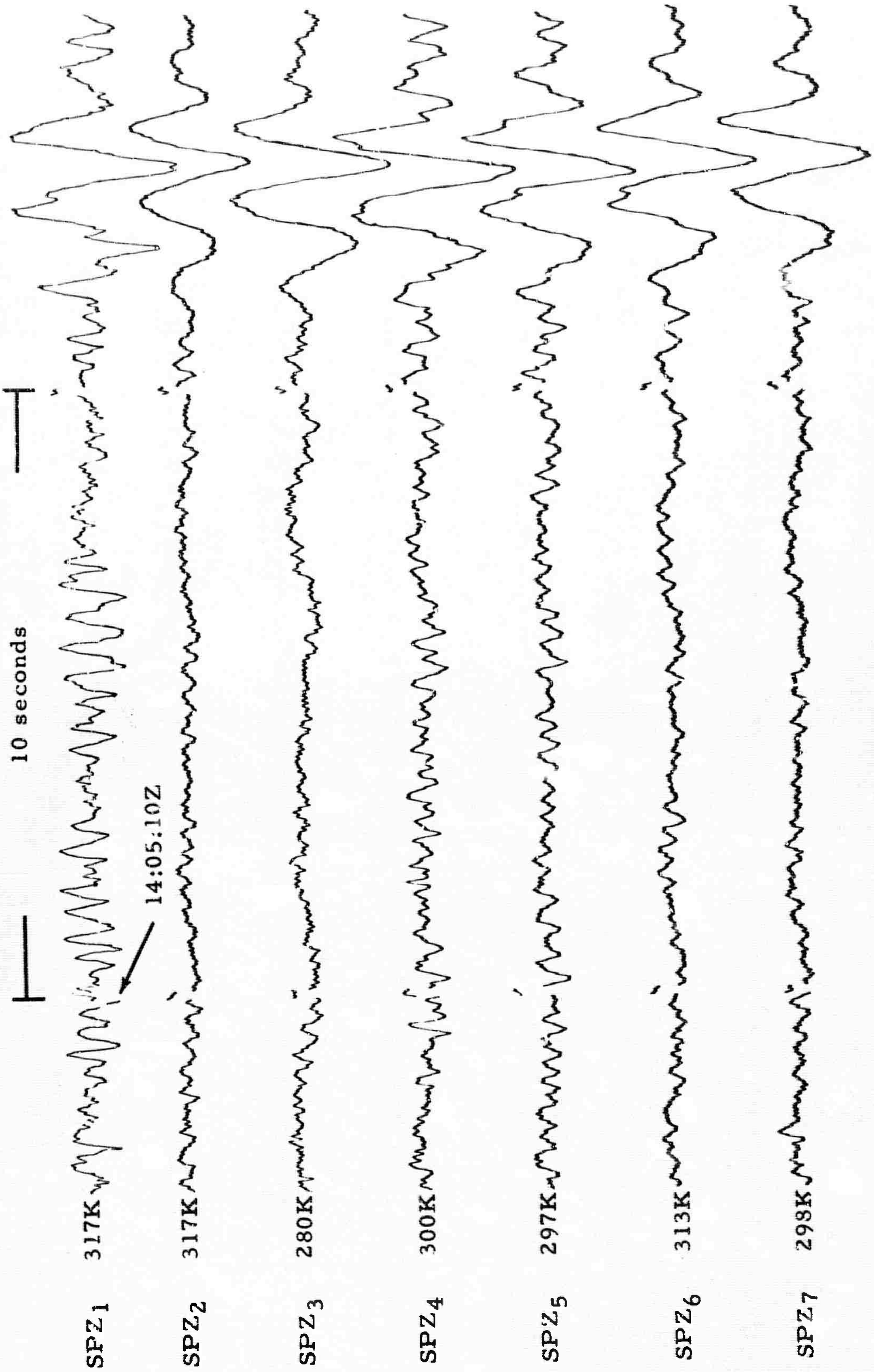

Figure 4. WO-AZ, 2 June 1965. Event from the Northern Easter Island Cordillera.
Epicentral data: $\Delta \approx 39.6^\circ$, $h \approx 33$km, azimuth $\approx 172^\circ$, magnitude ≈ 4.8

For the 2-second (50 samples) cases, a maximum lag of 25 samples was used in computing the power density spectra. We assumed that the received signal had a low noise content, and so tried to improve our resolution at the expense of the confidence level of the power spectrum (Blackman and Tukey, 1958). The maximum lag was changed to 10 samples for the 3-second (75 samples) cases, and this difference is reflected in the output of the BLACKY program.

Figures 5 through 18 are the plotted results of the NUTRAN computations. The corresponding BLACKY results are shown in figures 19 through 32.

4. CALIBRATION RESULTS

Application of formulas (1) and (2), together with the reference calibration curves at the hexagonal subarray centers (Appendix 1), yielded the results shown in figures 33 through 80.

4.1 AMPLITUDE RESPONSE

Both smoothed and unsmoothed cases were studied. As already mentioned in section 2 of this report, Hanning smoothing was applied in the frequency domain for the NUTRAN output. Figures 33 through 44 combine the results of the 2- and 3-second unsmoothed cases and figures 45 through 68 show the 2- and 3-second smoothed cases. In general, the 2-second cases agree better with the field calibrations.

A comparison of smoothed and unsmoothed cases indicates that the smoothed spectra give better results. This is probably due to the random nature of the noise contamination. The BLACKY estimates for the calibration were inferior to the NUTRAN estimates. A possible interpretation of this result is that the deterministic approach is more suited for treating signals.

As previously concluded (Huang, 1965b), the agreement between the estimated and the calibrated results is quite good for frequencies below 1.5 cps; the technique requires refinement beyond 1.5 cps.

It is also of interest to note that the geologically homogeneous station, WO-AZ, shows a better agreement than the heterogeneous station, JR-AZ.

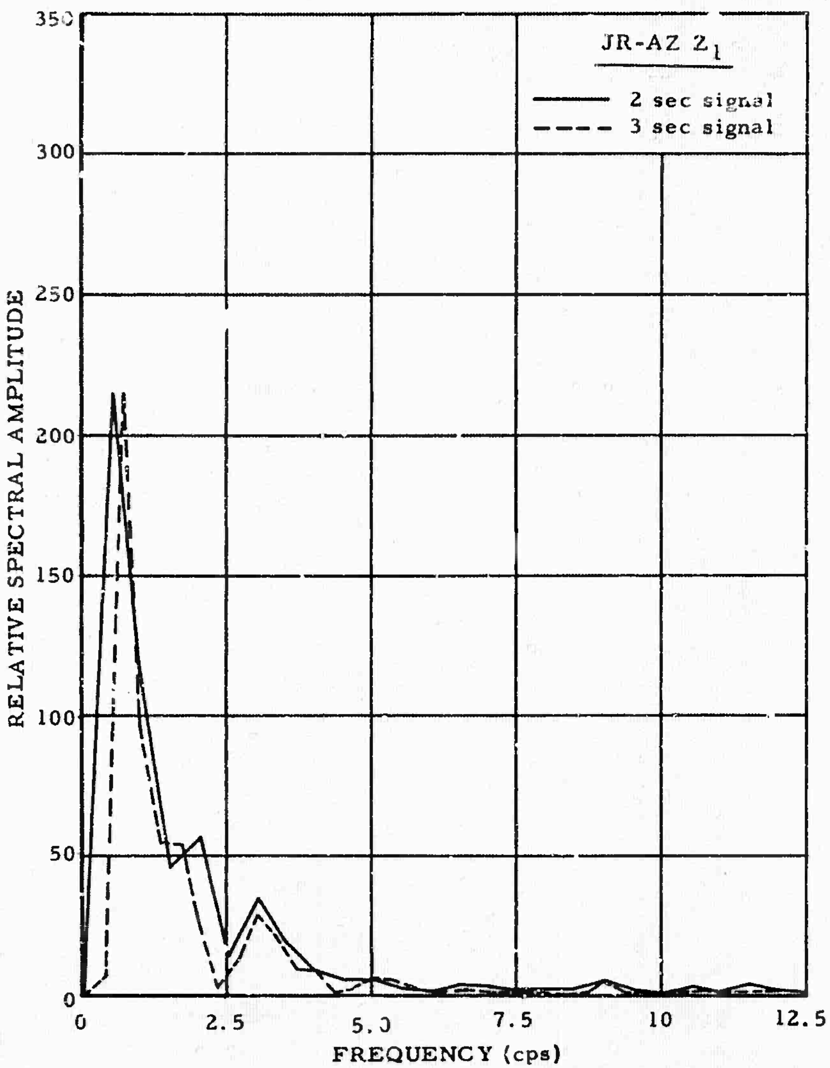

Figure 5. JR-AZ Z_1, amplitude spectrum of 2 June 1965 event

G 344

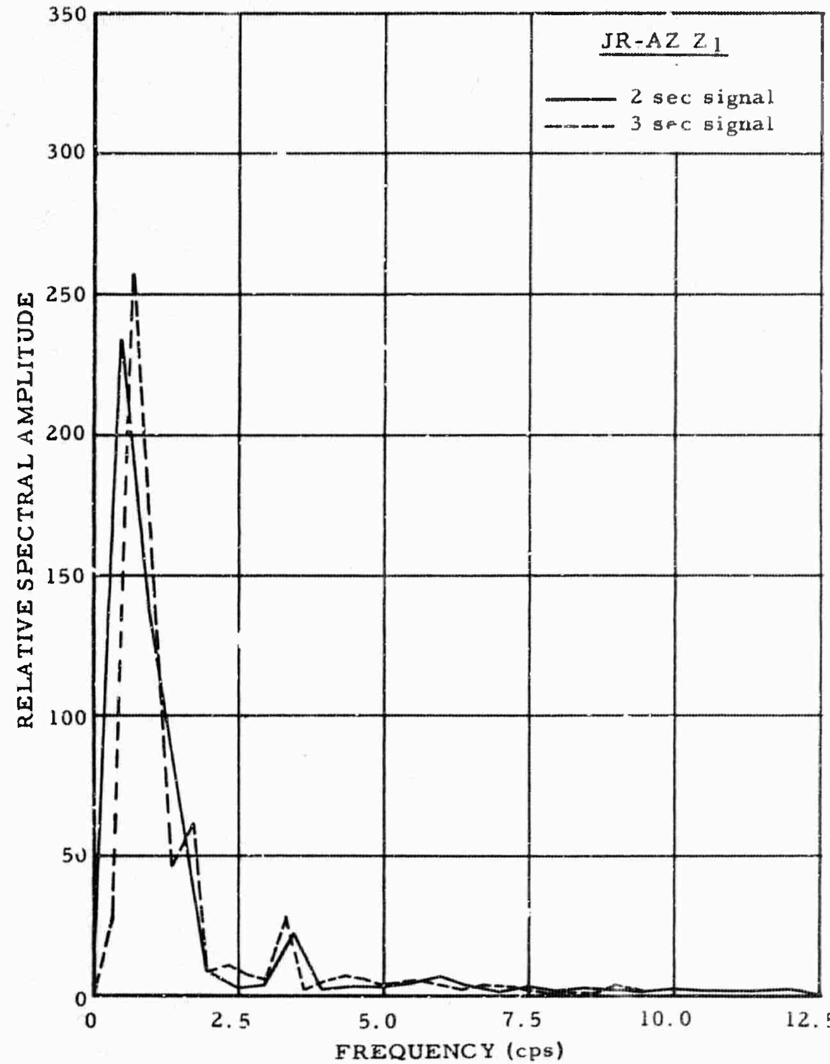

Figure 6. JR-AZ Z_2, amplitude spectrum of 2 June 1965 event

G 345

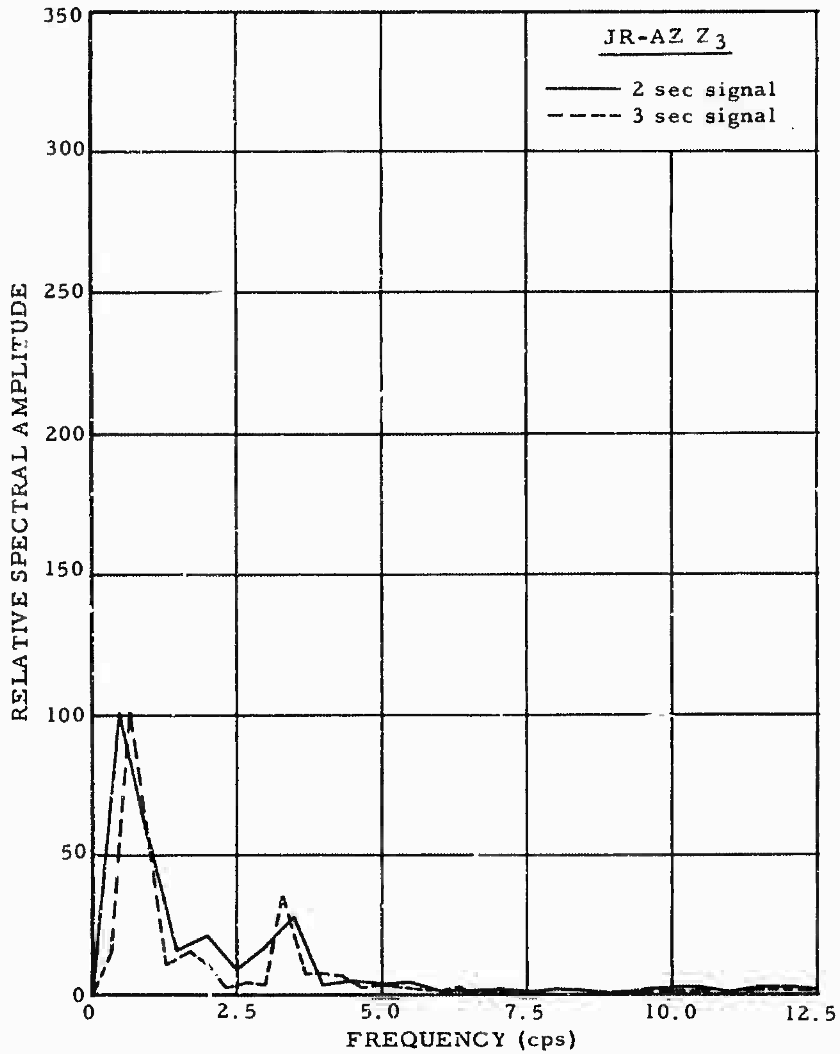

Figure 7. JR-AZ Z_3, amplitude spectrum of 2 June 1965 event

G 346

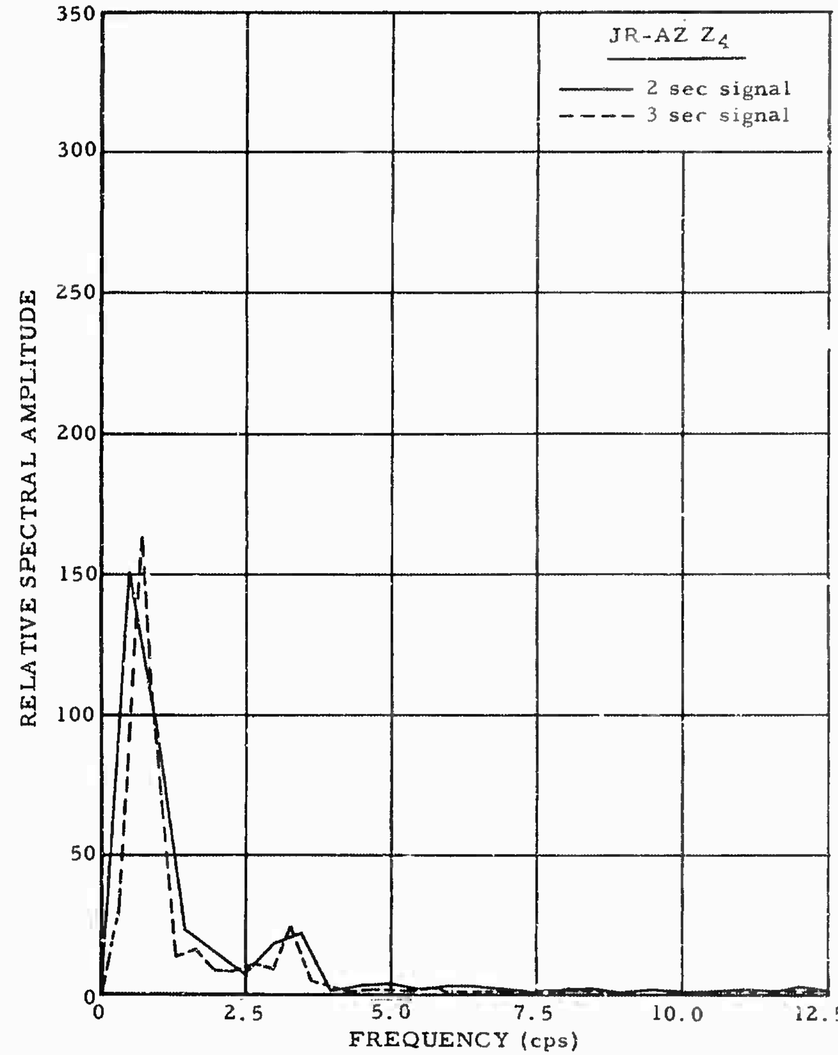

Figure 8. JR-AZ Z_4, amplitude spectrum of 2 June 1965 event

G 347

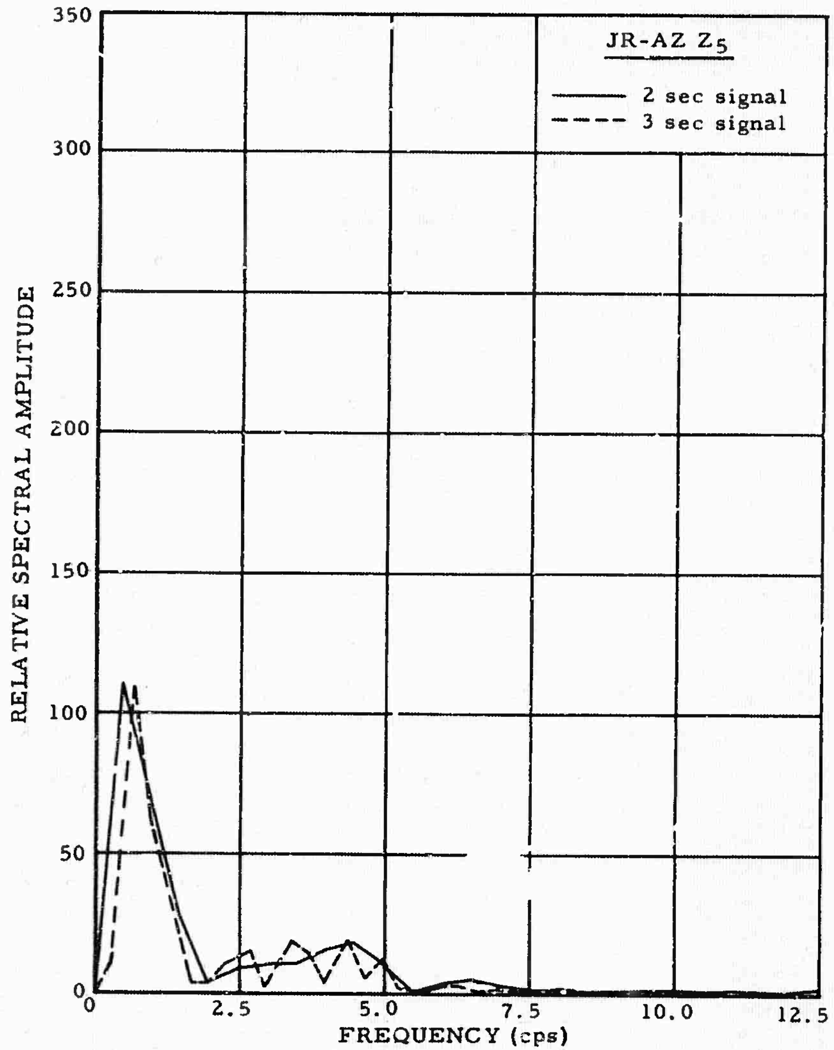

Figure 9. JR-AZ Z_5, amplitude spectrum of 2 June 1965 event

G 348

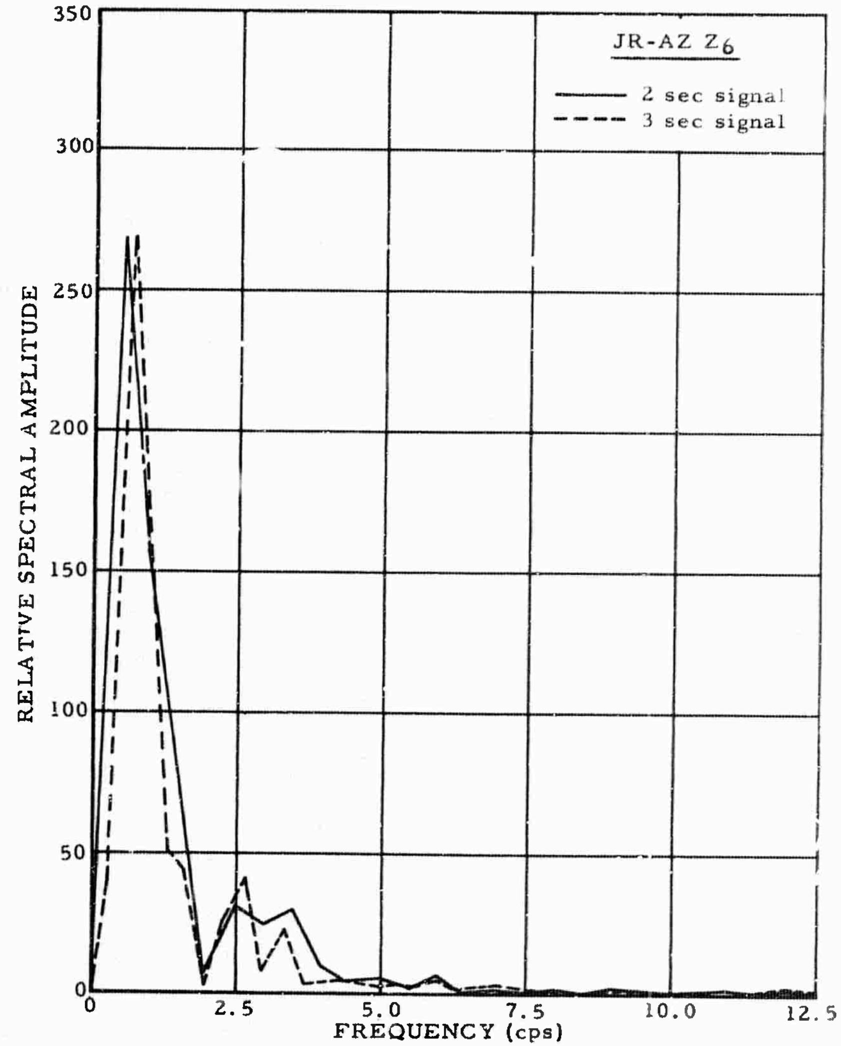

Figure 10. JR-AZ Z_6, amplitude spectrum of 2 June 1965 event

G 349

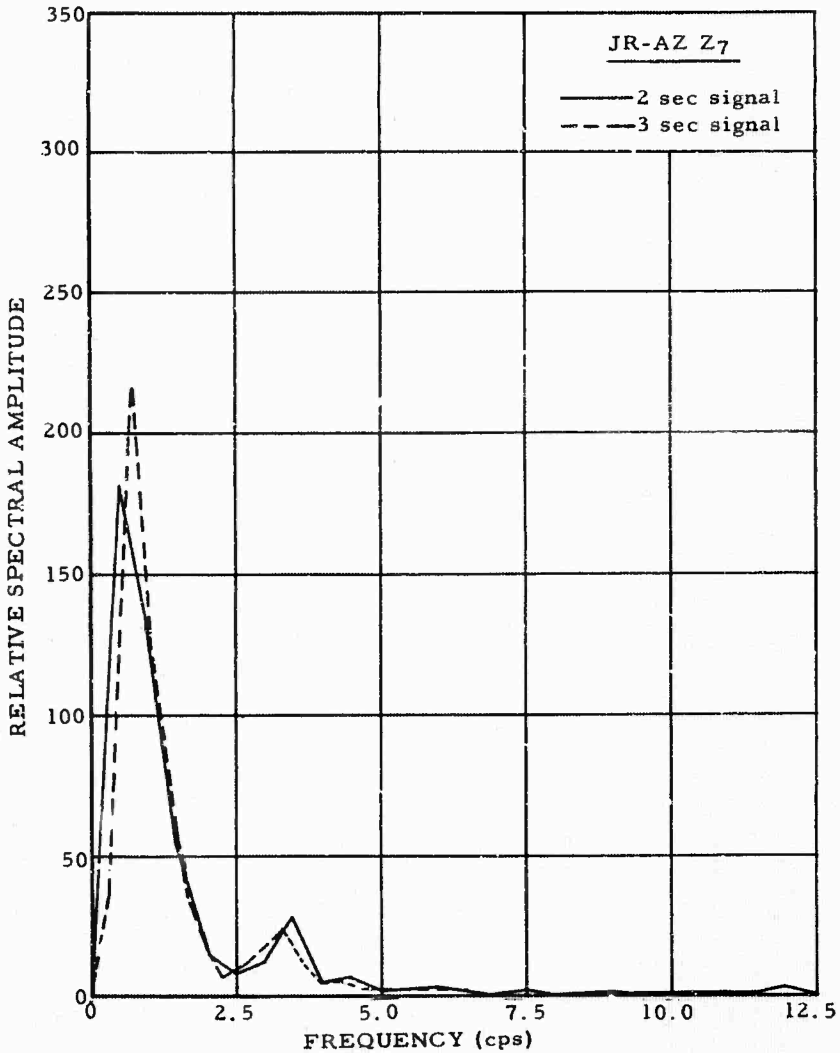

Figure 11. JR-AZ Z_7, amplitude spectrum of 2 June 1965 event

G 350

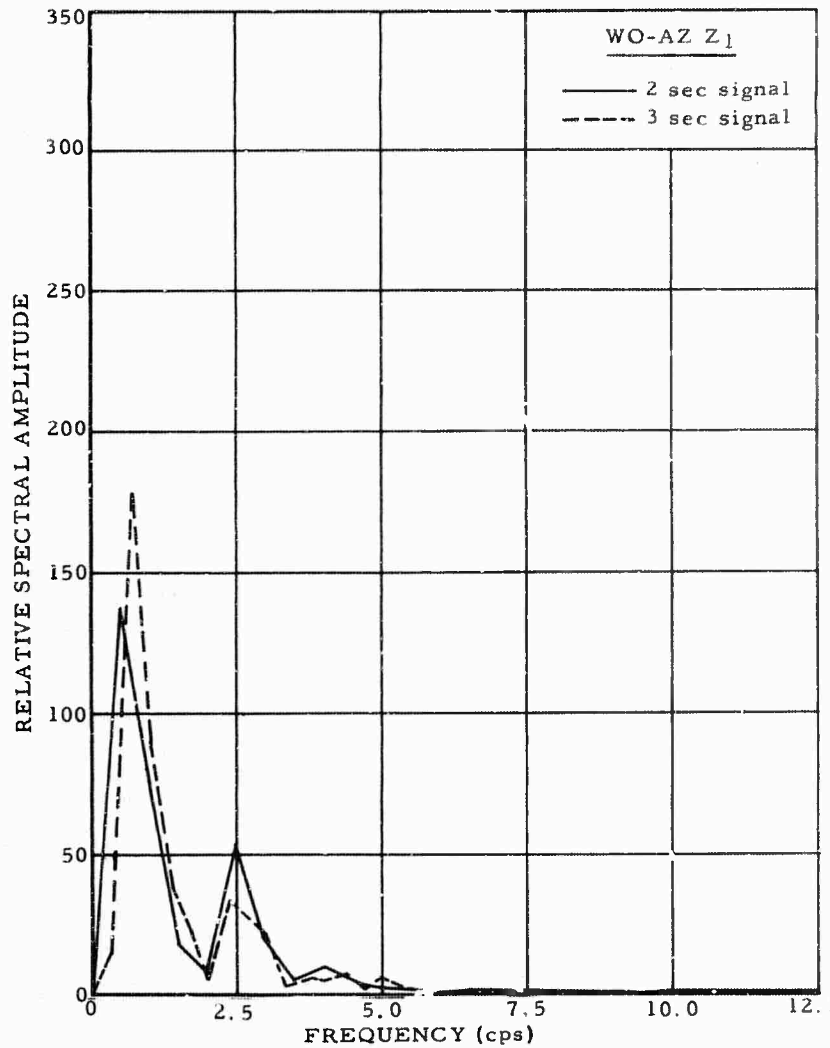

Figure 12. WO-AZ Z_1, amplitude spectrum of 2 June 1965 event

G 351

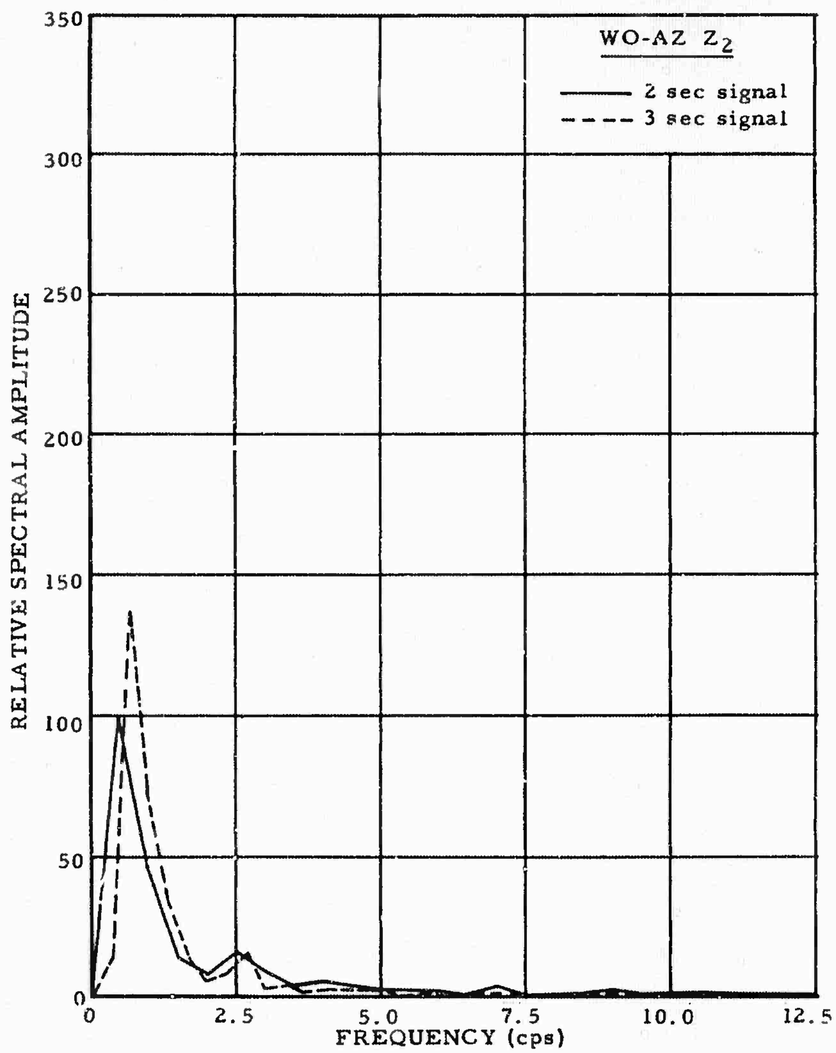

Figure 13. WO-AZ Z_2, amplitude spectrum of 2 June 1965 event

G 352

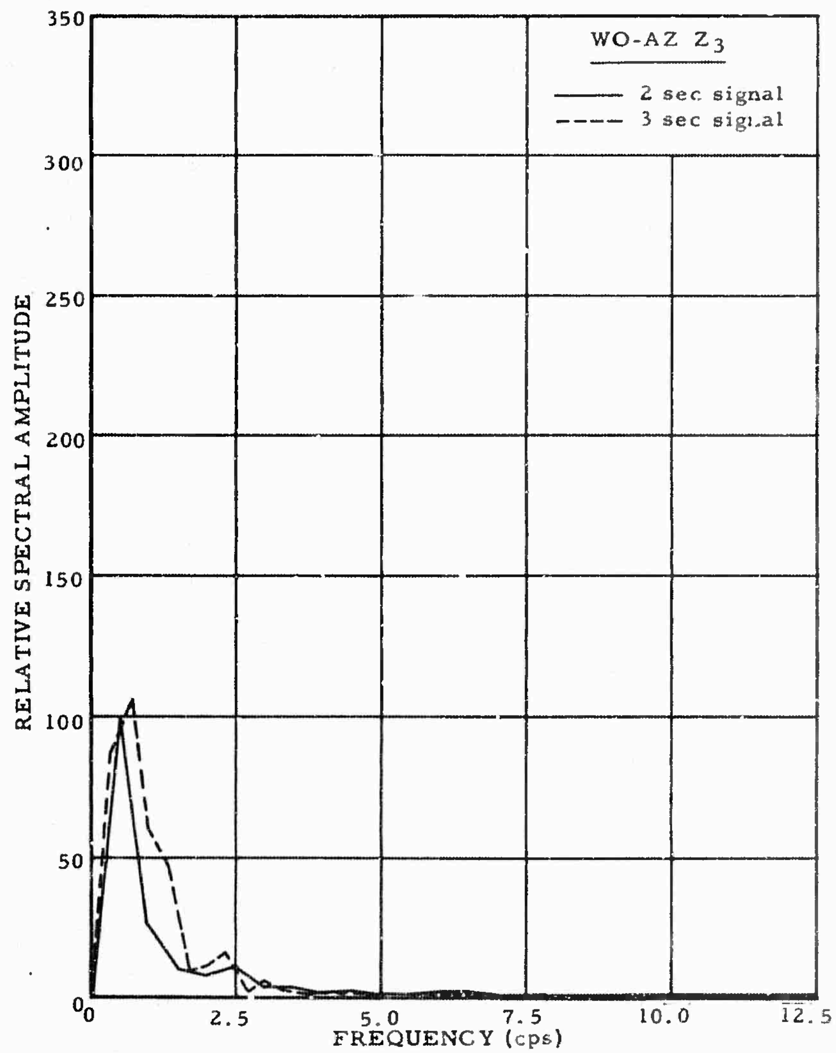

Figure 14. WO-AZ Z_3, amplitude spectrum of 2 June 1965 event

G 353

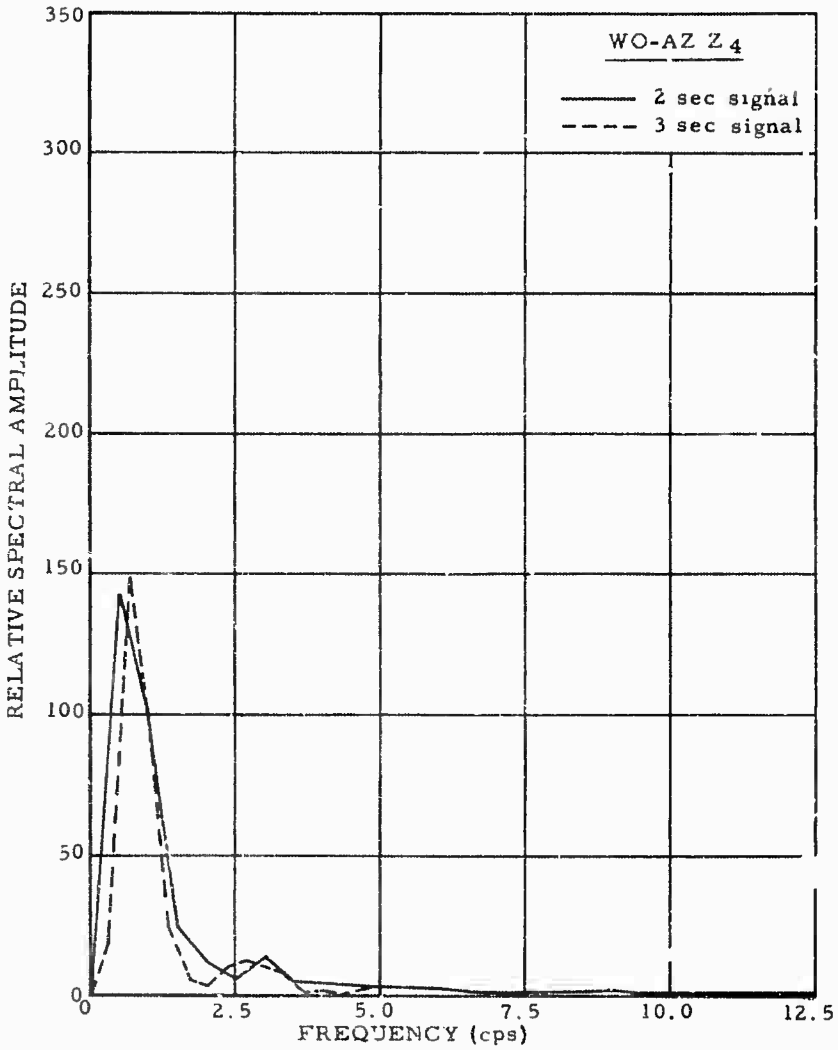

Figure 15. WO-AZ Z_4, amplitude spectrum of 2 June 1965 event

G 354

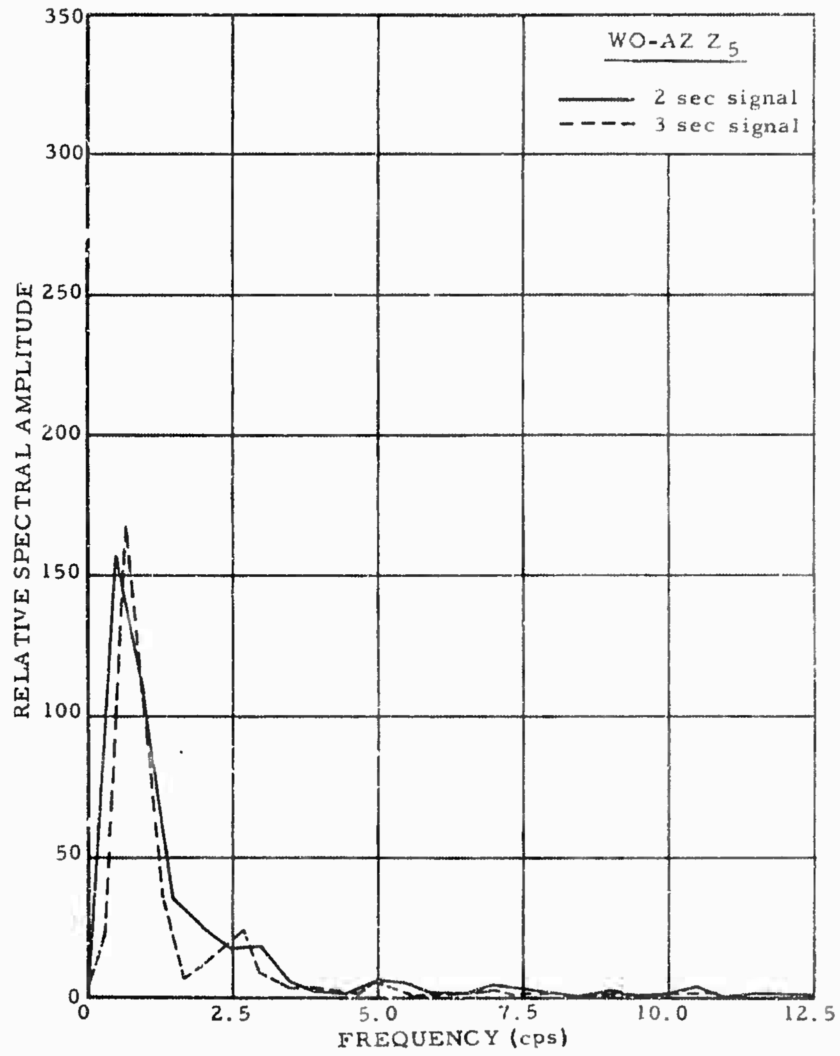

Figure 16. WO-AZ Z_5, amplitude spectrum of 2 June 1965 event

G 355

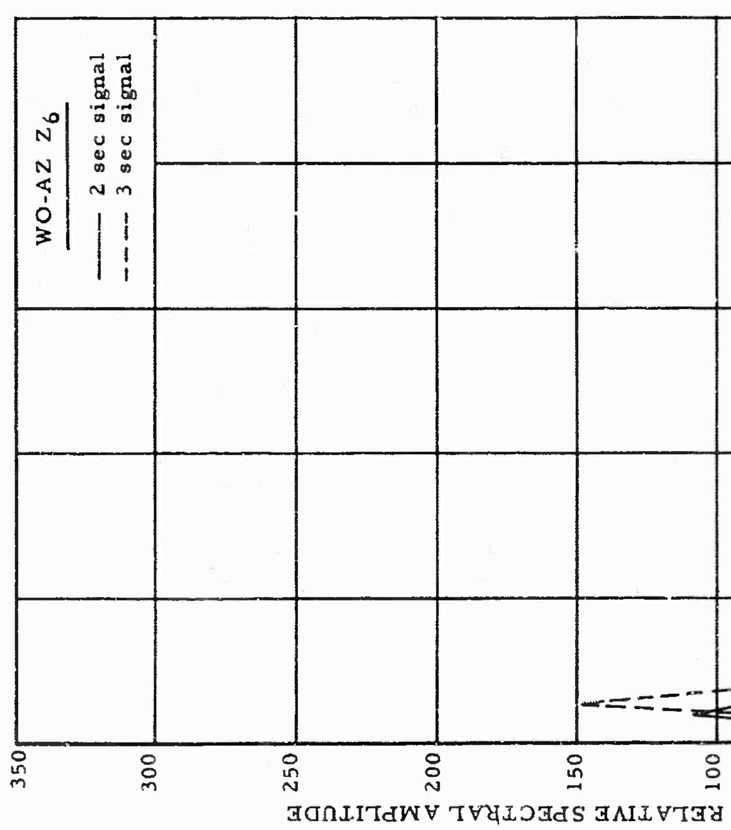

Figure 17. WO-AZ Z_6, amplitude spectrum of 2 June 1965 event

G 356

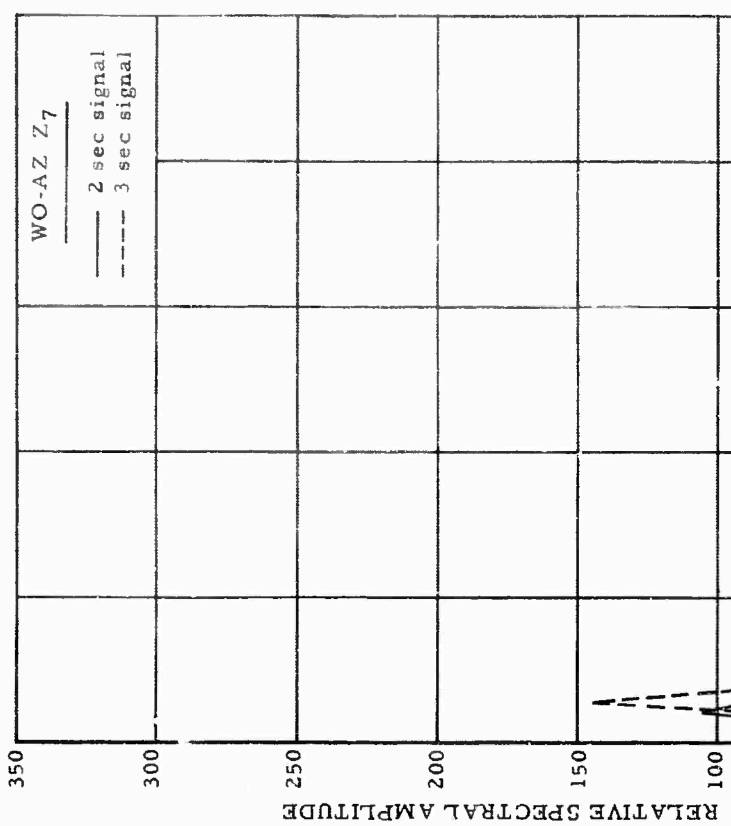

Figure 18. WO-AZ Z_7, amplitude spectrum of 2 June 1965 event

G 357

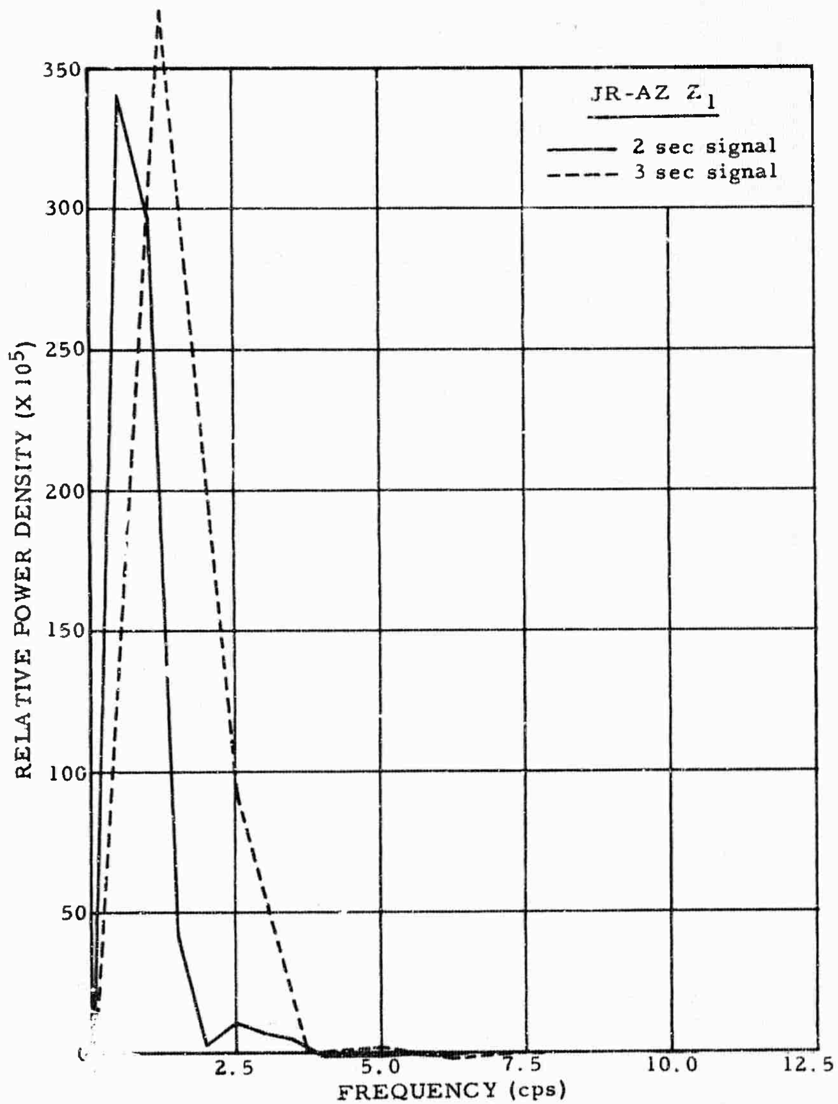

Figure 19. JR-AZ Z_1, power density spectrum of signal, 2 June 1965 event

G 358

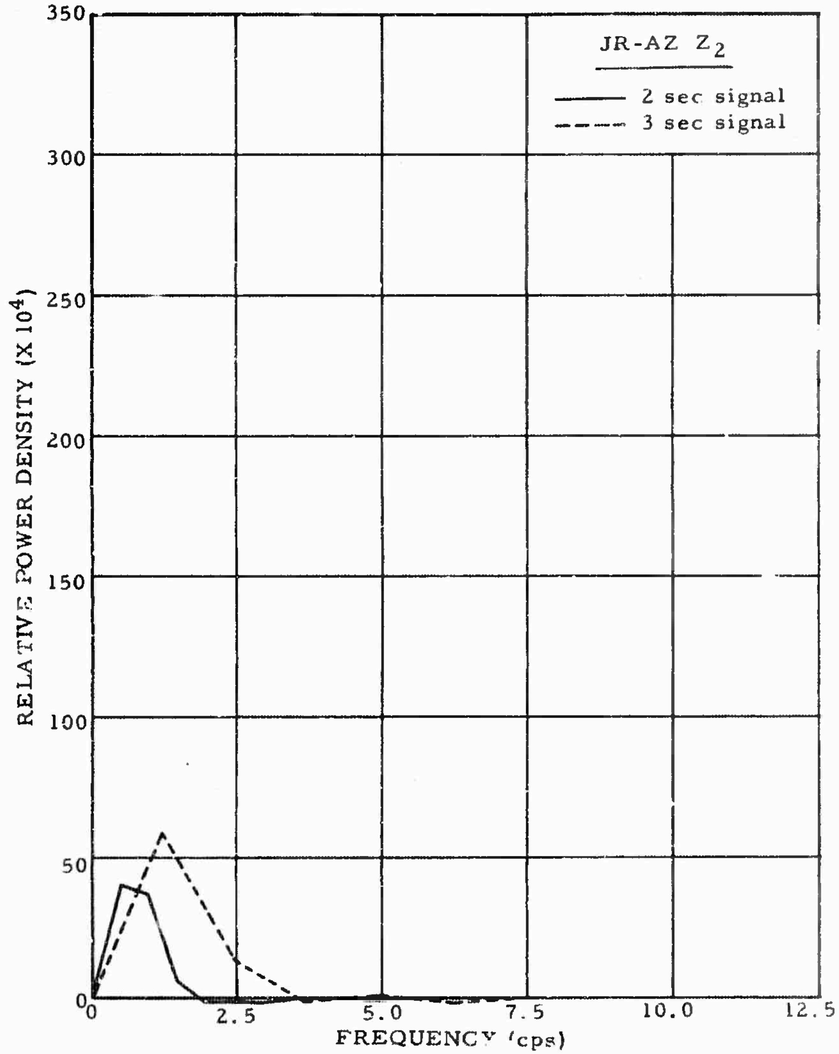

Figure 20. JR-AZ Z_2, power density spectrum of signal, 2 June 1965 event

G 359

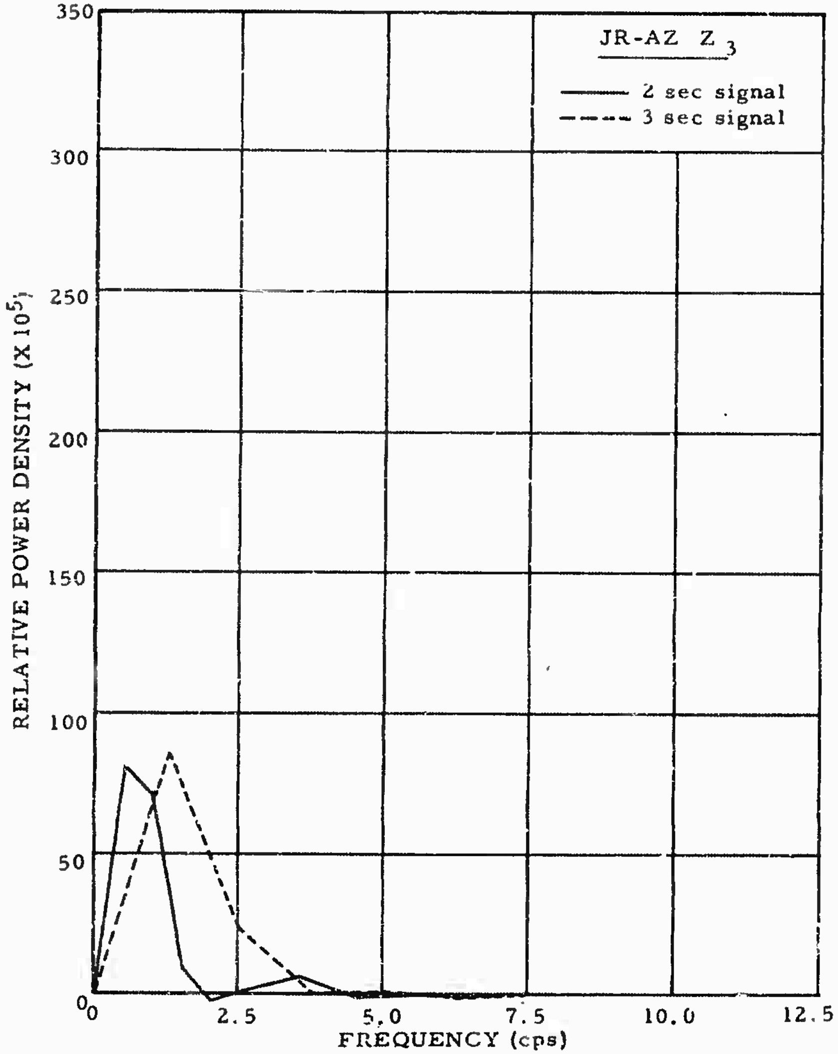

Figure 21. JR-AZ Z_3, power density spectrum of signal, 2 June 1965 event

G 360

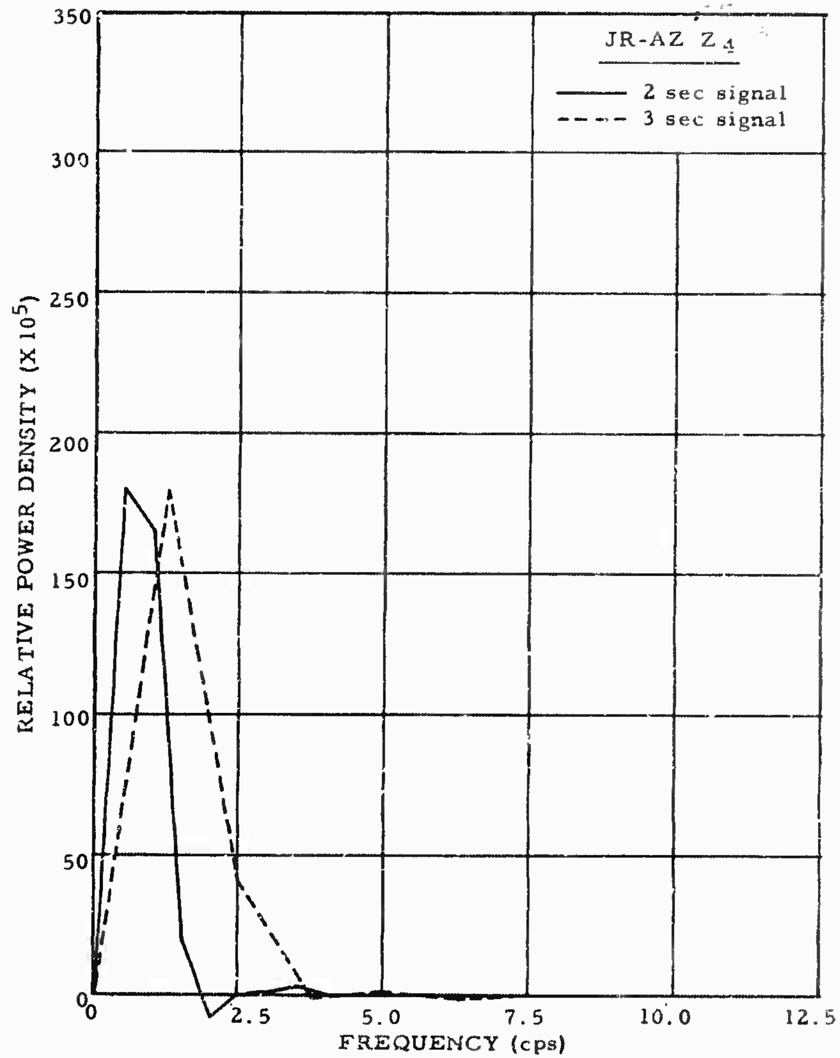

Figure 22. JR-AZ Z_4, power density spectrum of signal, 2 June 1965 event

G 361

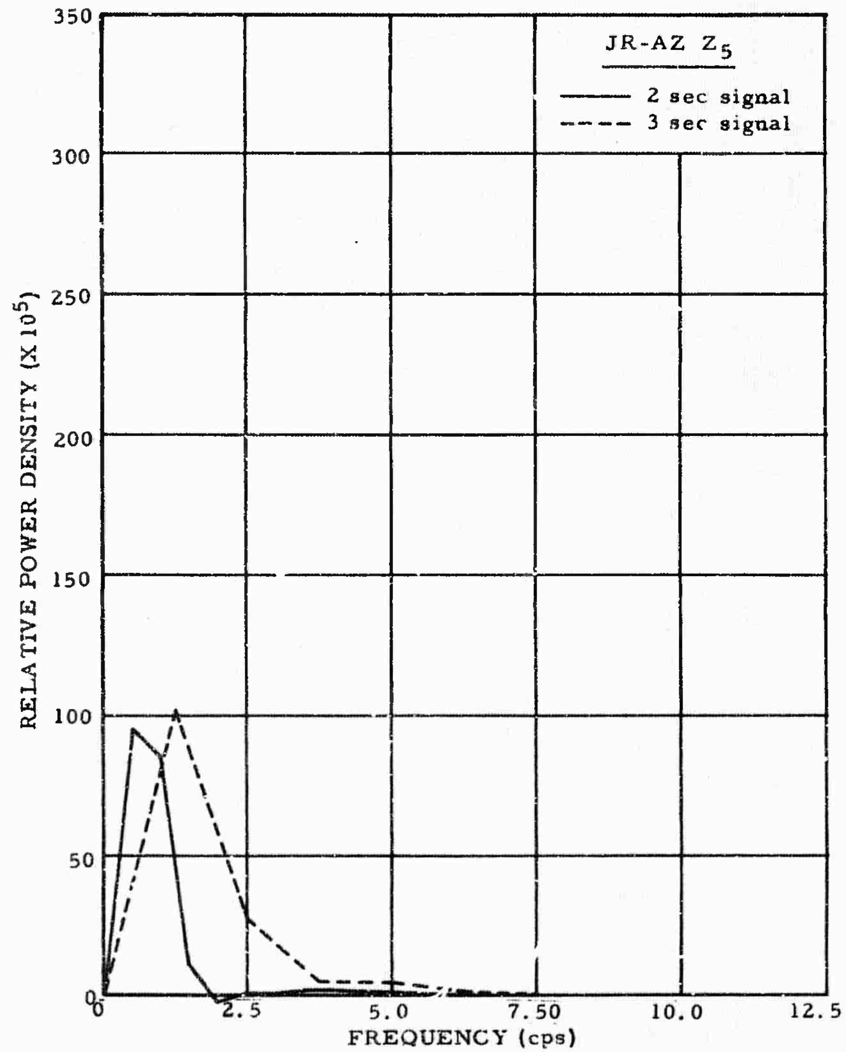

Figure 23. JR-AZ Z_5, power density spectrum of signal, 2 June 1965 event

G 362

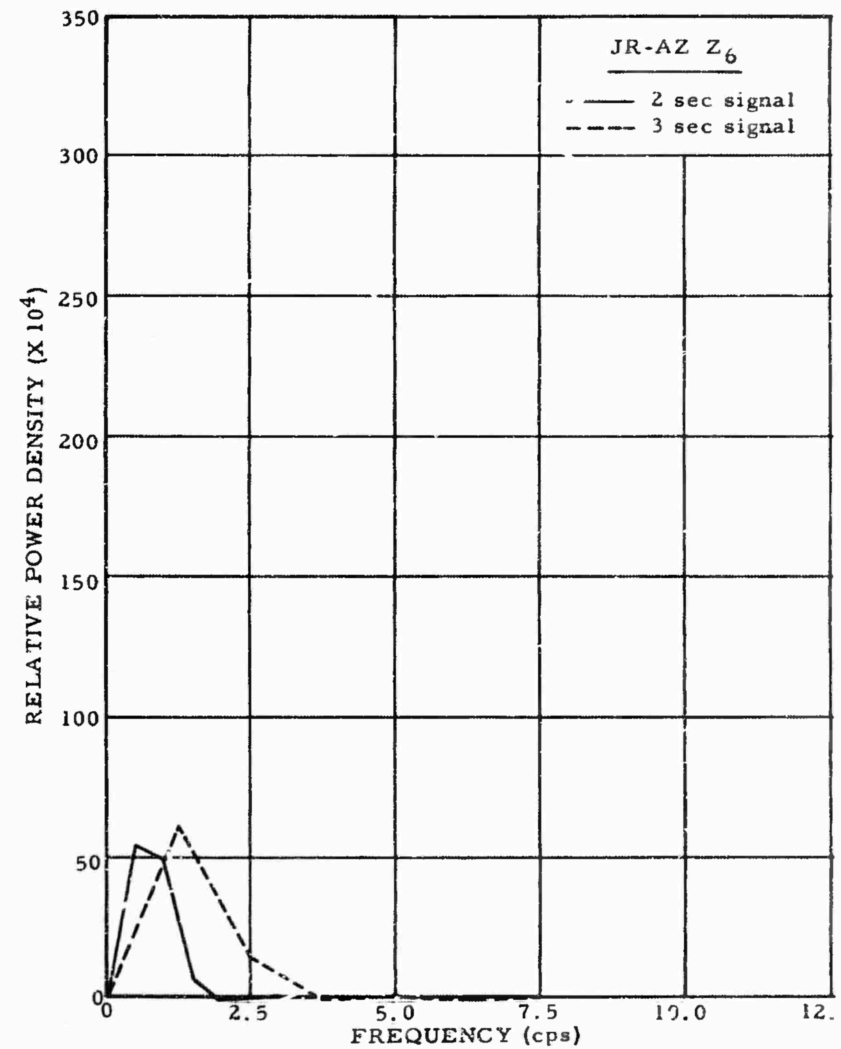

Figure 24. JR-AZ Z_6, power density spectrum of signal, 2 June 1965 event

G 363

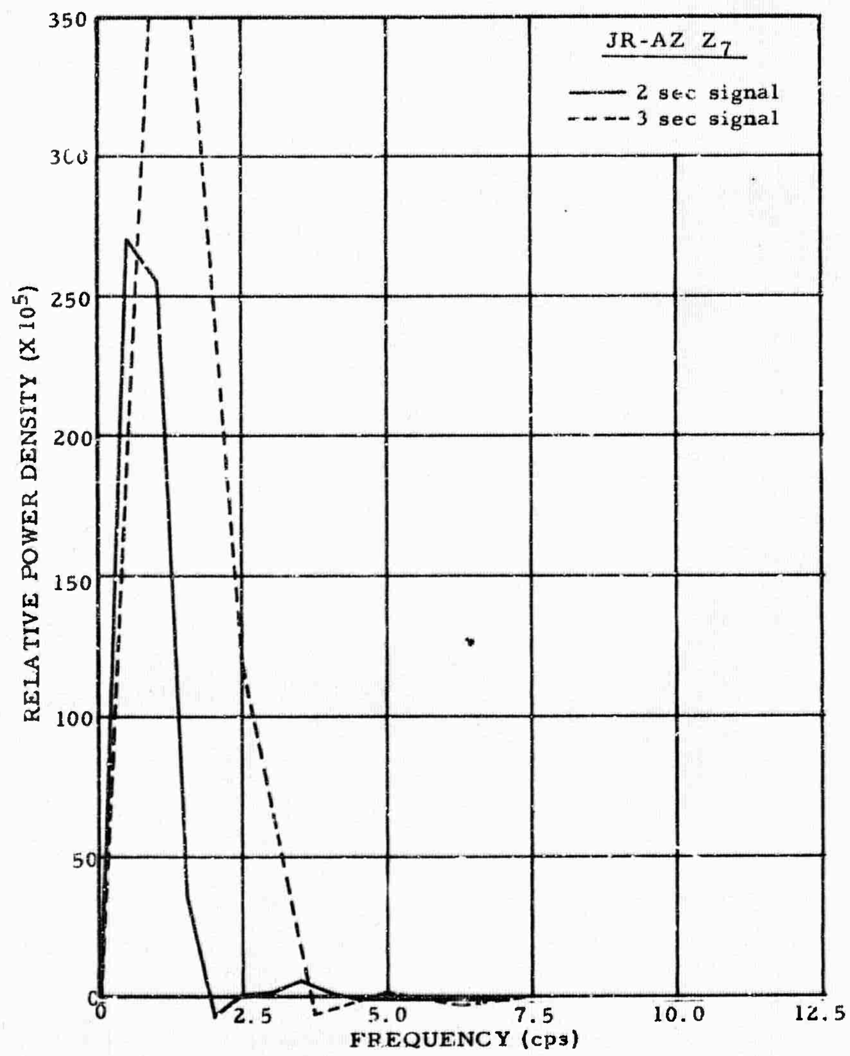

Figure 25. JR-AZ Z_7, power density spectrum of signal, 2 June 1965 event

G 364

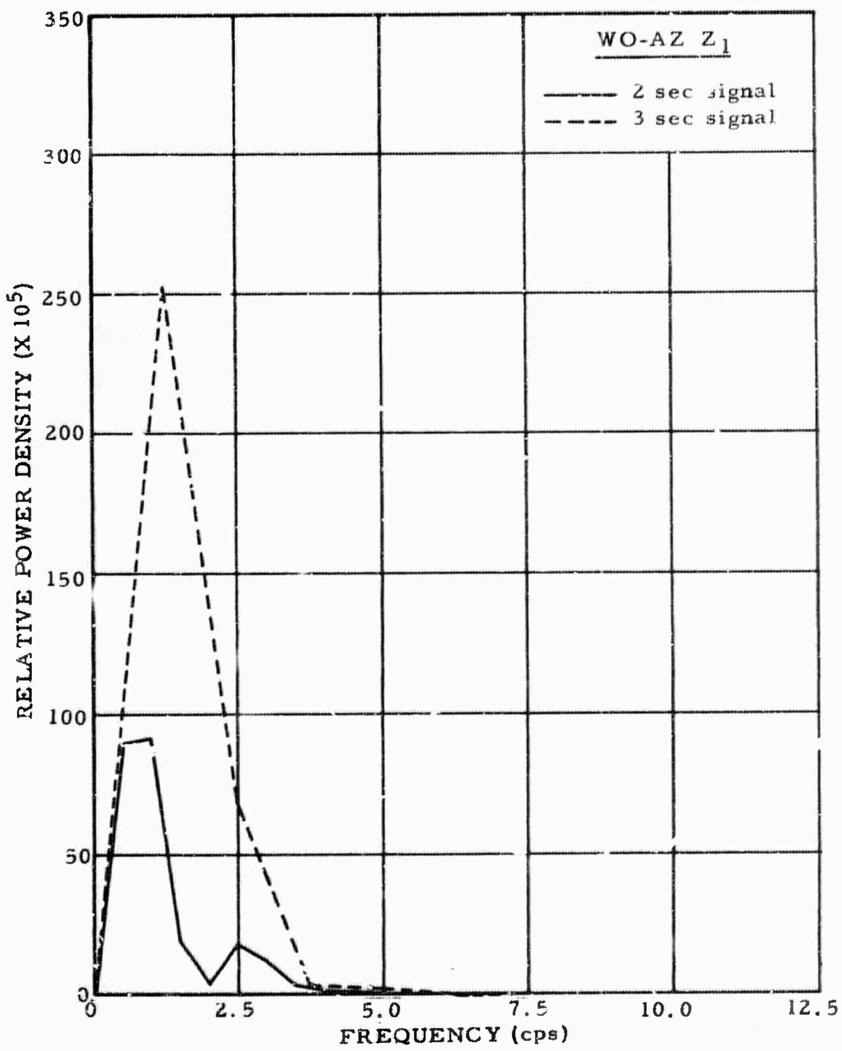

Figure 26. WO-AZ Z_1, power density spectrum of signal, 2 June 1965 event

G 365

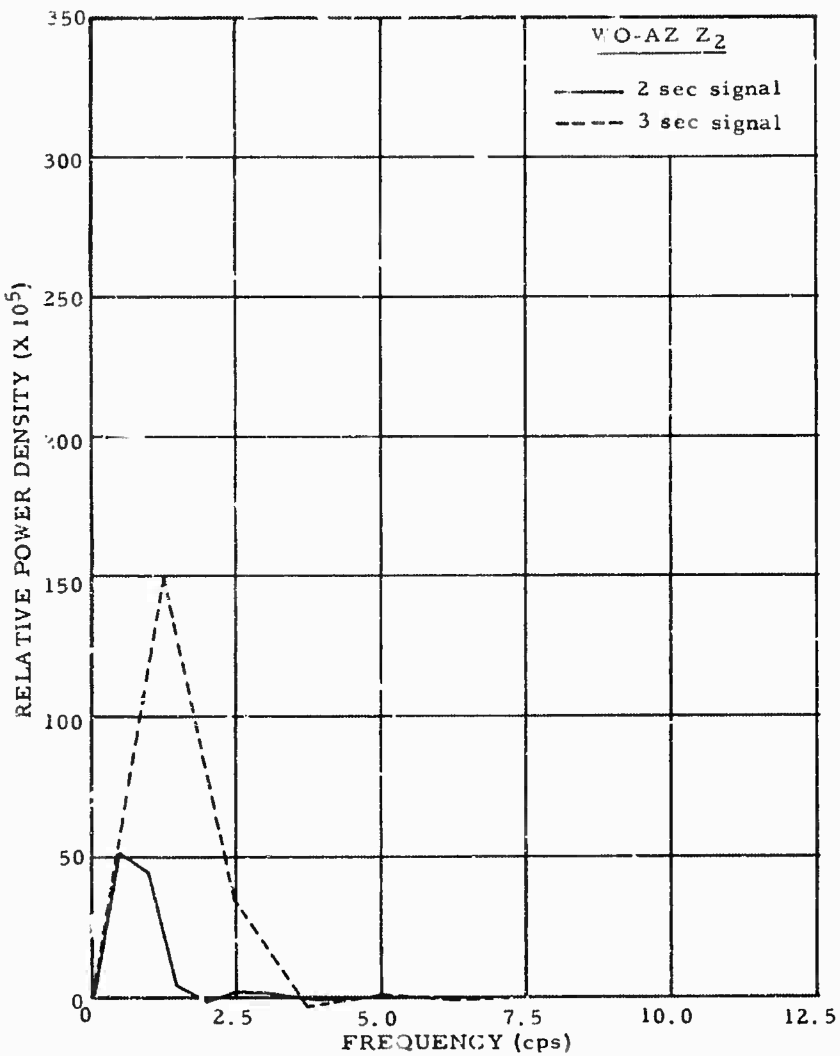

Figure 27. WO-AZ Z_2, power density spectrum of signal, 2 June 1965 event

G 366

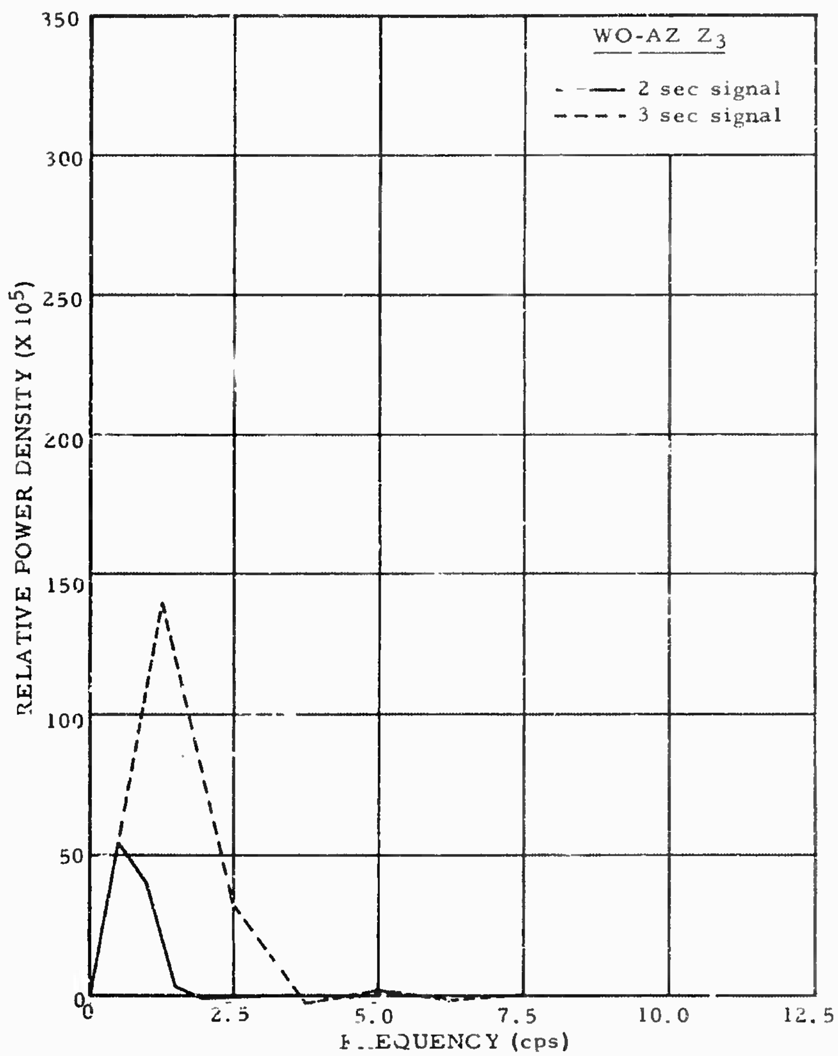

Figure 28. WO-AZ Z_3, power density spectrum of signal, 2 June 1965 event

G 367

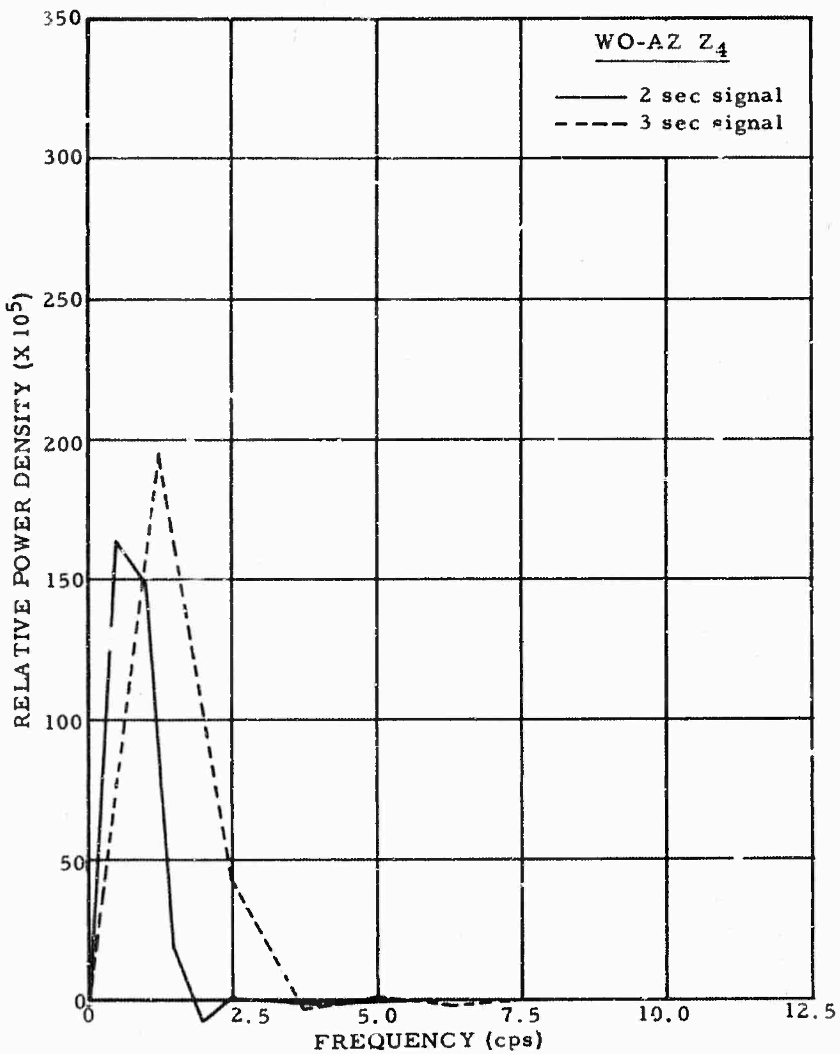

Figure 29. WO-AZ Z_4, power density spectrum of signal, 2 June 1965 event

G 368

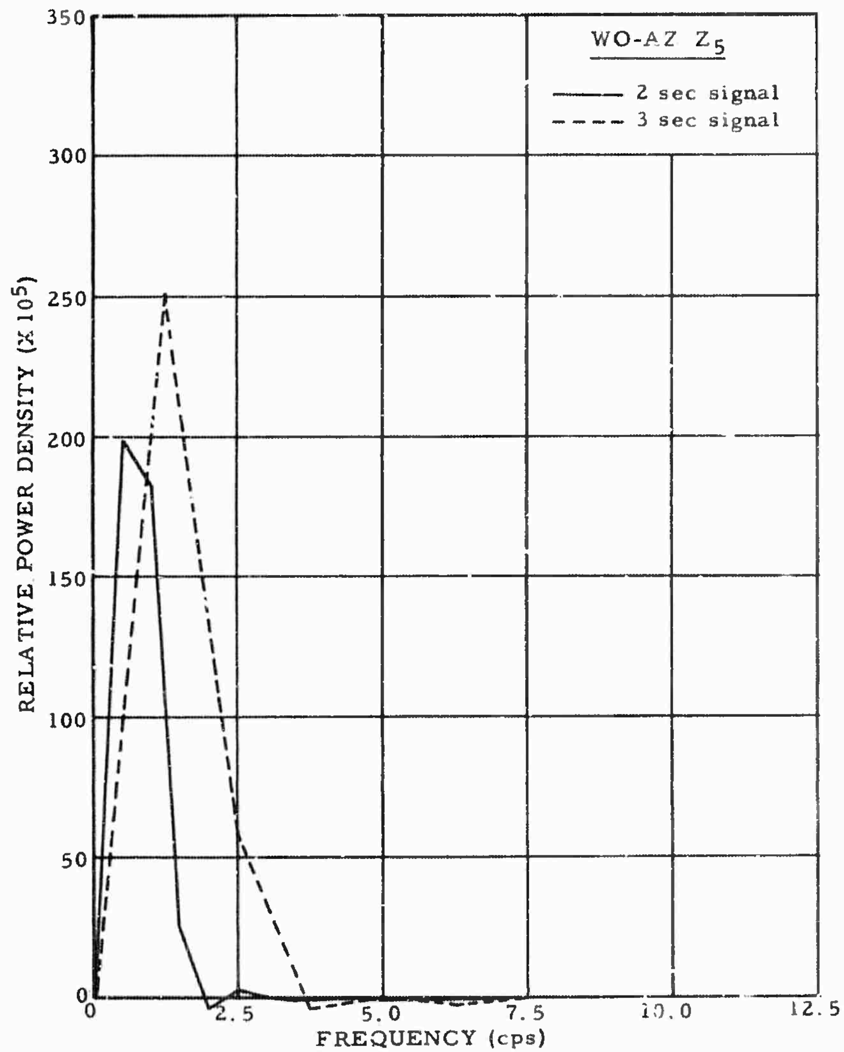

Figure 30. WO-AZ Z_5, power density spectrum of signal, 2 June 1965 event

G 369

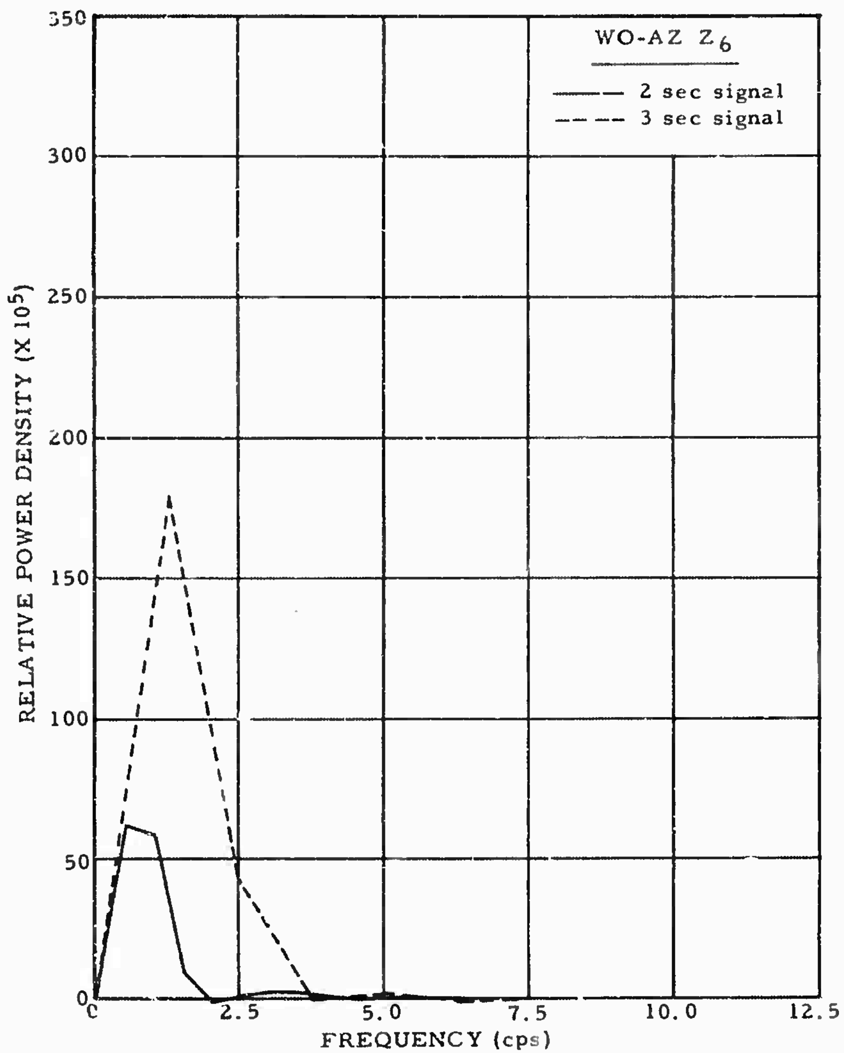

Figure 31. WO-AZ Z_6, power density spectrum of signal, 2 June 1965 event

G 370

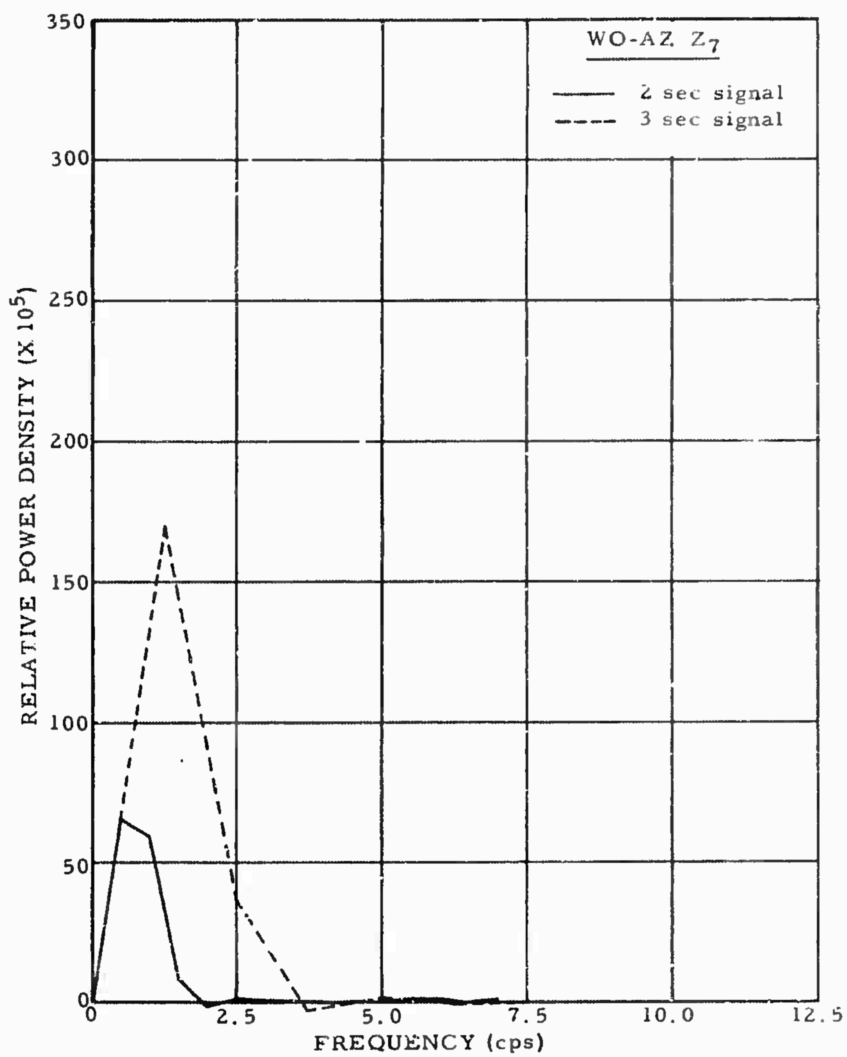

Figure 32. WO-AZ Z_7, power density spectrum of signal, 2 June 1965 event

G 371

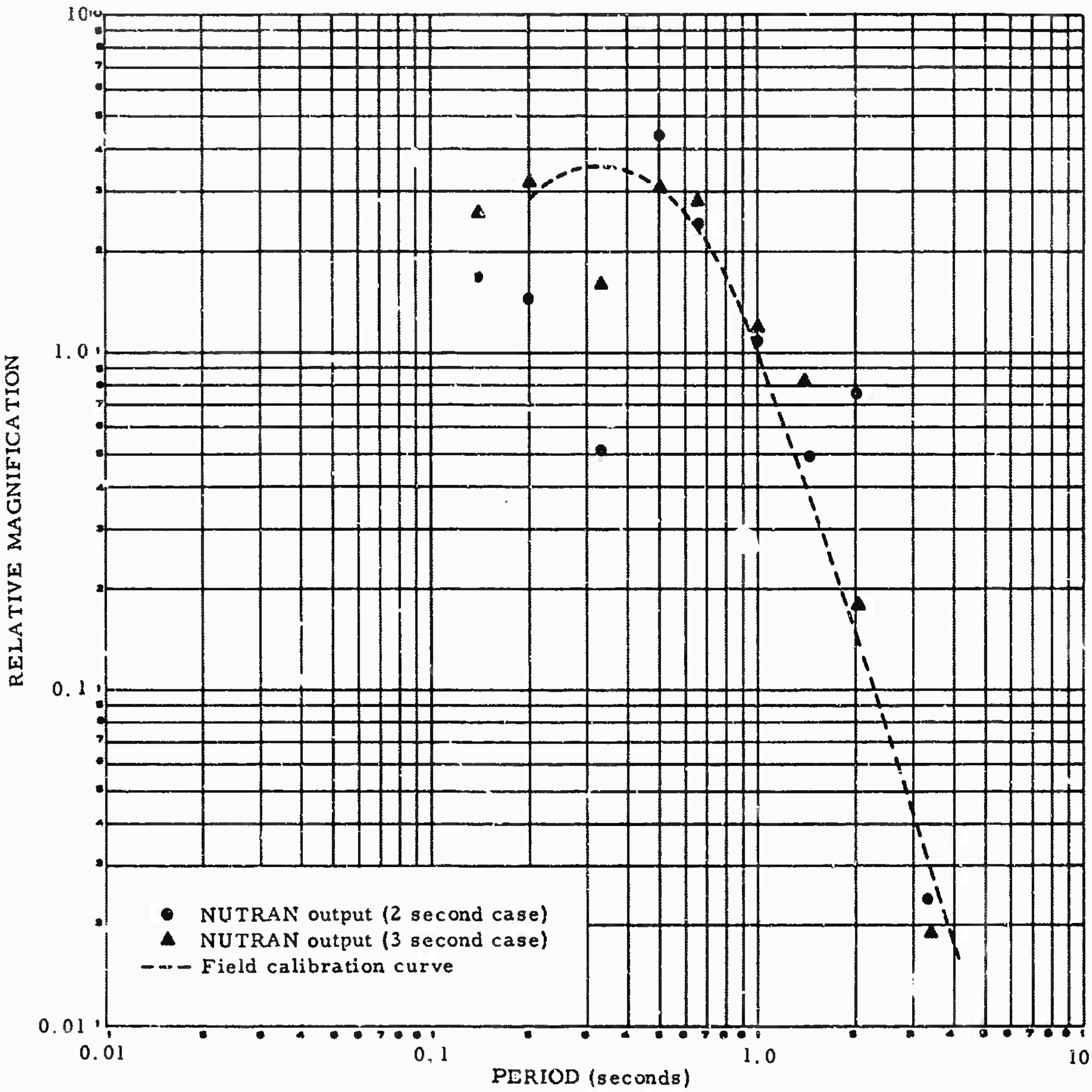

Figure 33. Unsmoothed calibration estimates at JR-AZ Z_2, 2 and 3 second cases

G 372

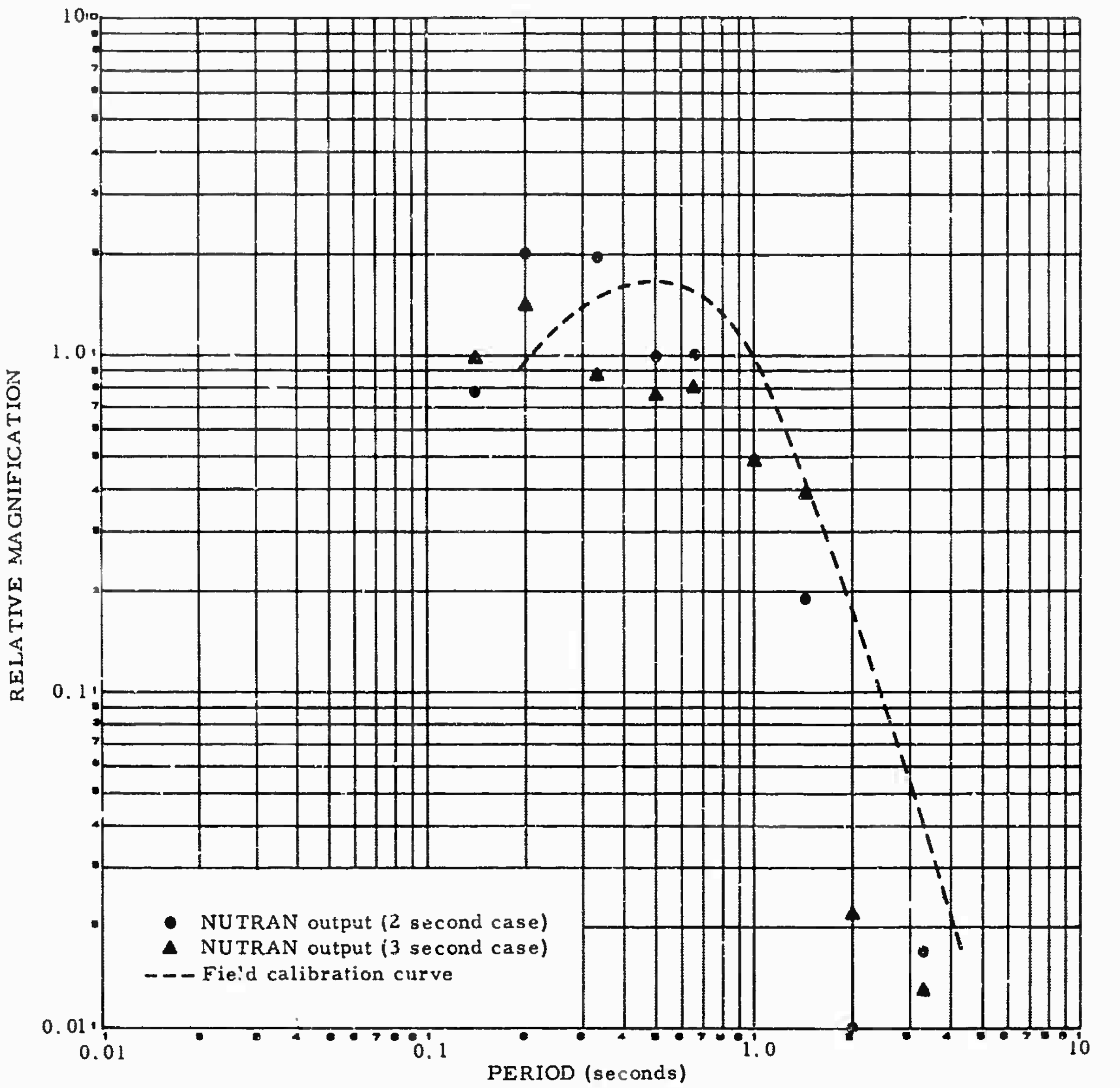

Figure 34. Unsmoothed calibration estimates at JR-AZ Z_3, 2 and 3 second cases

G 373

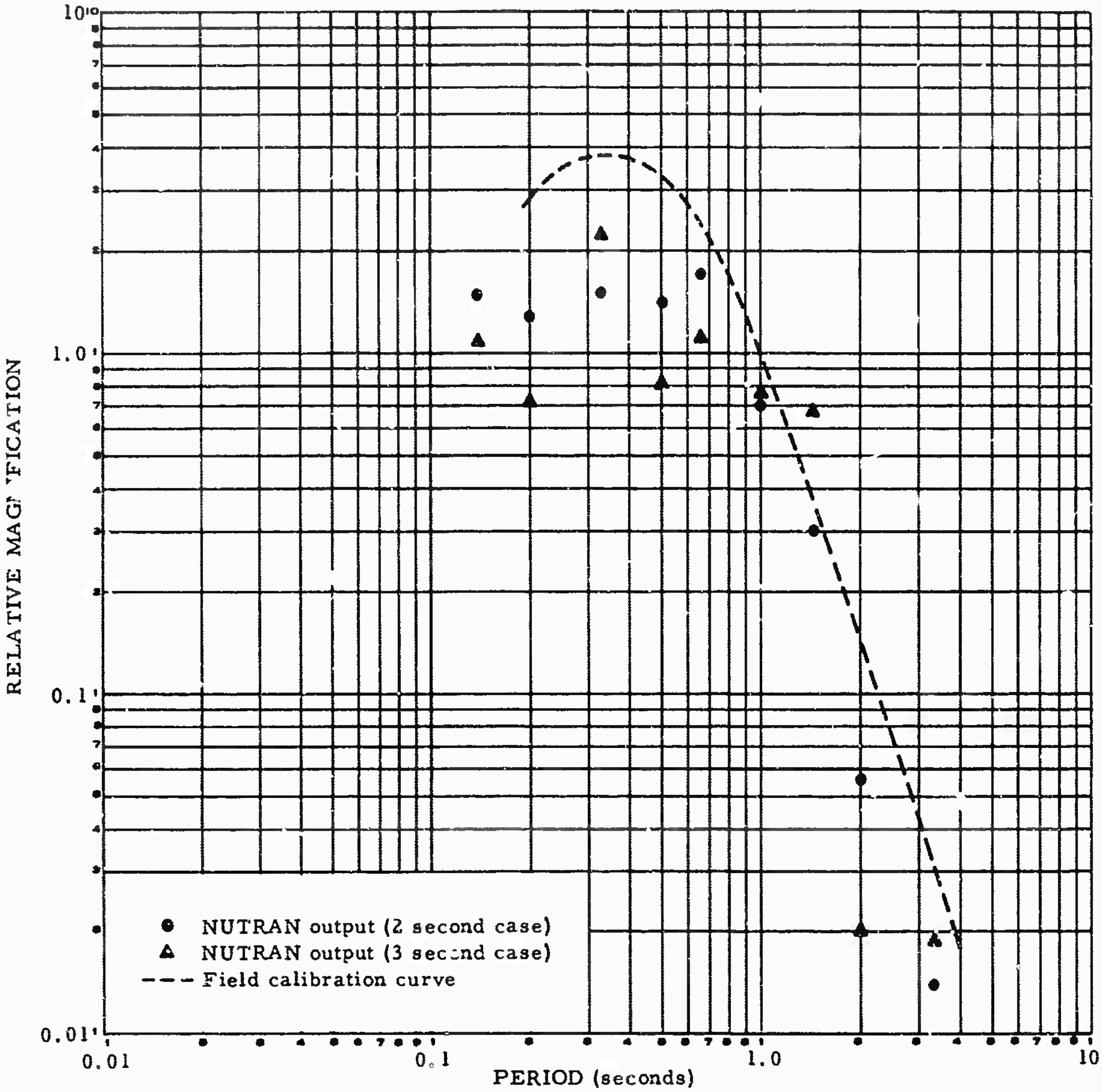

Figure 35. Unsmoothed calibration estimates at JR-AZ Z_4, 2 and 3 second cases

G 374

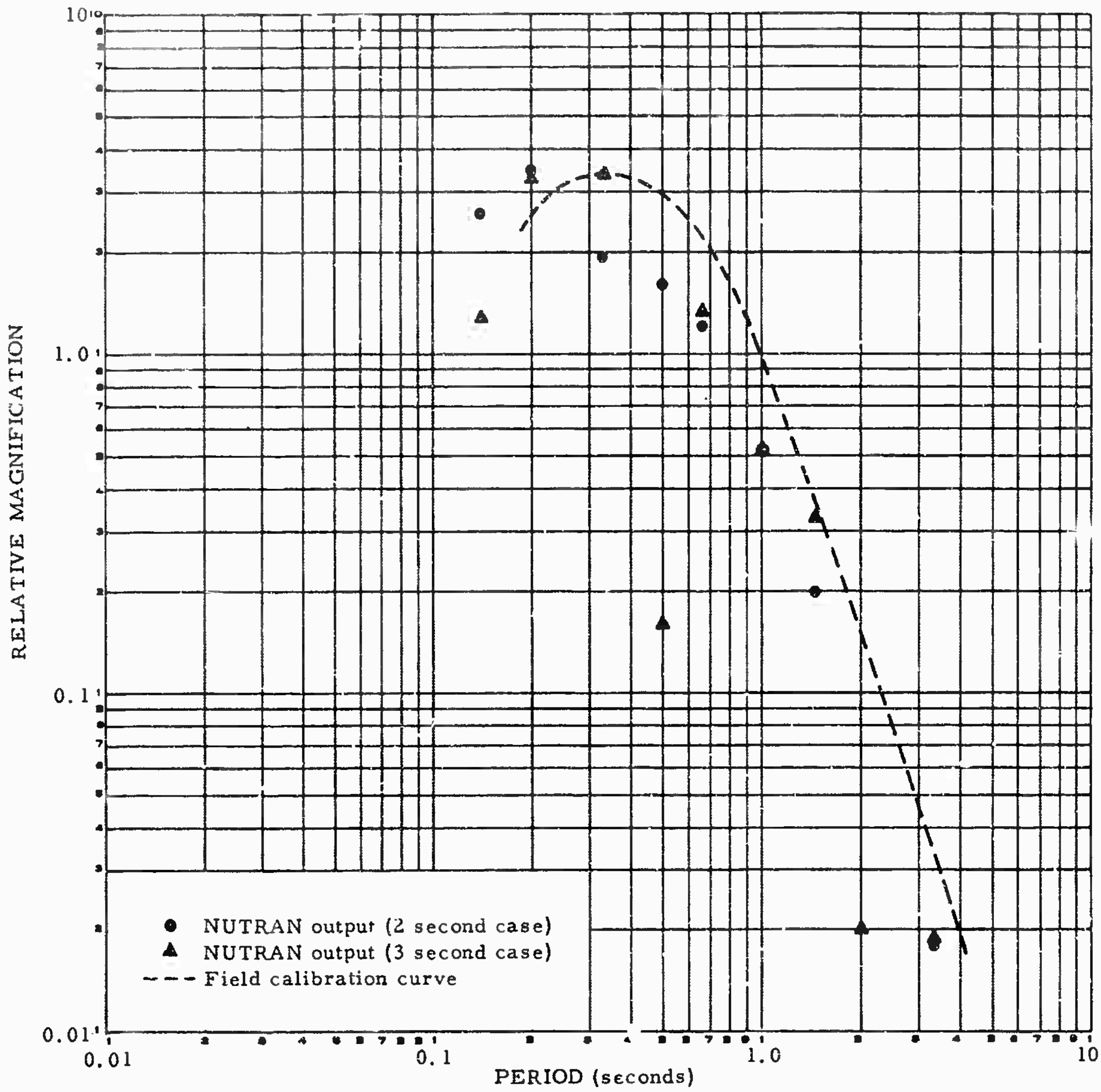

Figure 36. Unsmoothed calibration estimates at JR-AZ Z_5, 2 and 3 second cases

G 375

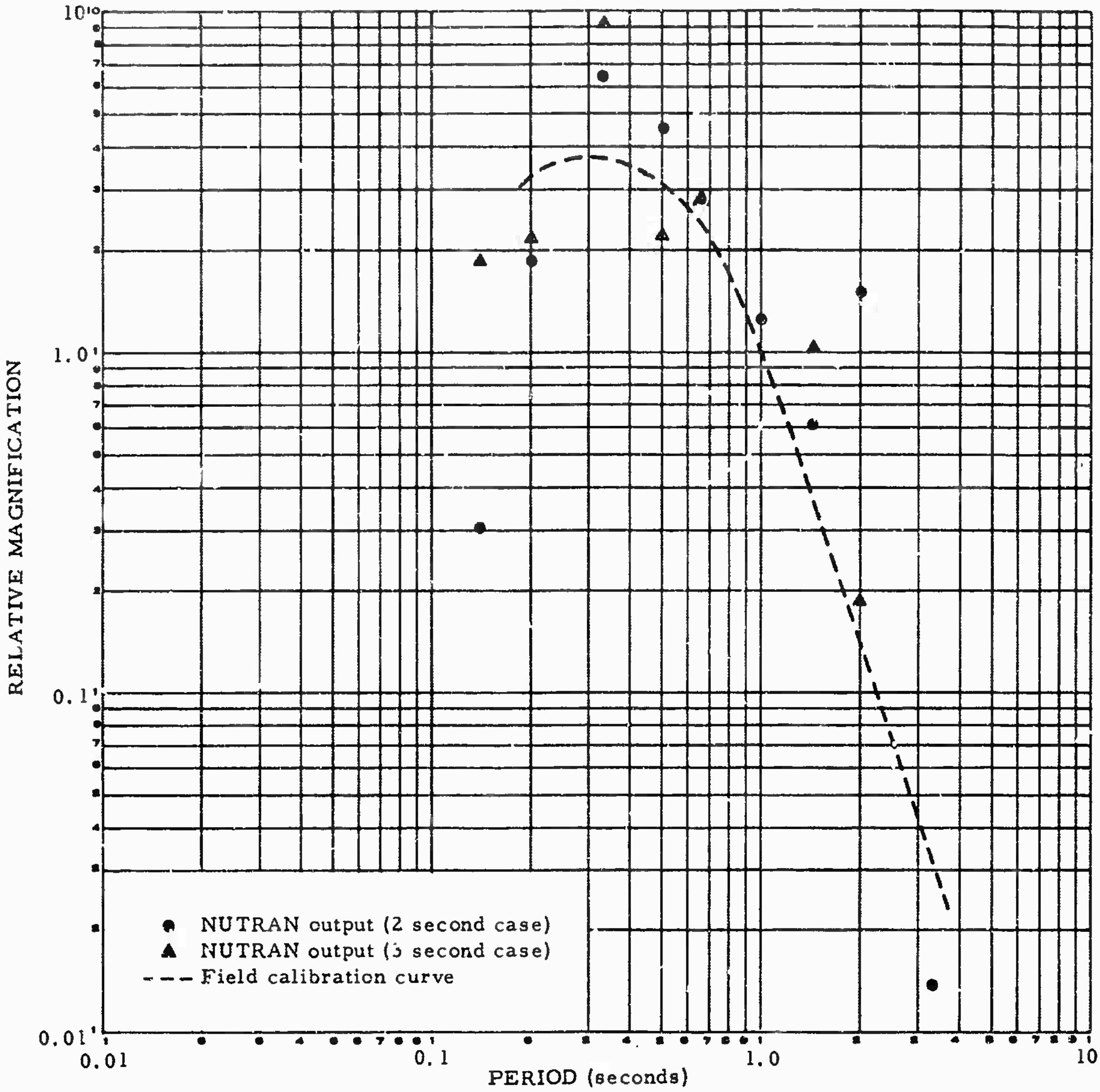

Figure 37. Unsmoothed calibration estimates at JR-AZ Z_6, 2 and 3 second cases

G 376

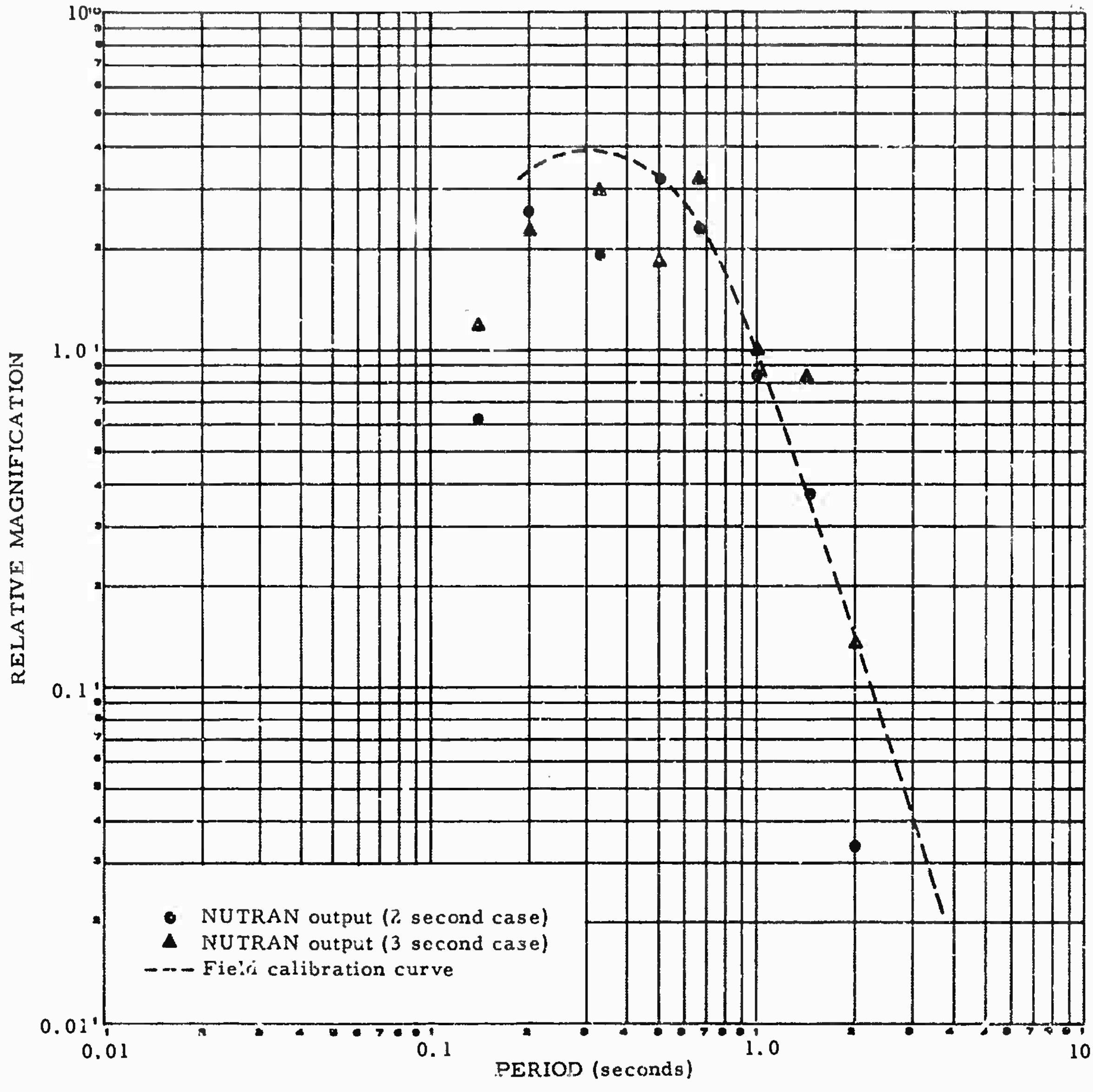

Figure 38. Unsmoothed calibration estimates at JR-AZ Z_7, 2 and 3 second cases

G 377

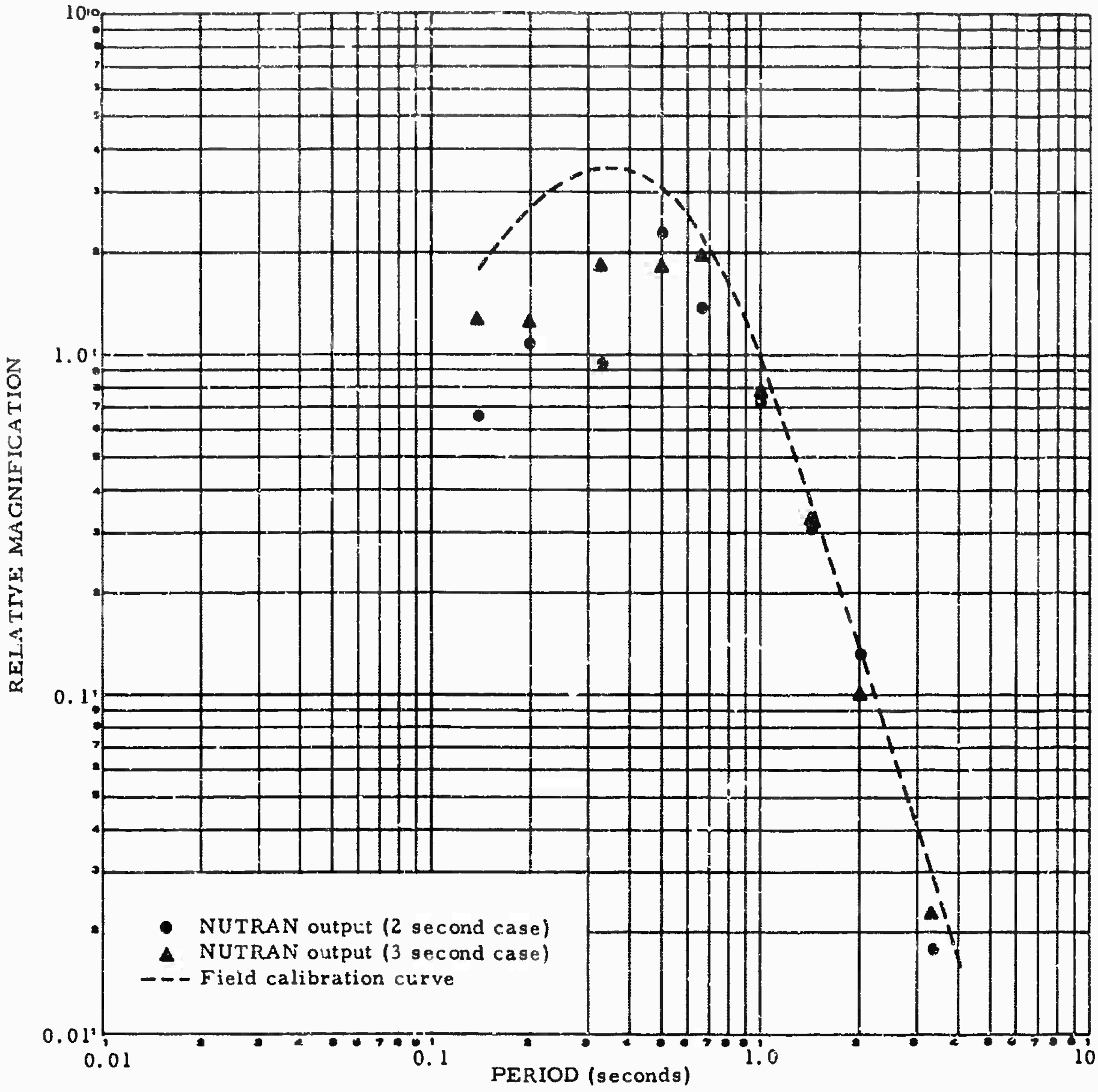

Figure 39. Unsmoothed calibration estimates at WO-AZ Z_2, 2 and 3 second cases

G 378

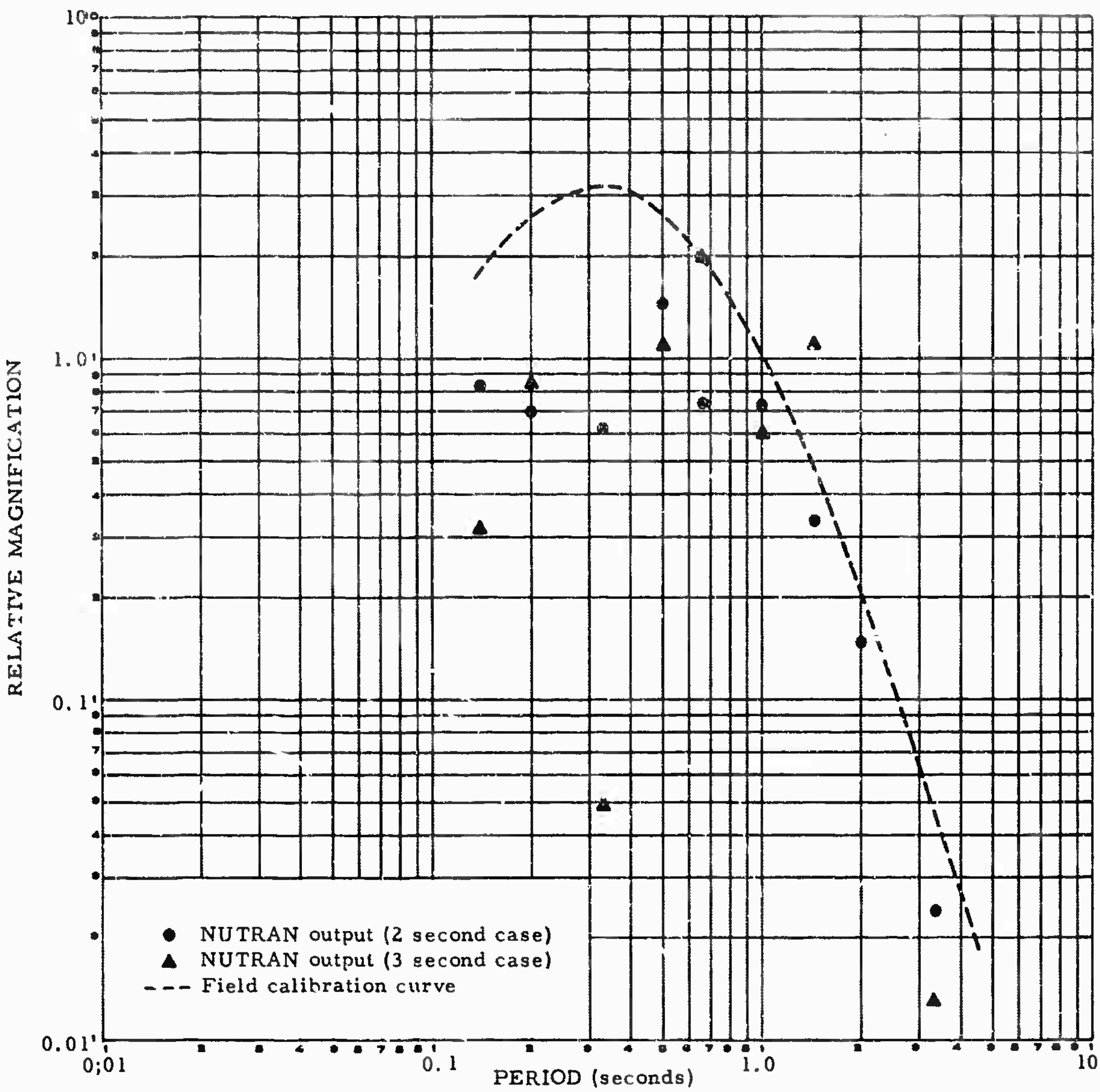

Figure 40. Unsmoothed calibration estimates at WO-AZ Z_3, 2 and 3 second cases

G 379

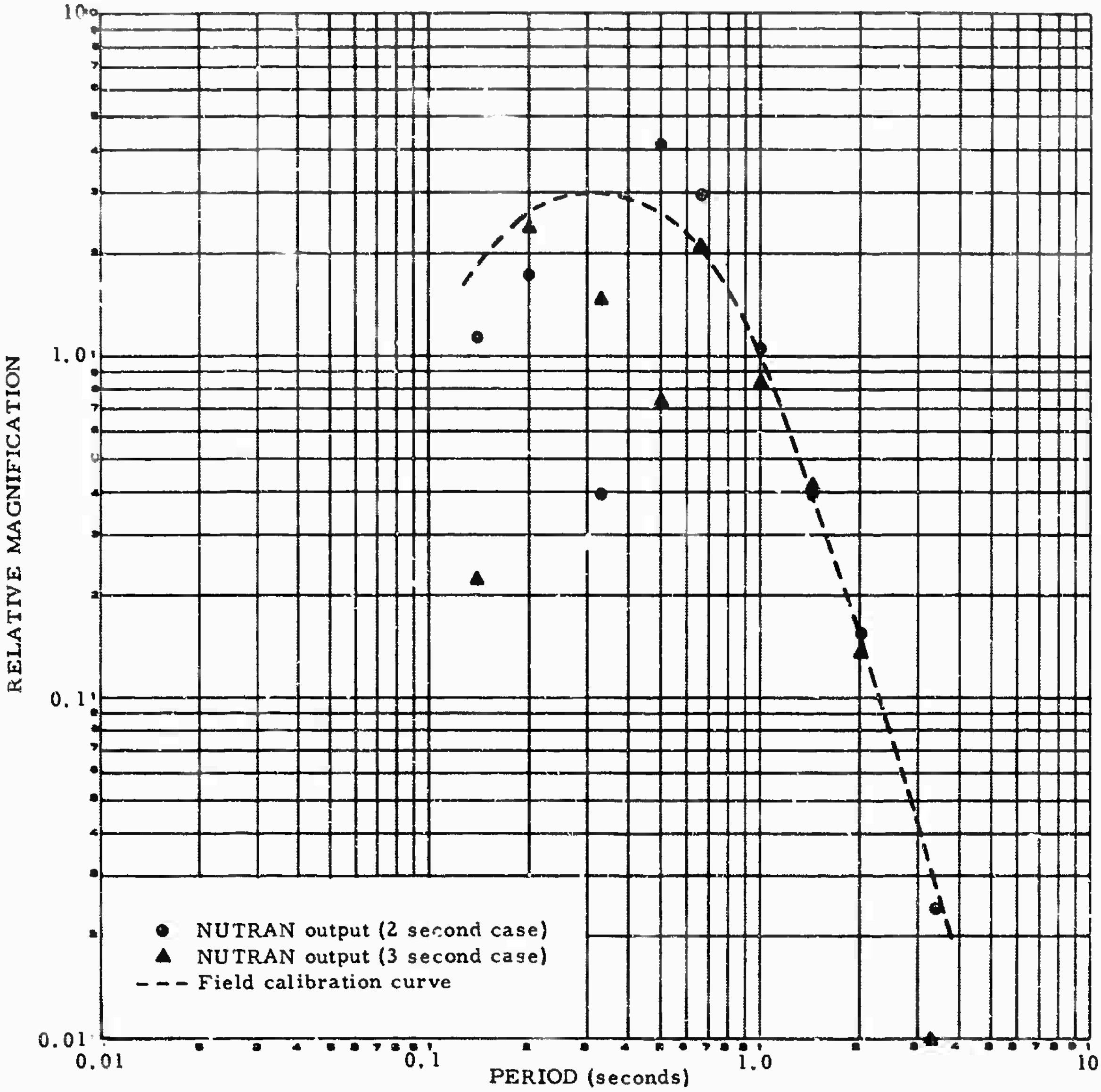

Figure 41. Unsmoothed calibration estimates at WO-AZ Z_4, 2 and 3 second cases

G 380

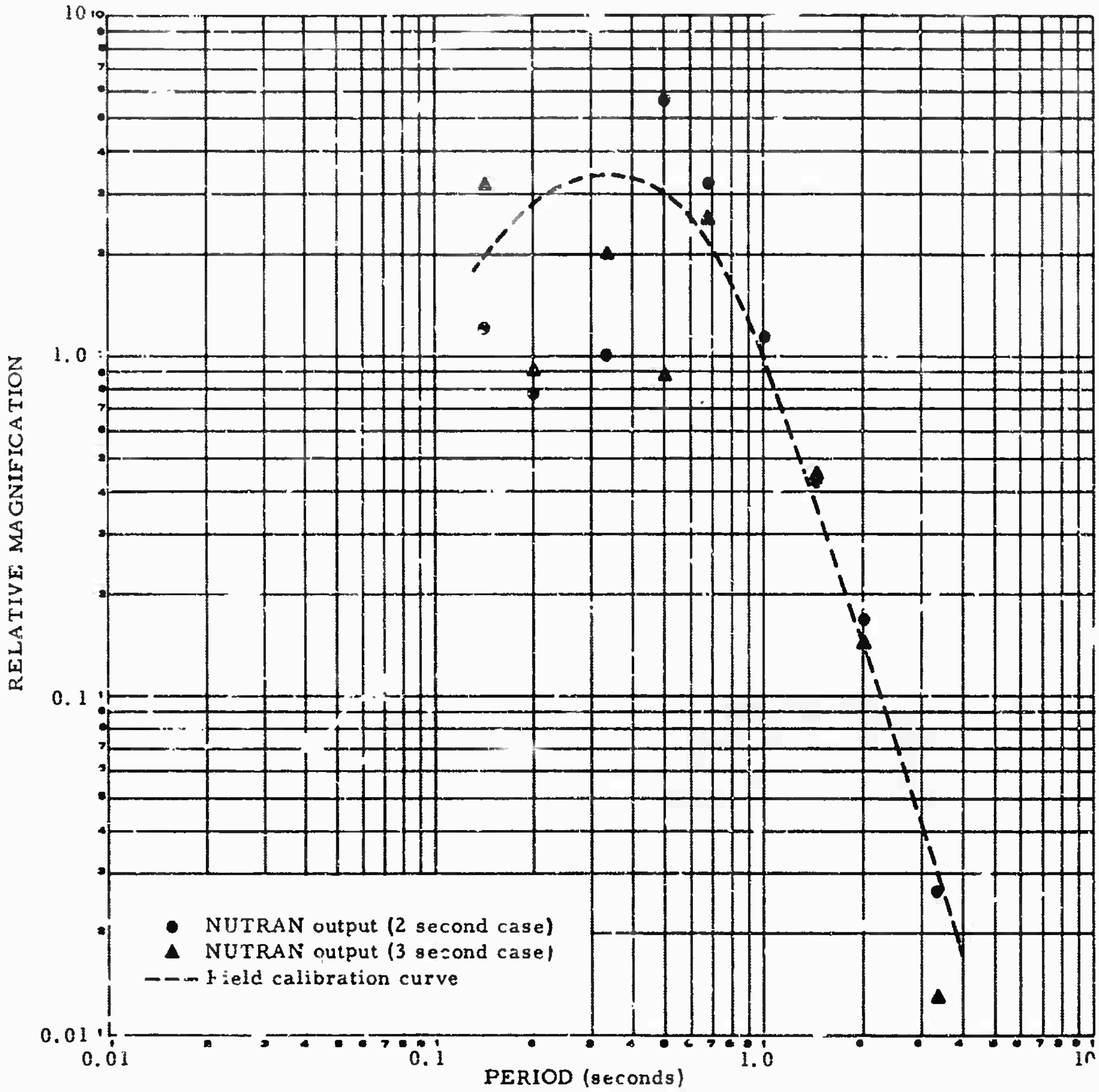

Figure 42. Unsmoothed calibration estimates at WO-AZ Z_5, 2 and 3 second cases

G 381

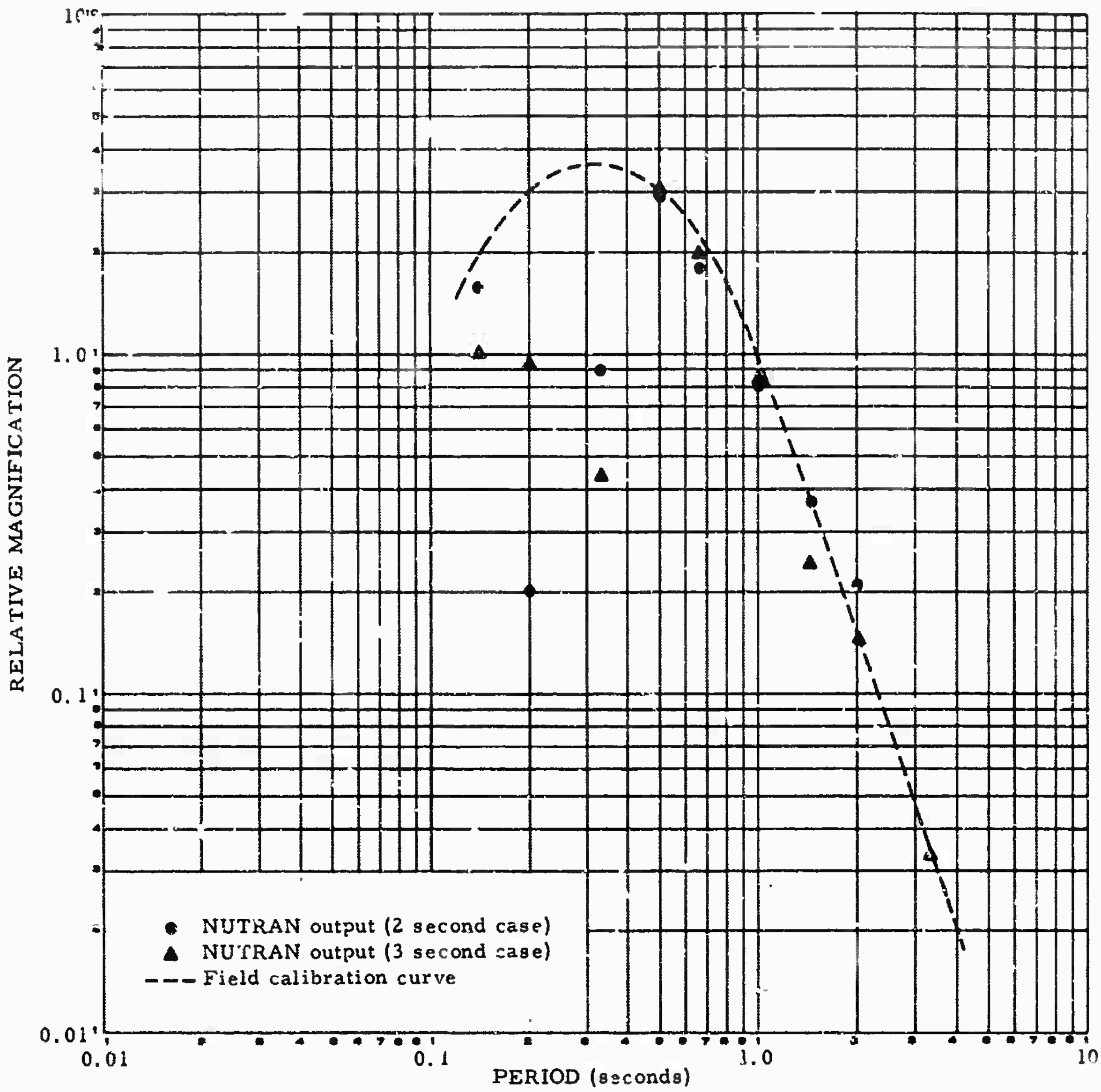

Figure 43. Unsmoothed calibration estimates at WO-AZ Z_6, 2 and 3 second cases

G 382

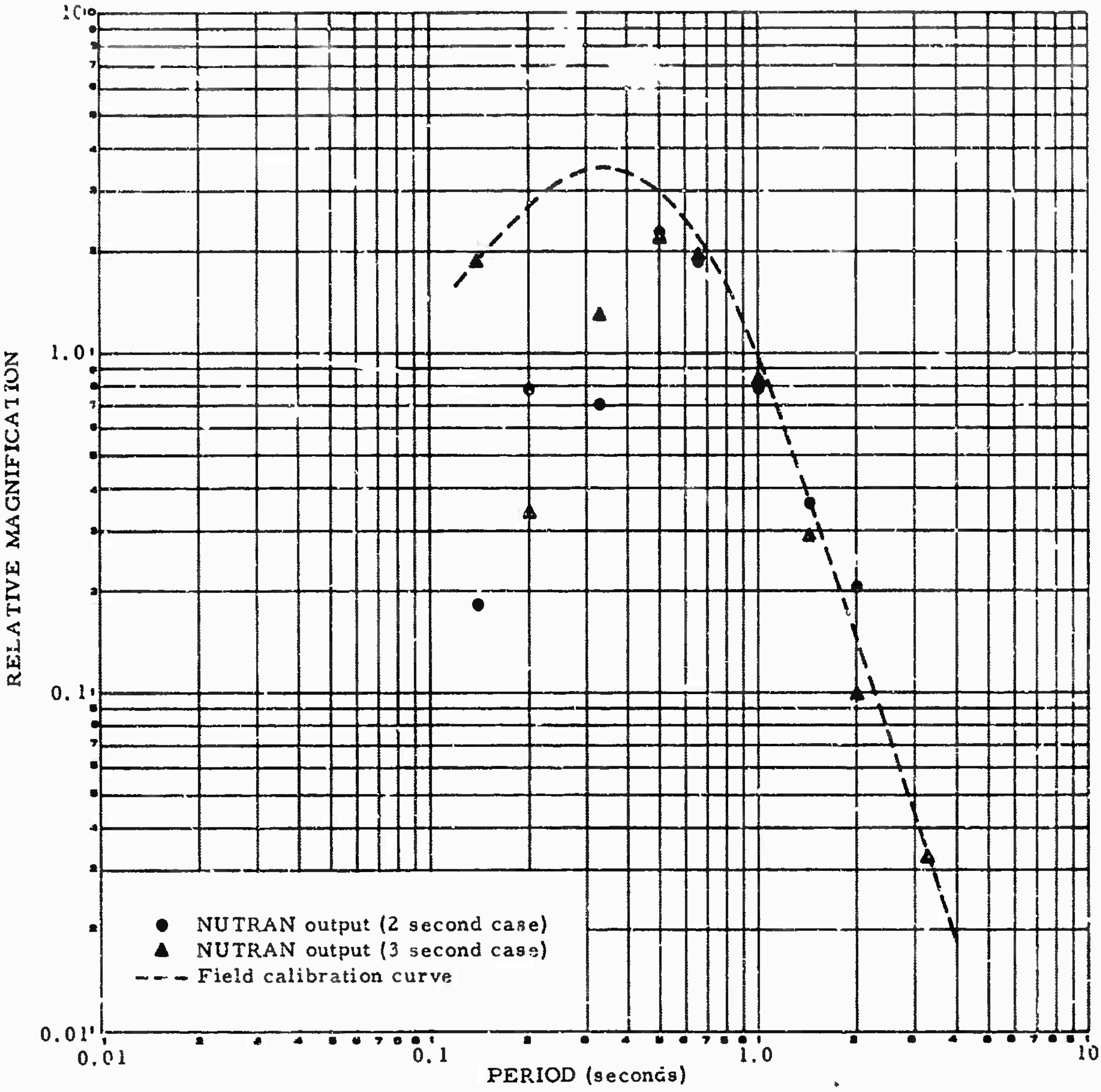

Figure 44. Unsmoothed calibration estimates at WO-AZ Z_7, 2 and 3 second cases

G 383

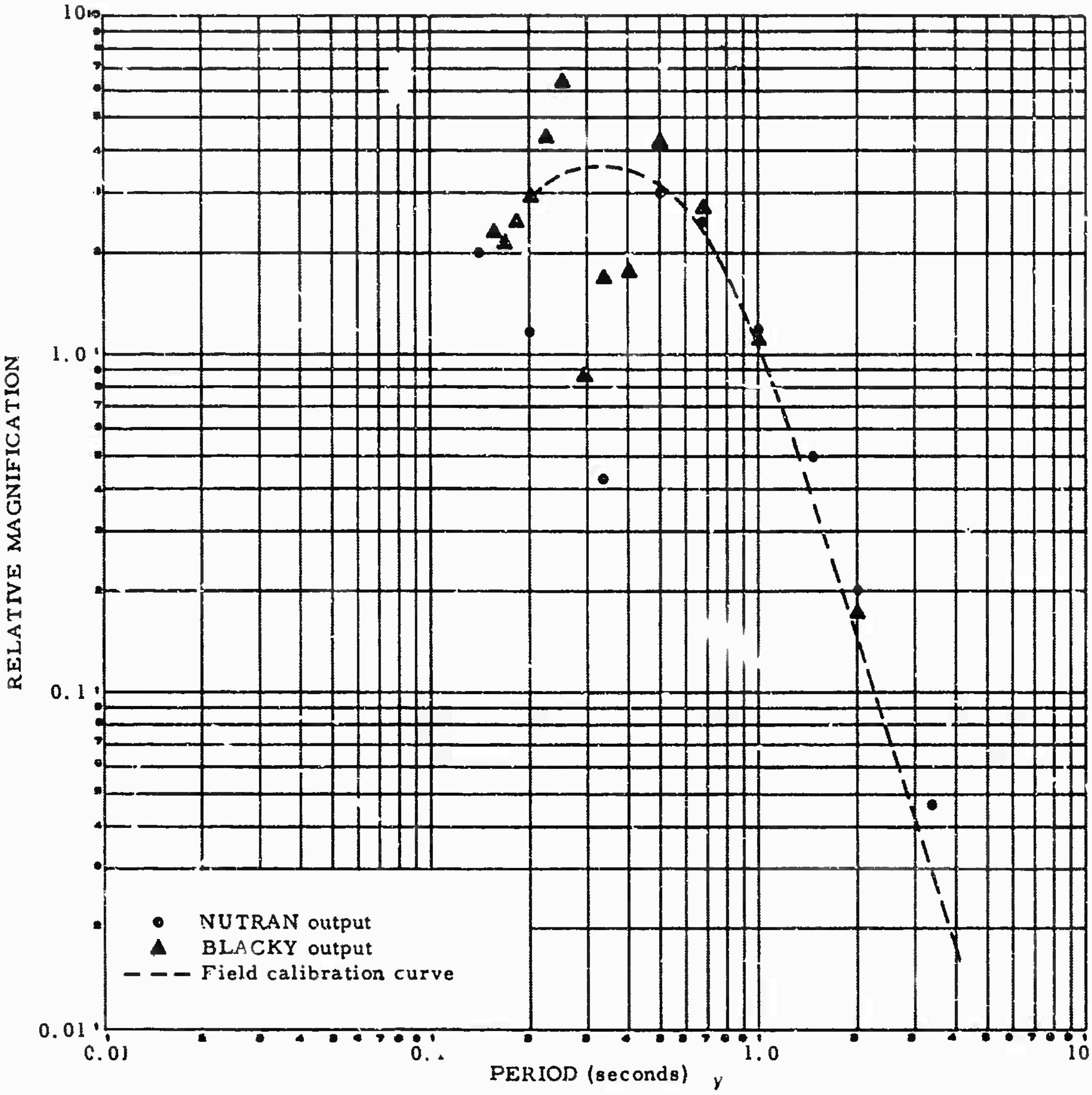

Figure 45. Smoothed calibration estimates at JR-AZ Z_2, 2 second case

G 384

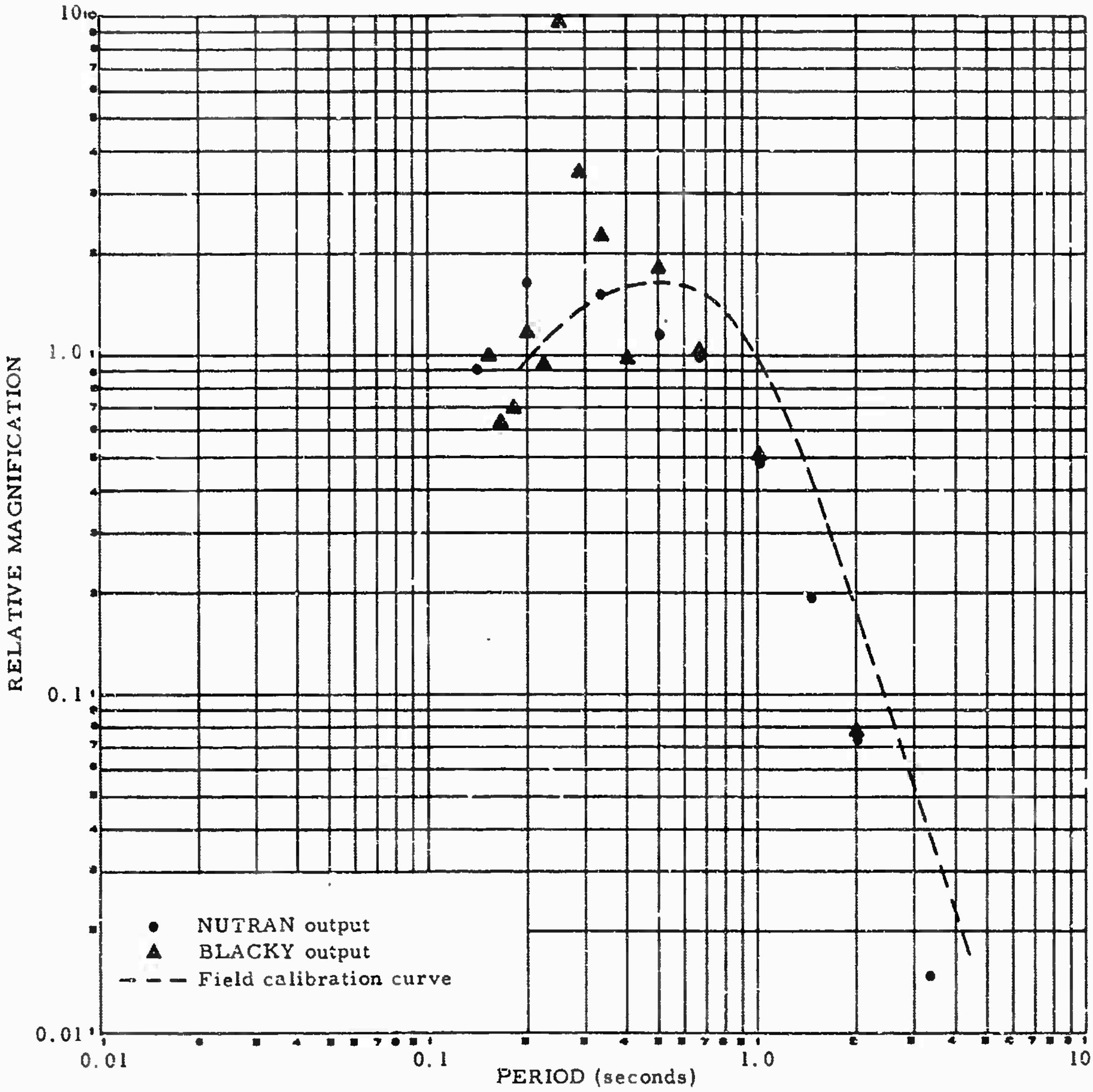

Figure 46. Smoothed calibration estimates at JR-AZ Z_3, 2 second case

G 385

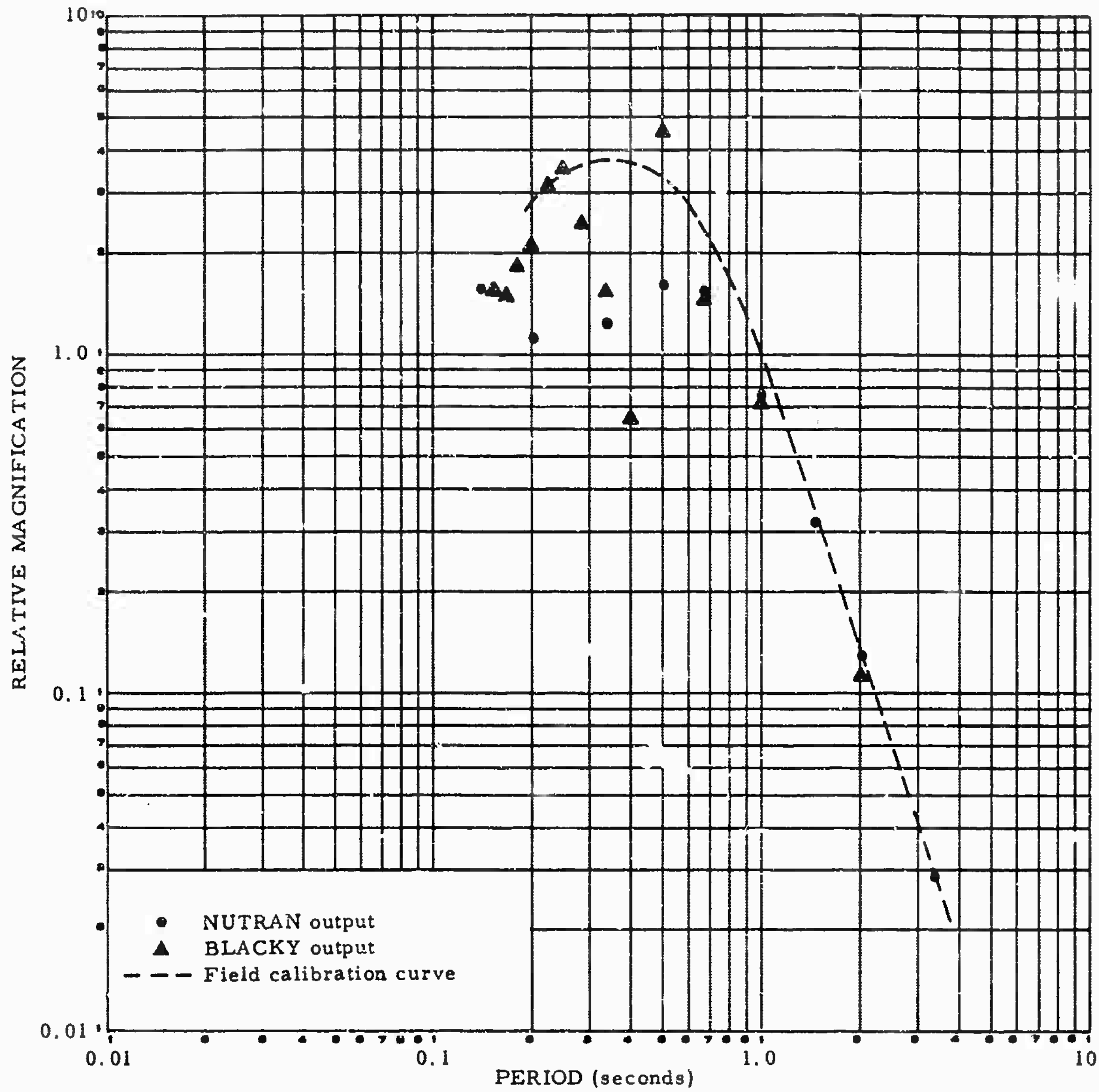

Figure 47. Smoothed calibration estimates at JR-AZ Z_4, 2 second case

G 386

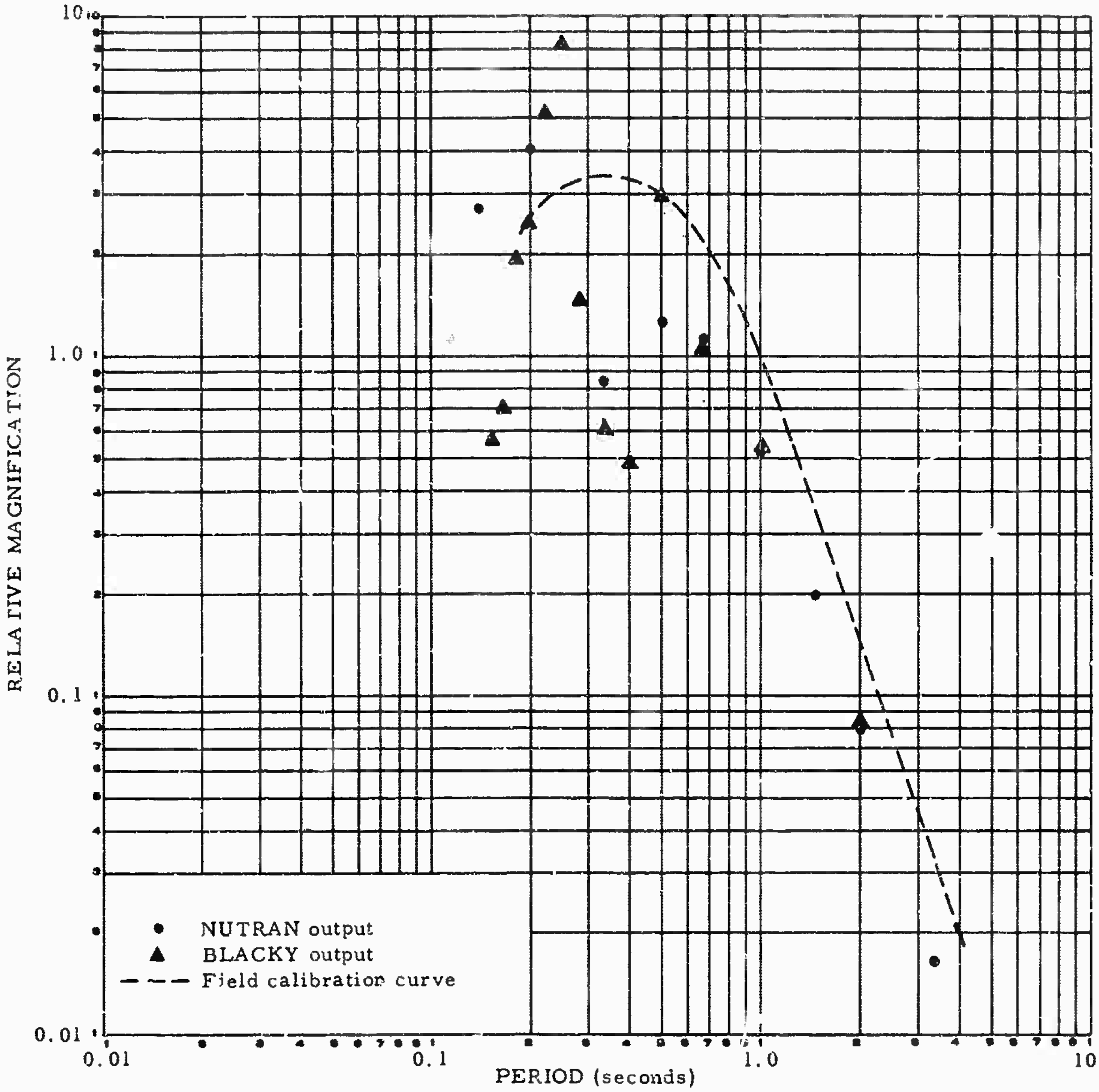

Figure 48. Smoothed calibration estimates at JR-AZ Z_5, 2 second case

G 387

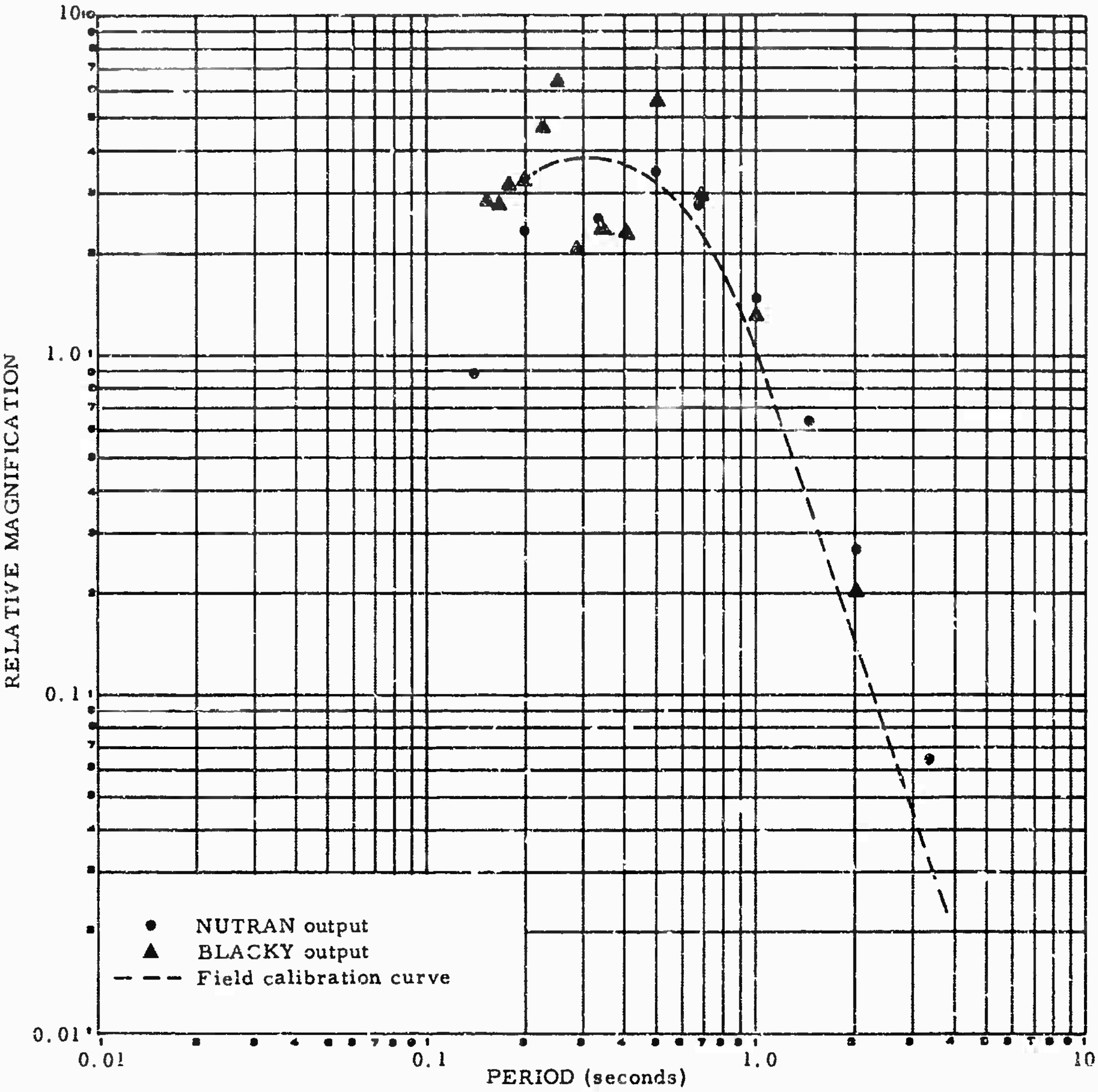

Figure 49. Smoothed calibration estimates at JR-AZ Z_6, 2 second case

G 388

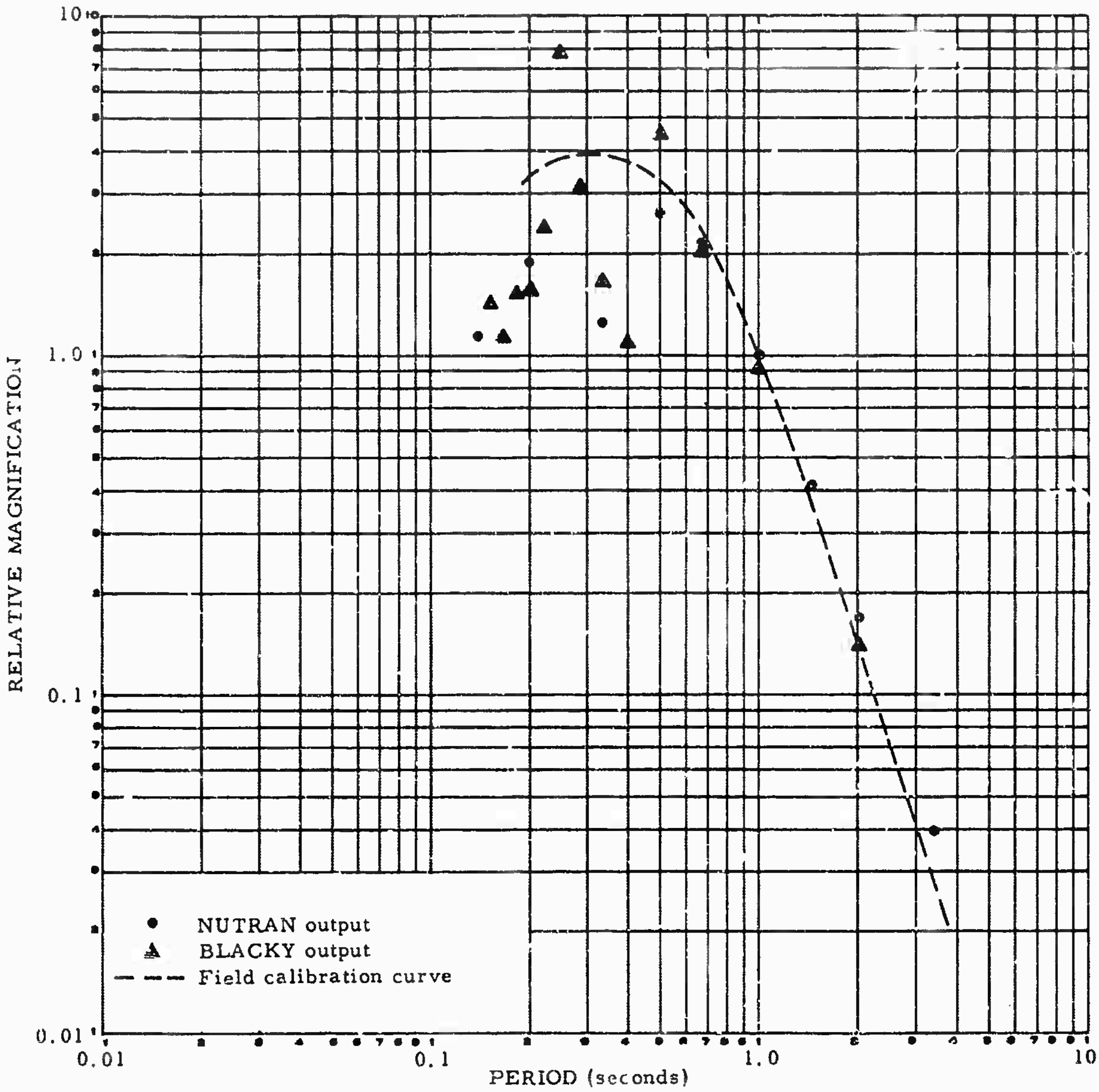

Figure 50. Smoothed calibration estimates at JR-AZ Z_7, 2 second case

G 389

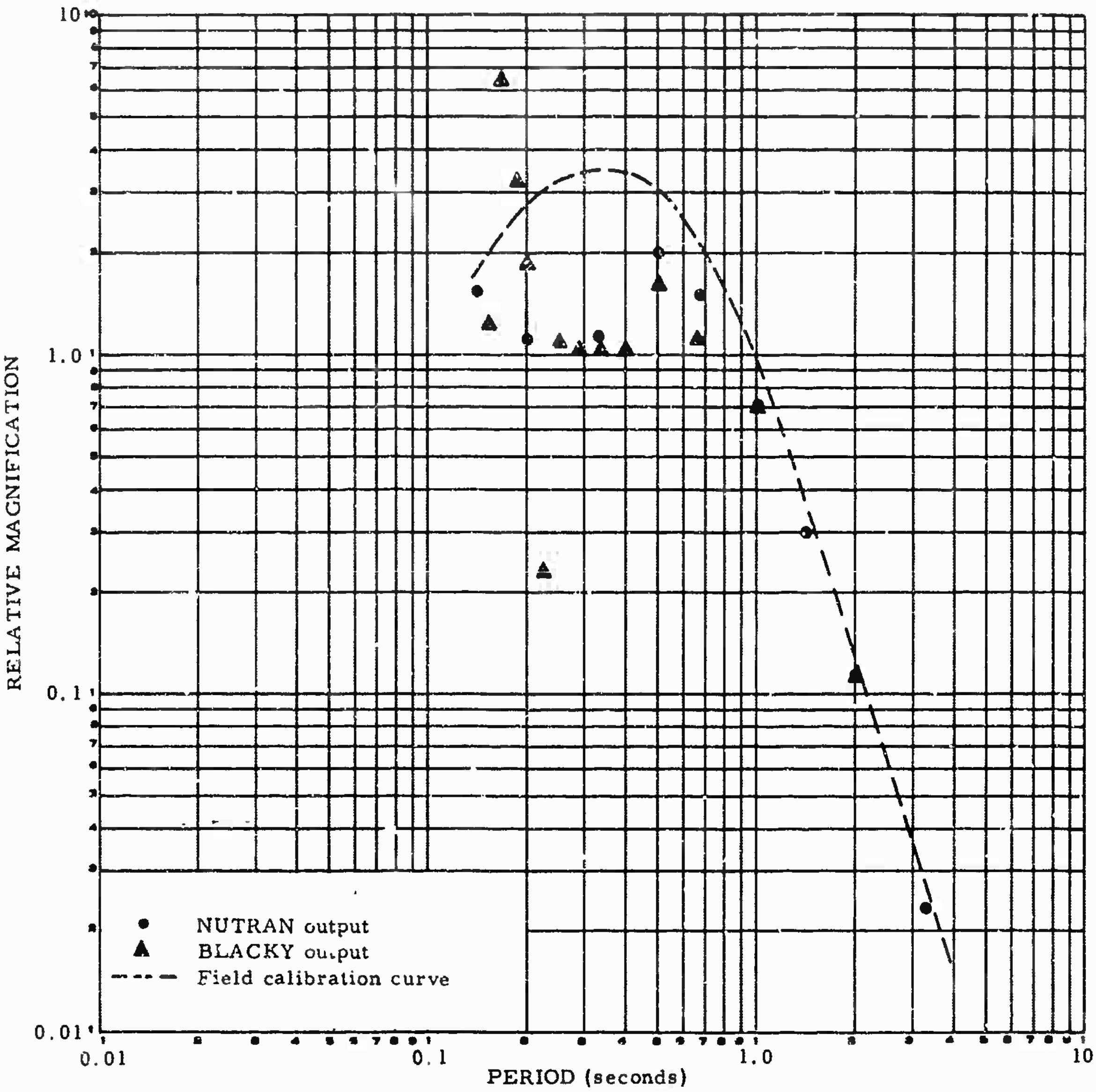

Figure 51. Smoothed calibration estimates at WO-AZ Z_2, 2 second case

G 390

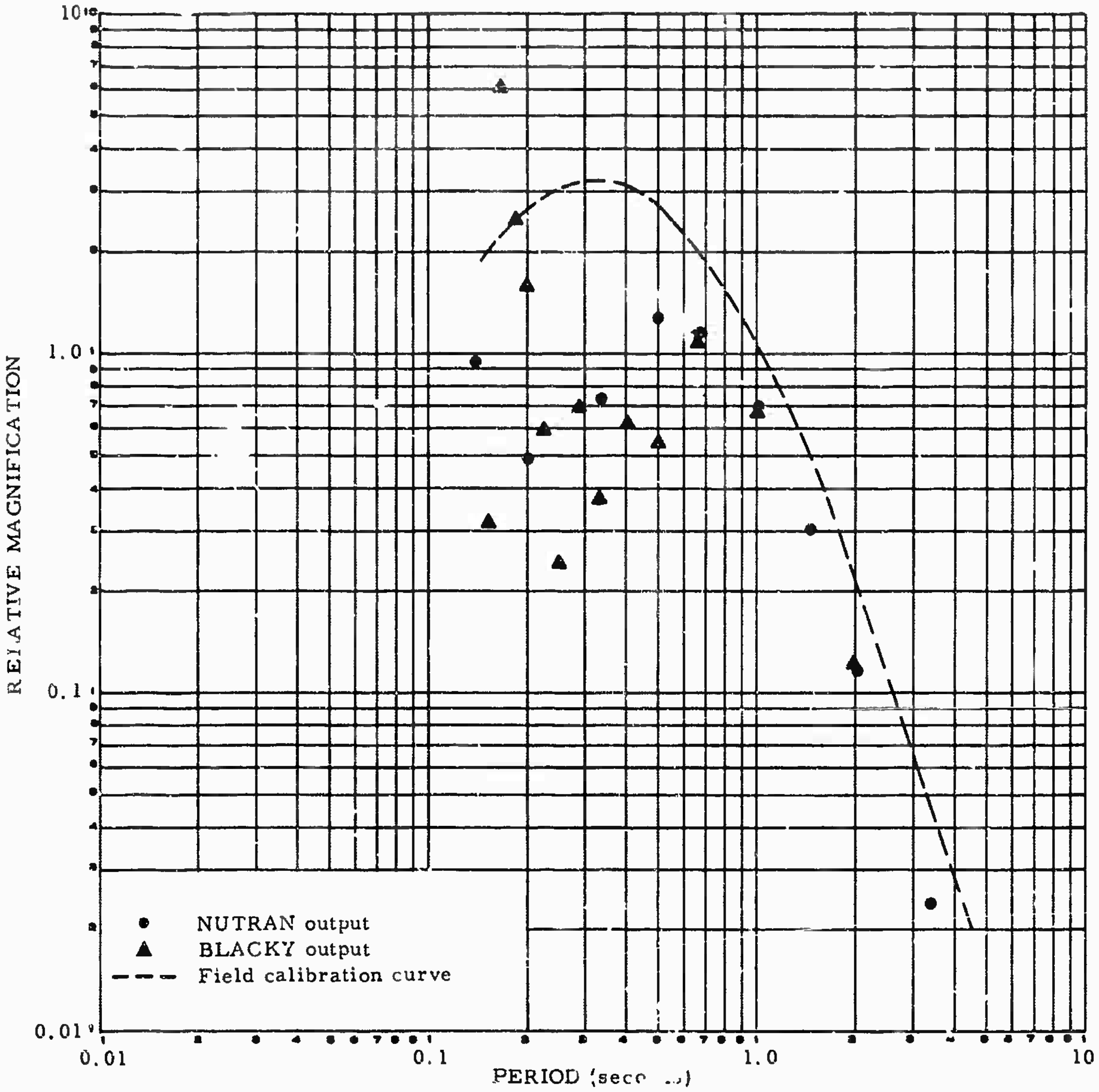

Figure 52. Smoothed calibration estimates at WO-AZ Z_3, 2 second case

G 391

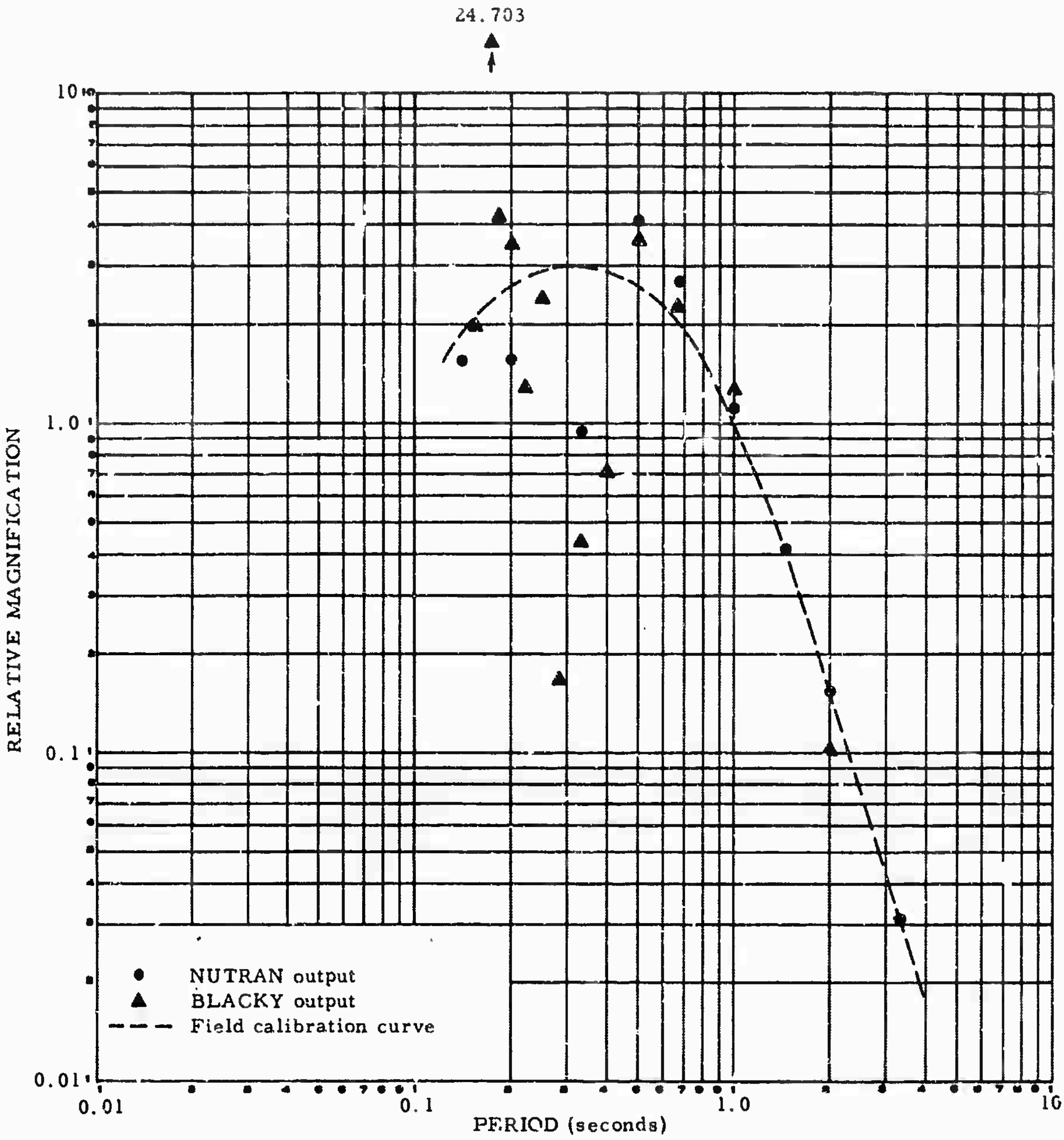

Figure 53. Smoothed calibration estimates at WO-AZ Z_4, 2 second case

G 392

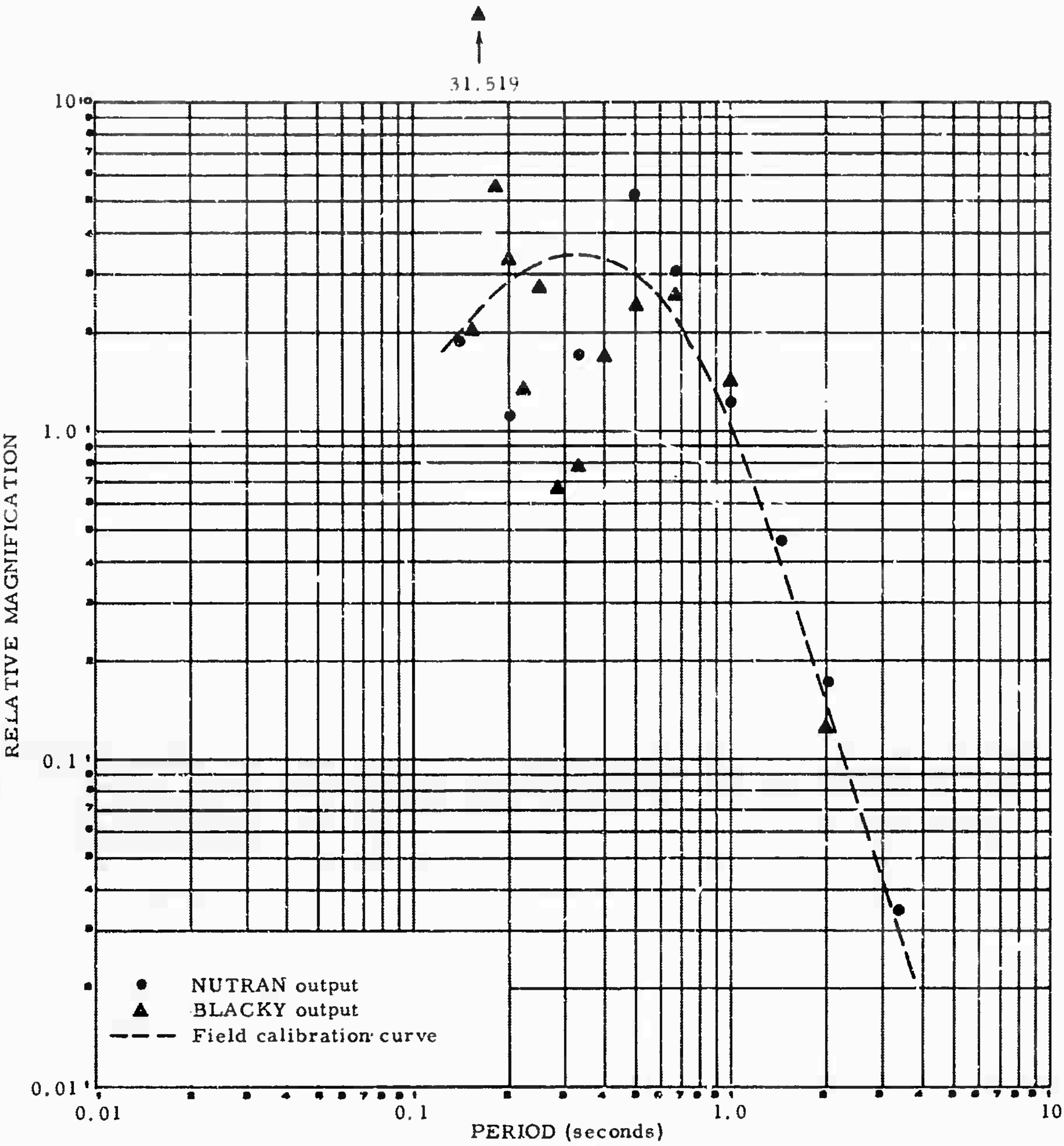

Figure 54. Smoothed calibration estimates at WC-AZ Z_5, 2 second case

G 393

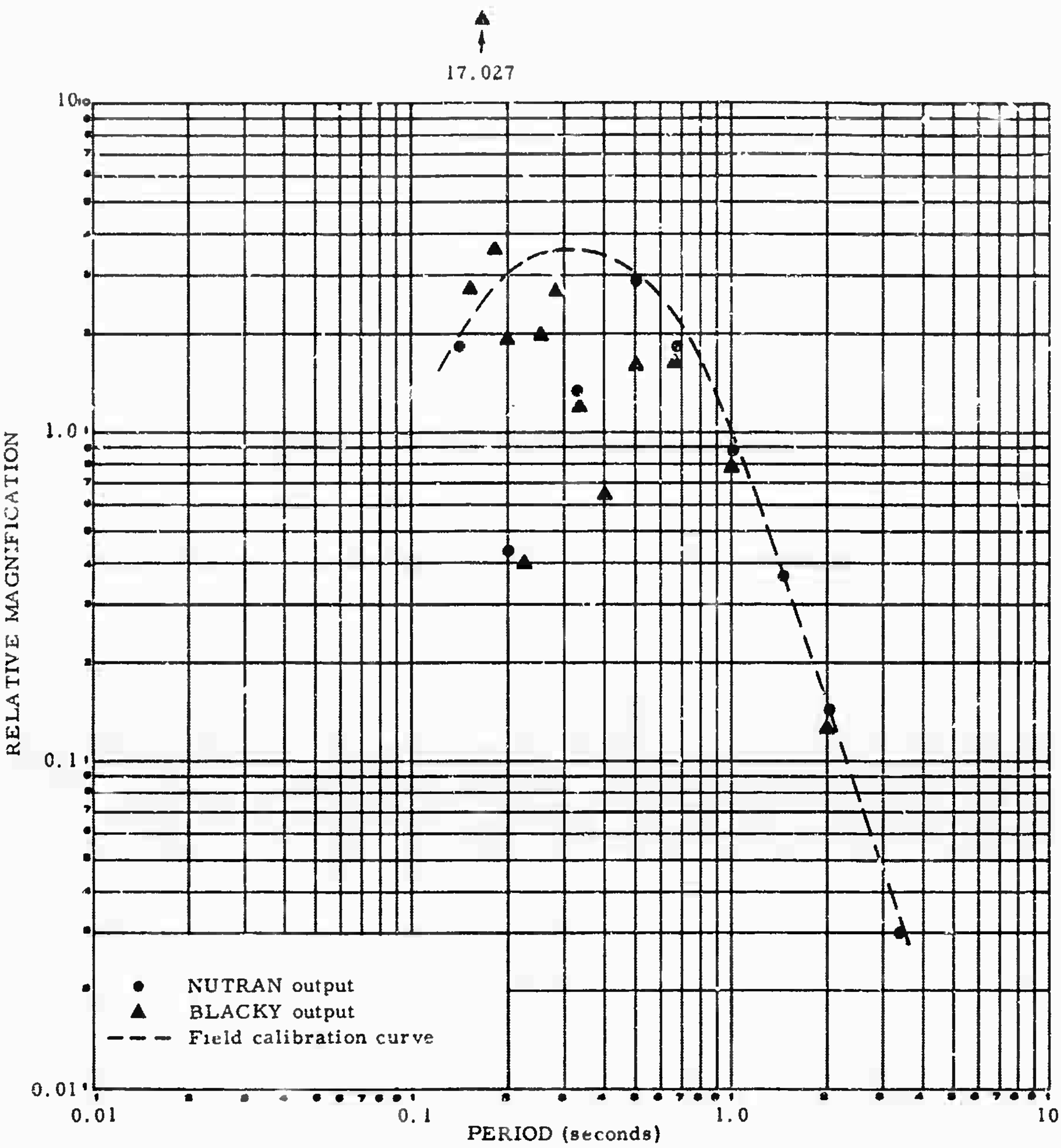

Figure 55. Smoothed calibration estimates at WO-AZ Z_6, 2 second case

G 394

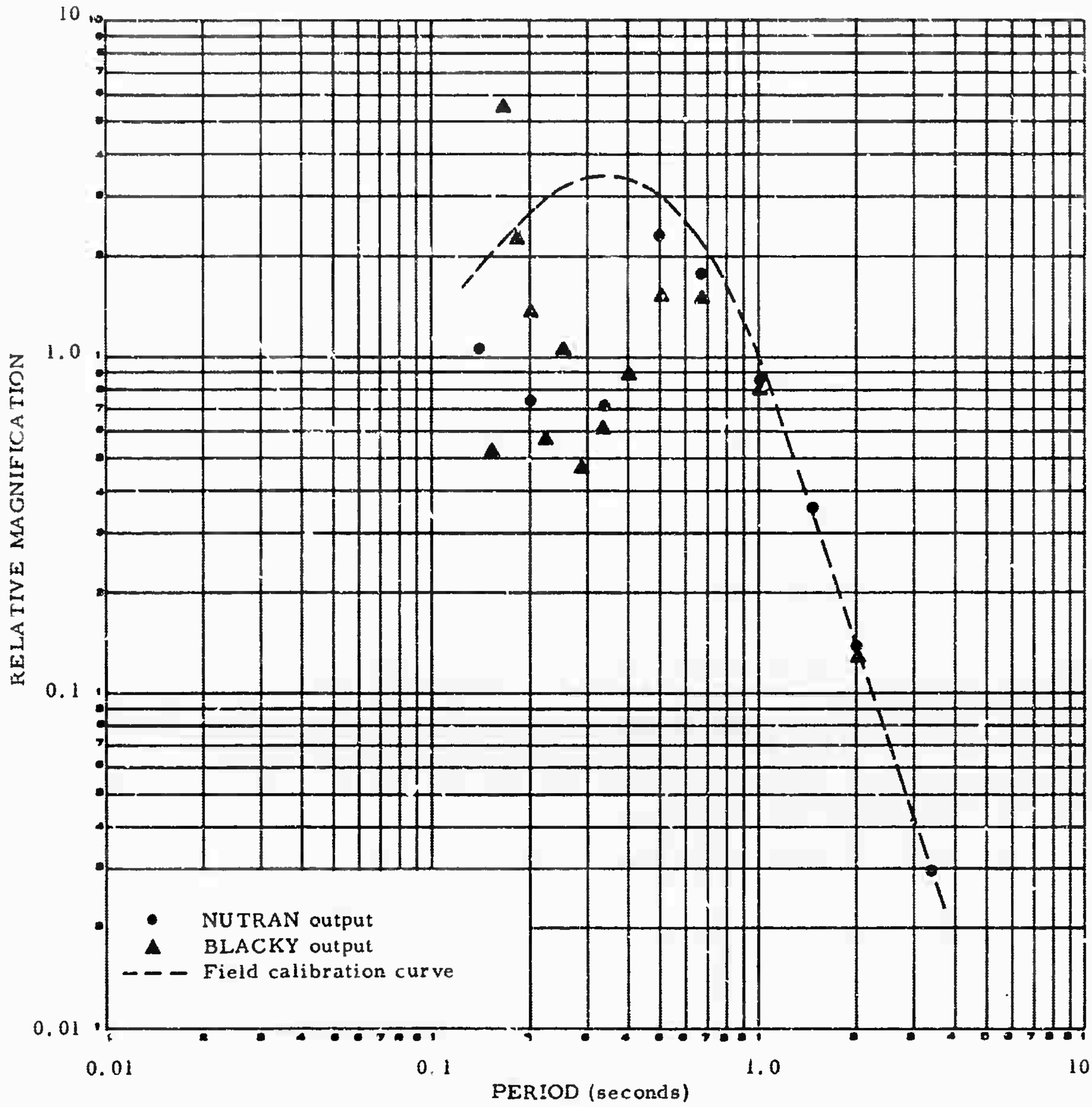

Figure 56. Smoothed calibration estimates at WO-AZ Z_7, 2 second case

G 395

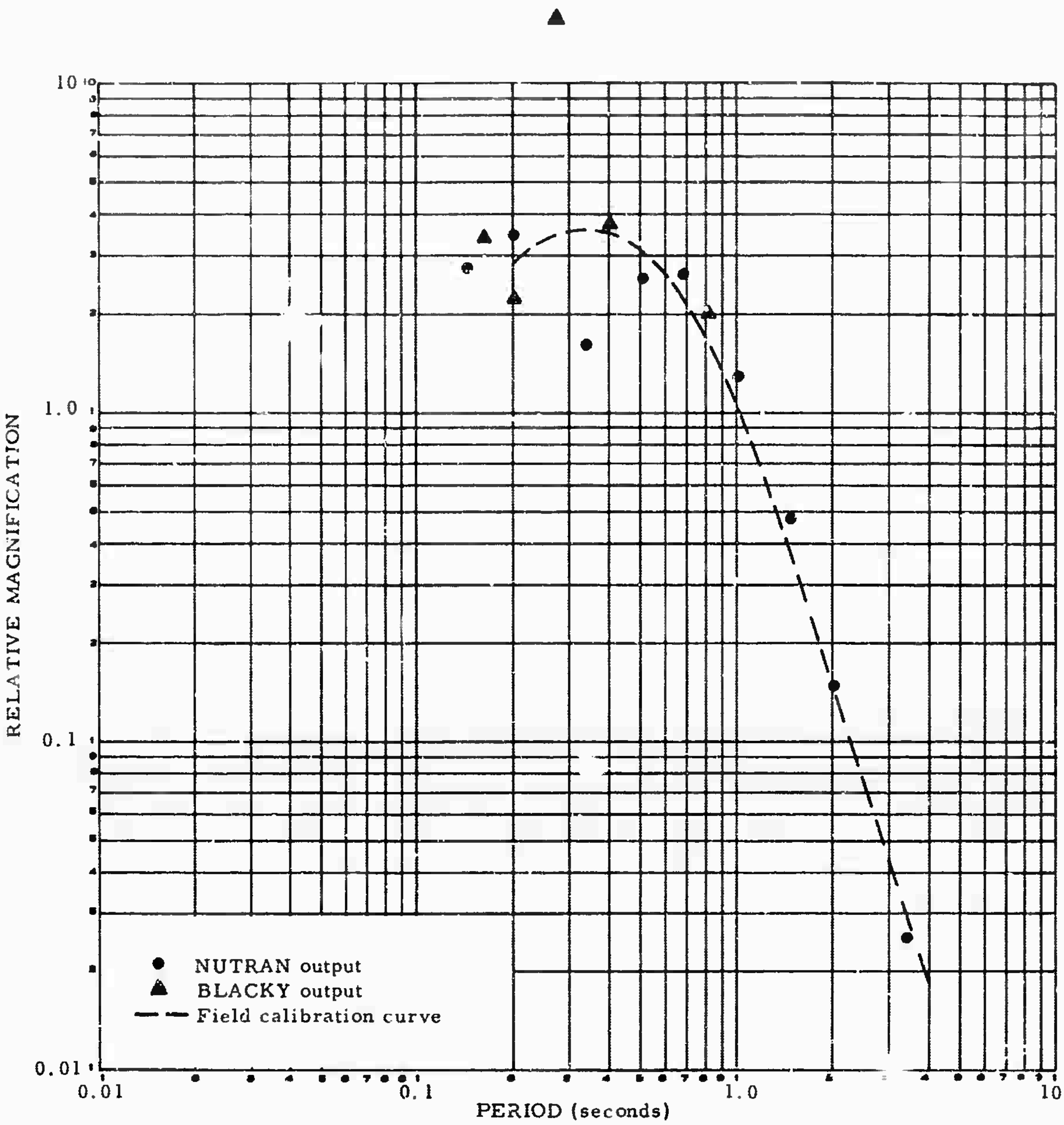

Figure 57. Smoothed calibration estimates at JR-AZ Z_2, 3 second case

G 396

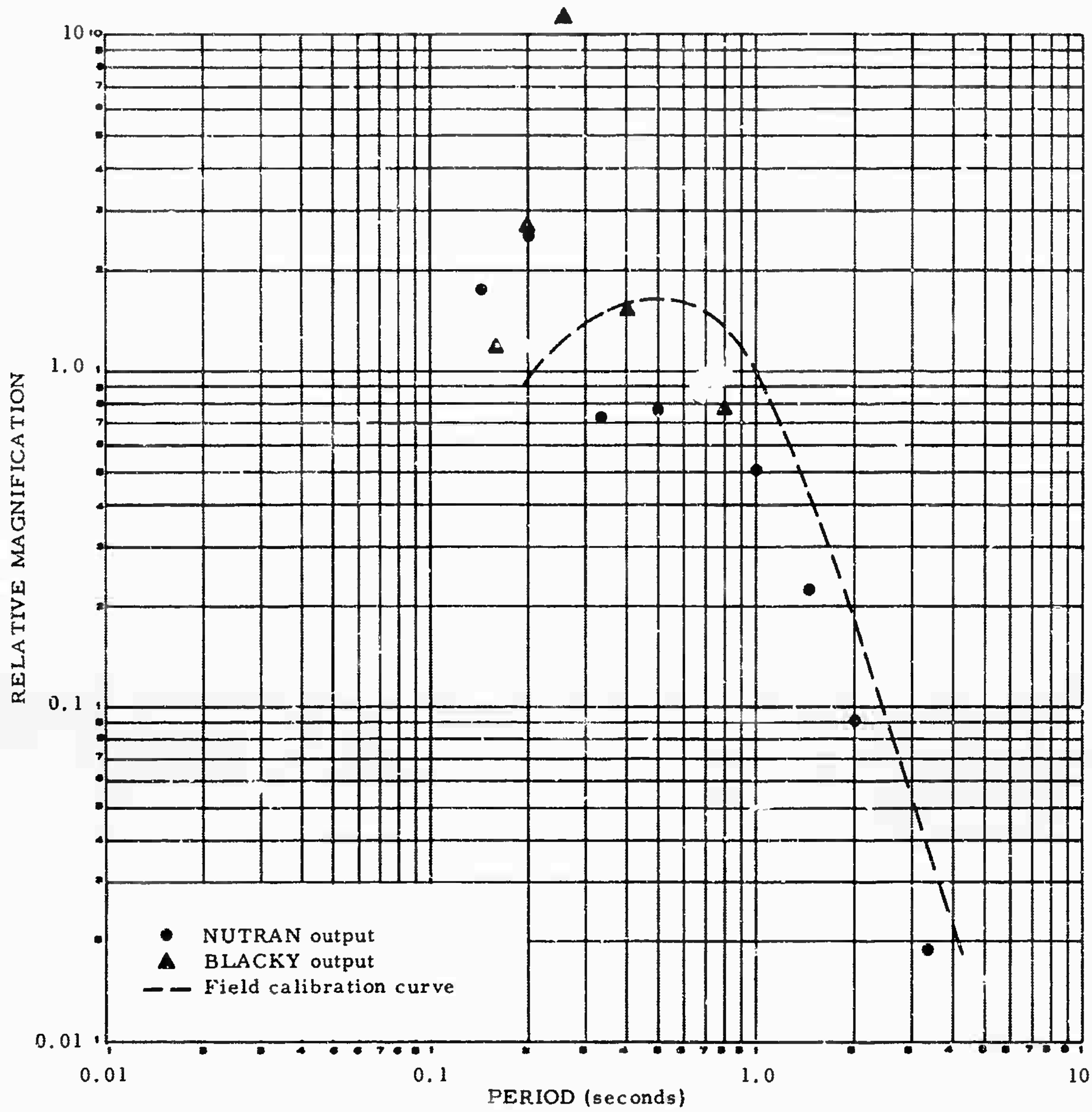

Figure 58. Smoothed calibration estimates at JR-AZ Z_3,
3 second case

G 397

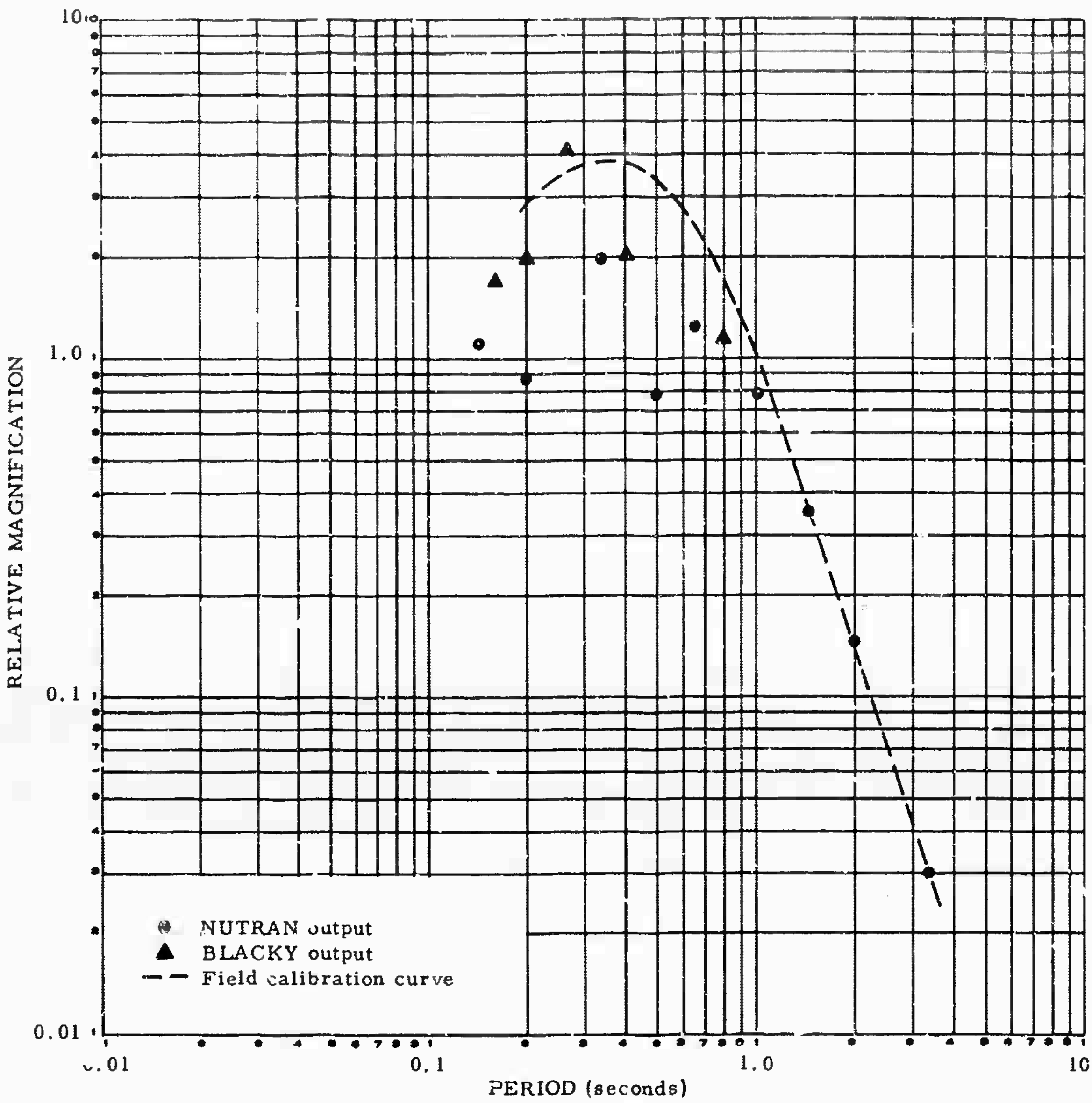

Figure 59. Smoothed calibration estimates at JR-AZ Z_4, 3 second case

G 398

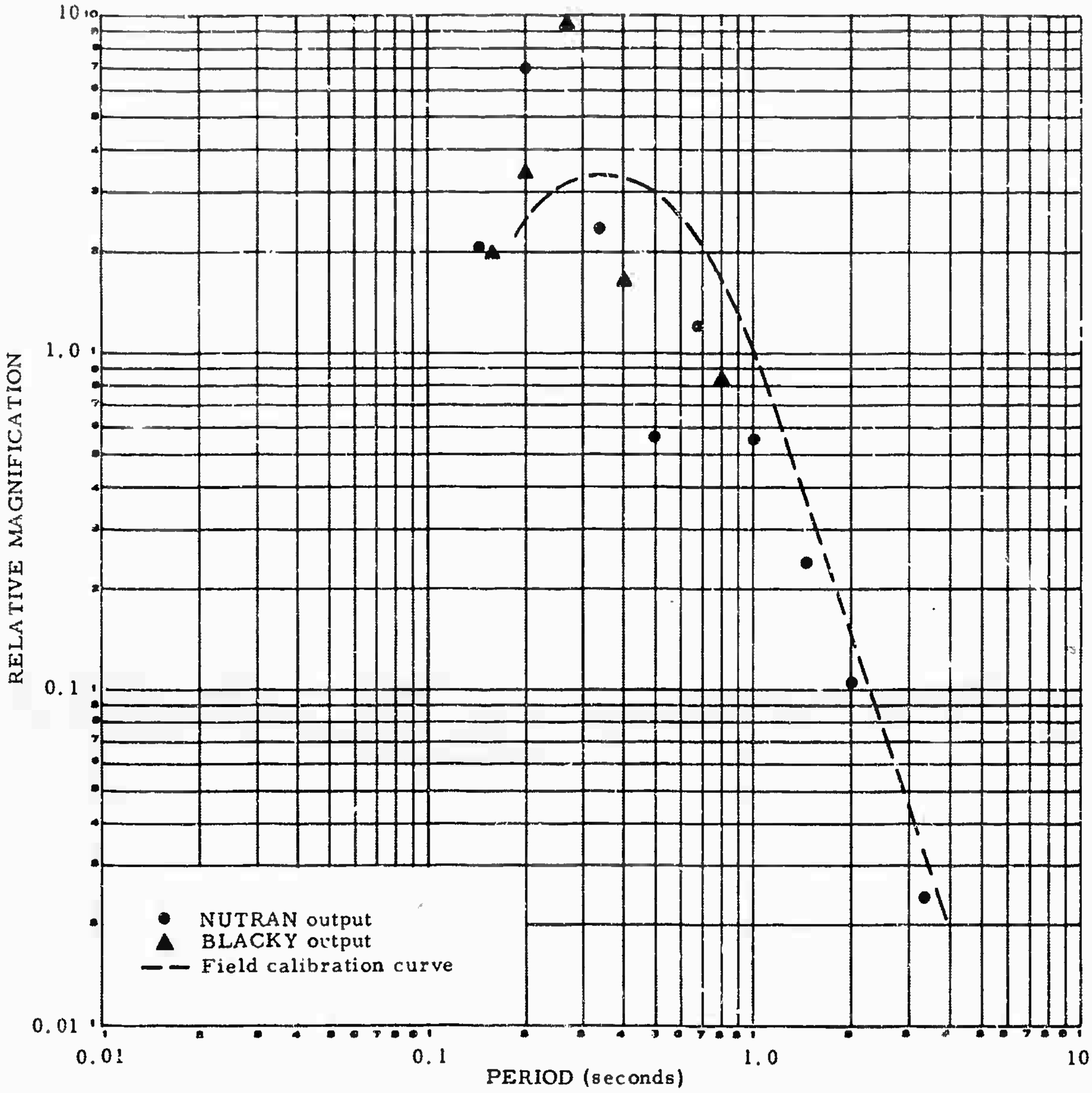

Figure 60. Smoothed calibration estimates at JR-AZ Z_5, 3 second case

G 399

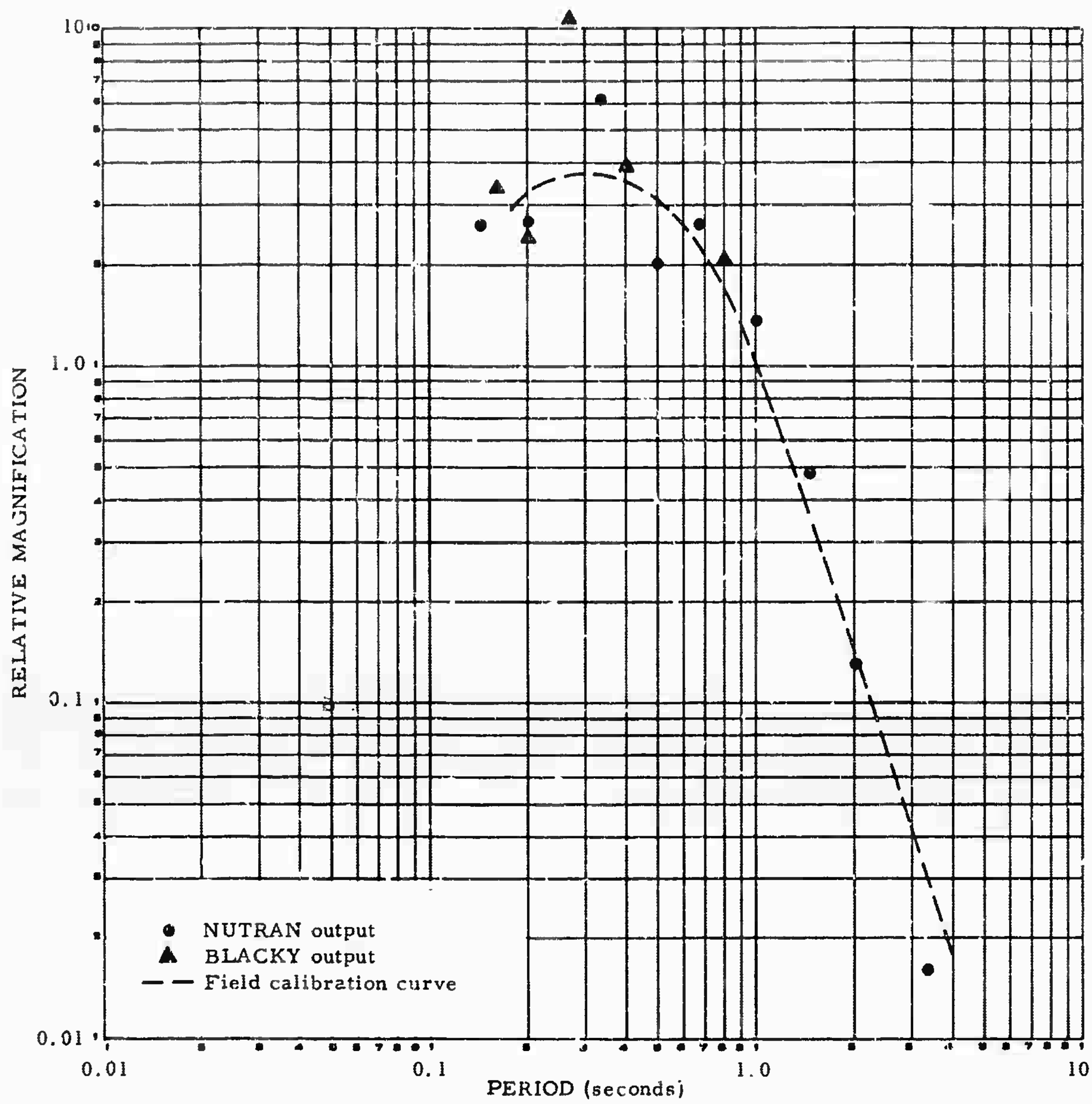

Figure 61. Smoothed calibration estimates at JR-AZ Z_6, 3 second case

G 400

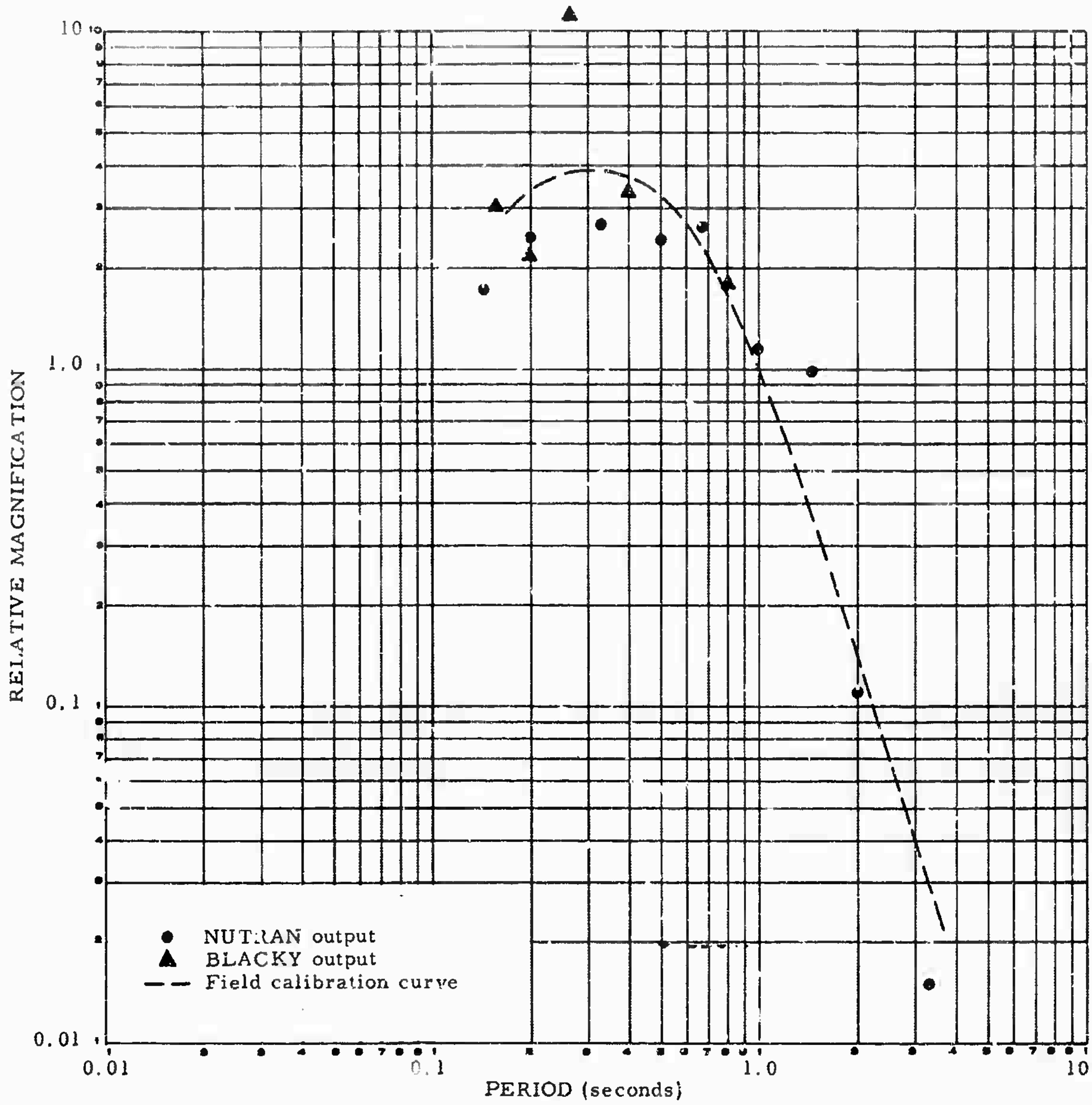

Figure 62. Smoothed calibration estimates at JR-AZ Z_7, 3 second case

G 401

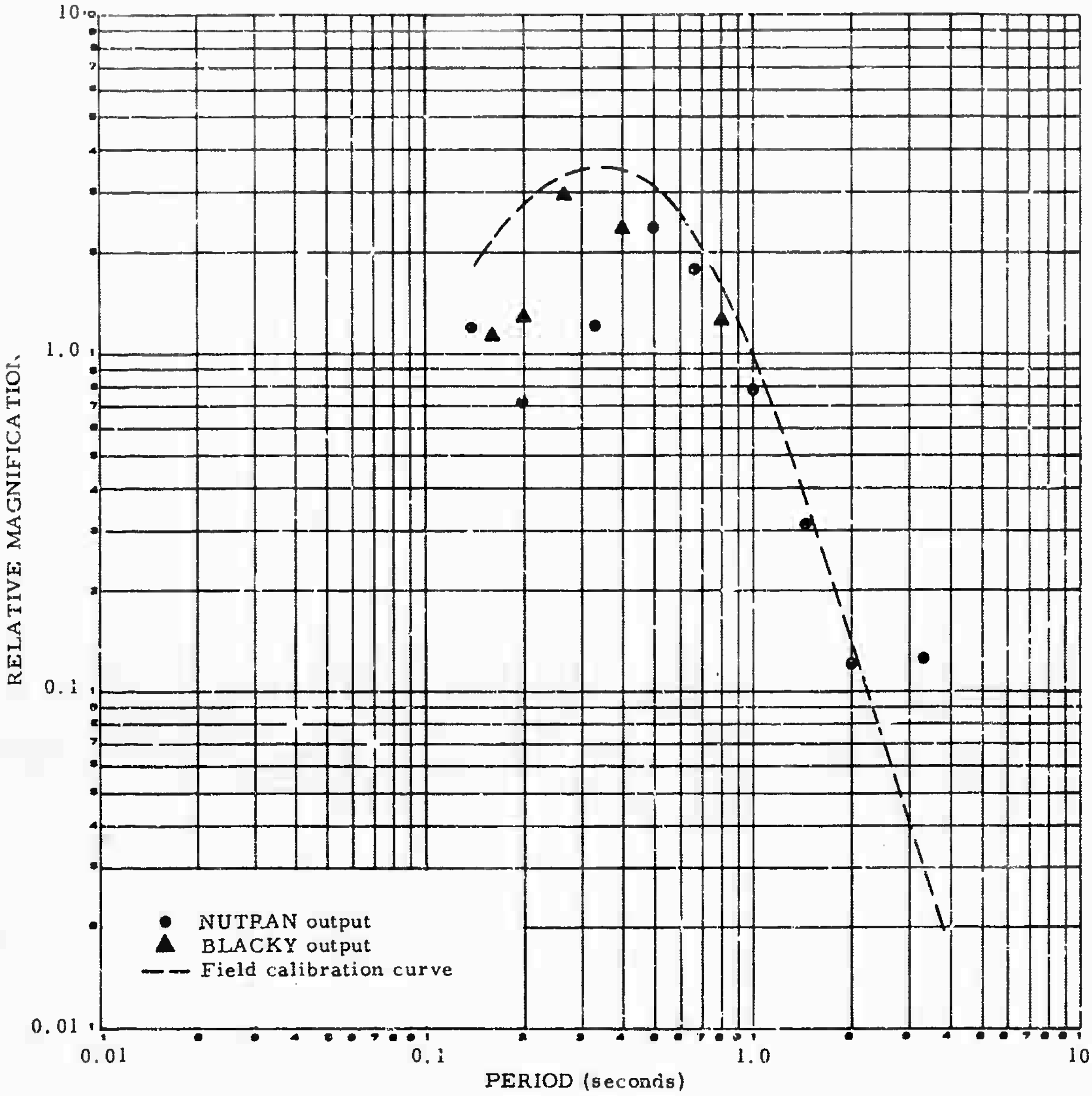

Figure 63. Smoothed calibration estimates at WO-AZ Z_2, 3 second case

G 402

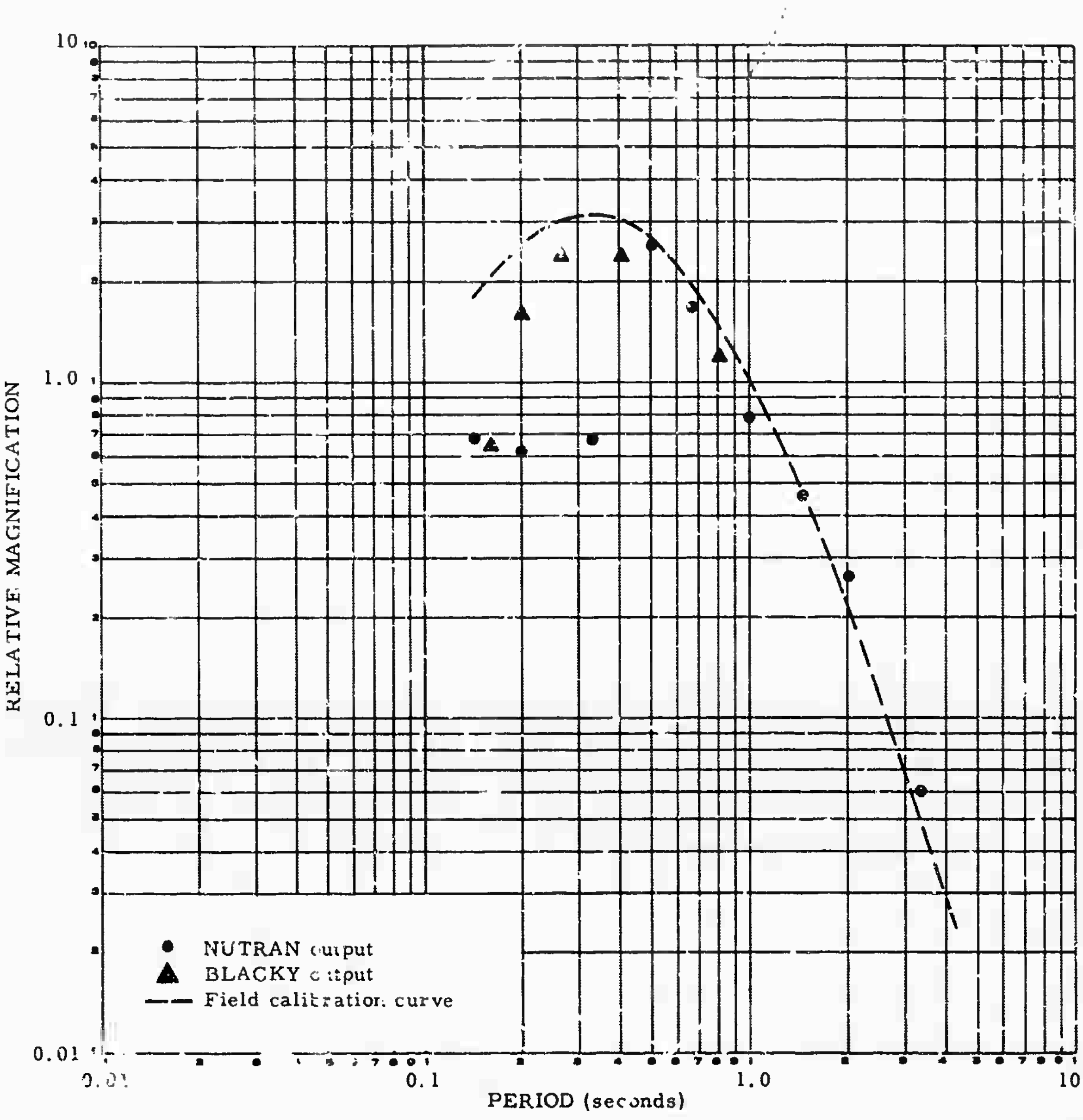

Figure 64. Smoothed calibration estimates at WO-AZ Z_3, 3 second case

G 403

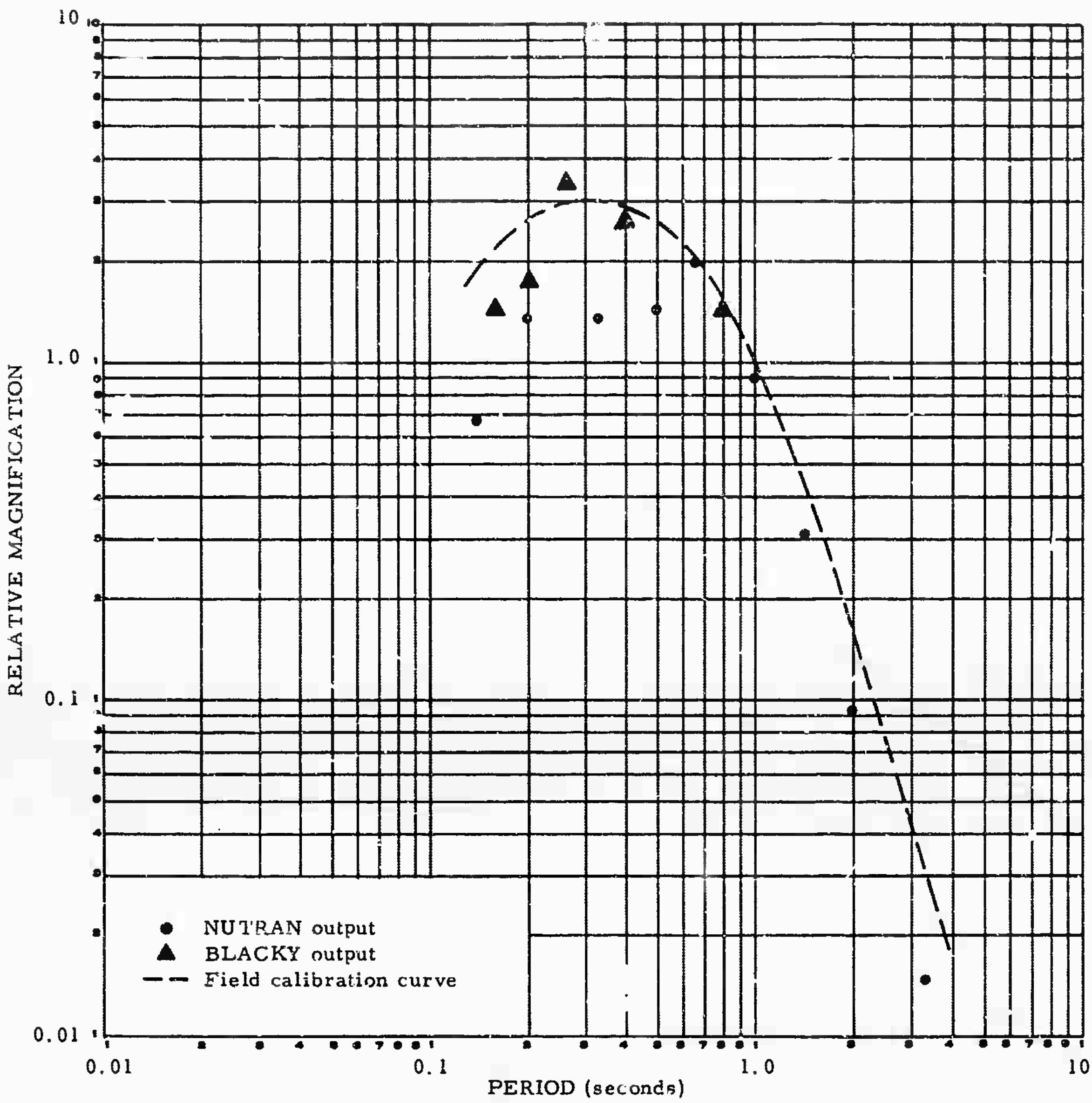

Figure 65. Smoothed calibration estimates at WO-AZ Z_4, 3 second case

G 404

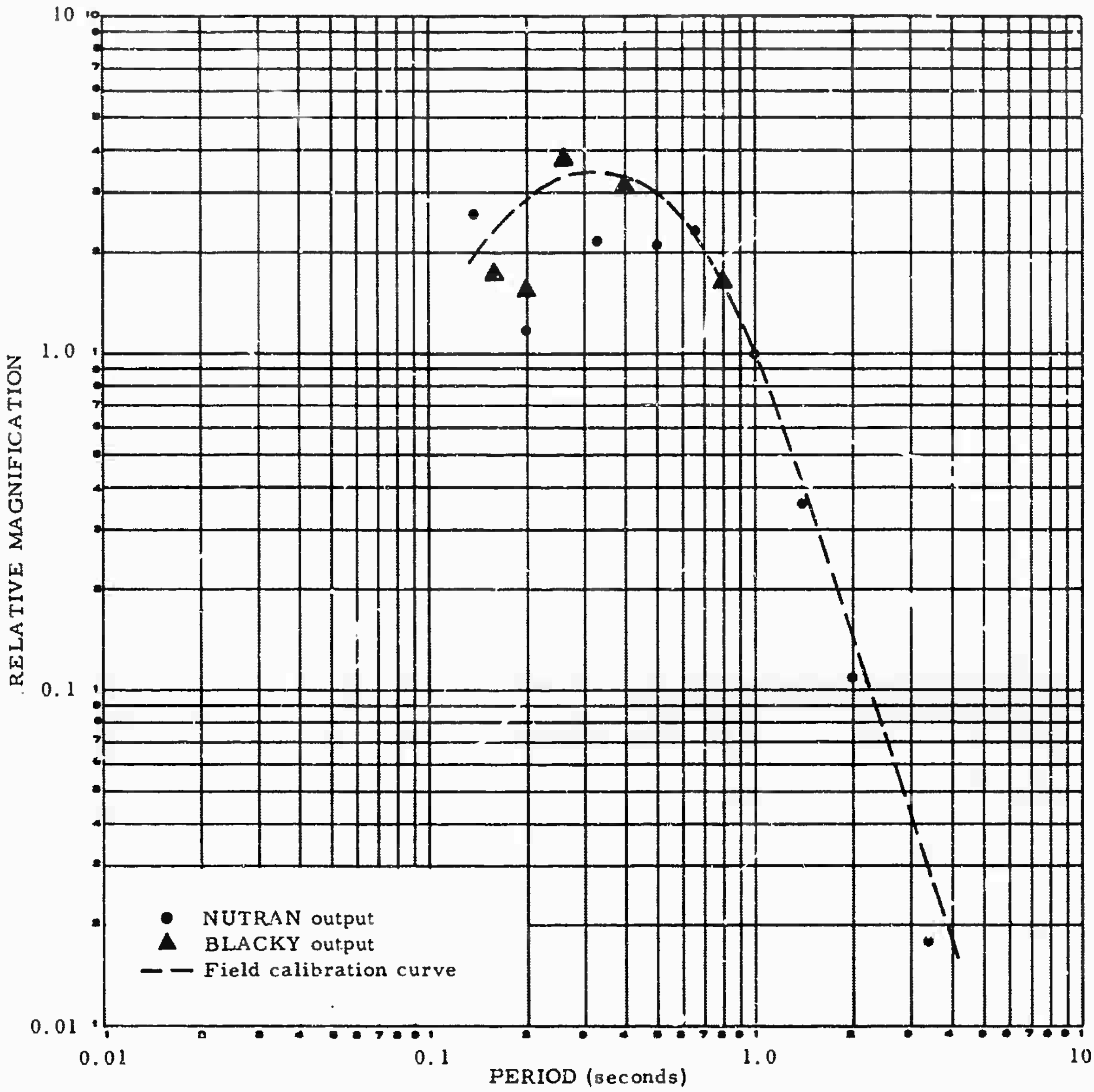

Figure 66. Smoothed calibration estimates at WO-AZ Z_5, 3 second case

G 405

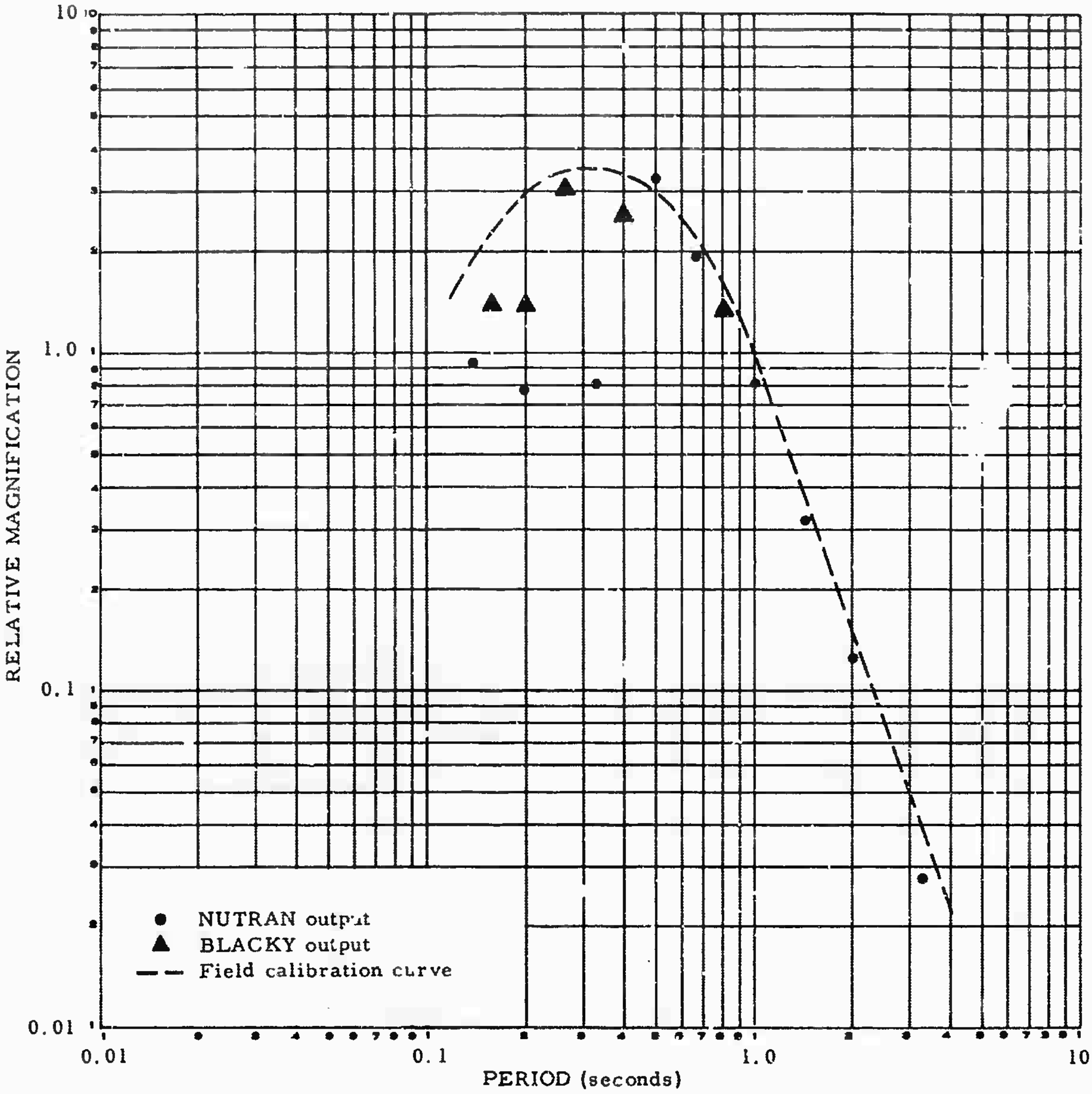

Figure 67. Smoothed calibration estimates at WO-AZ Z_6, 3 second case

G 406

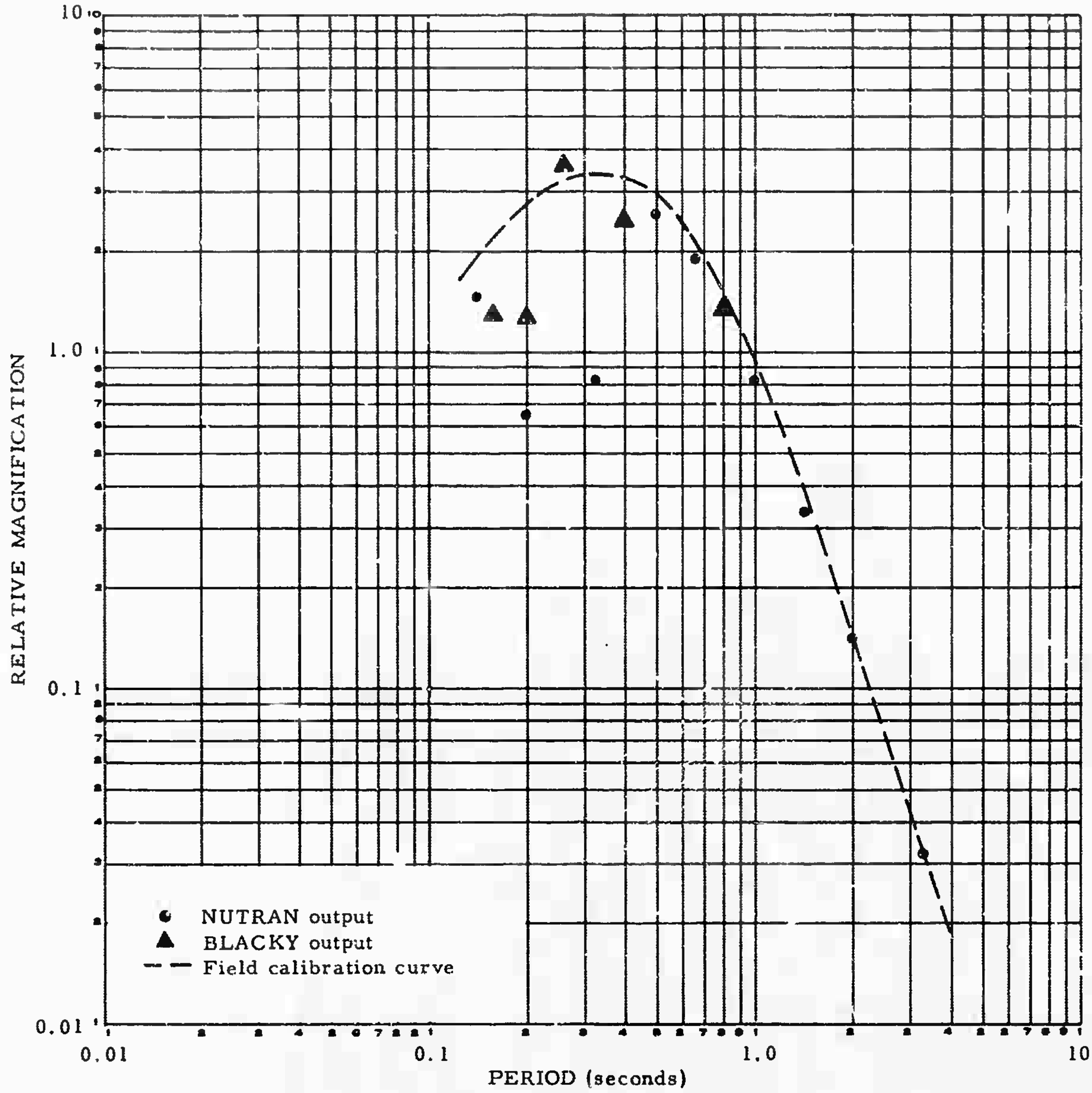

Figure 68. Smoothed calibration estimates at WO-AZ Z_7, 3 second case

G 407

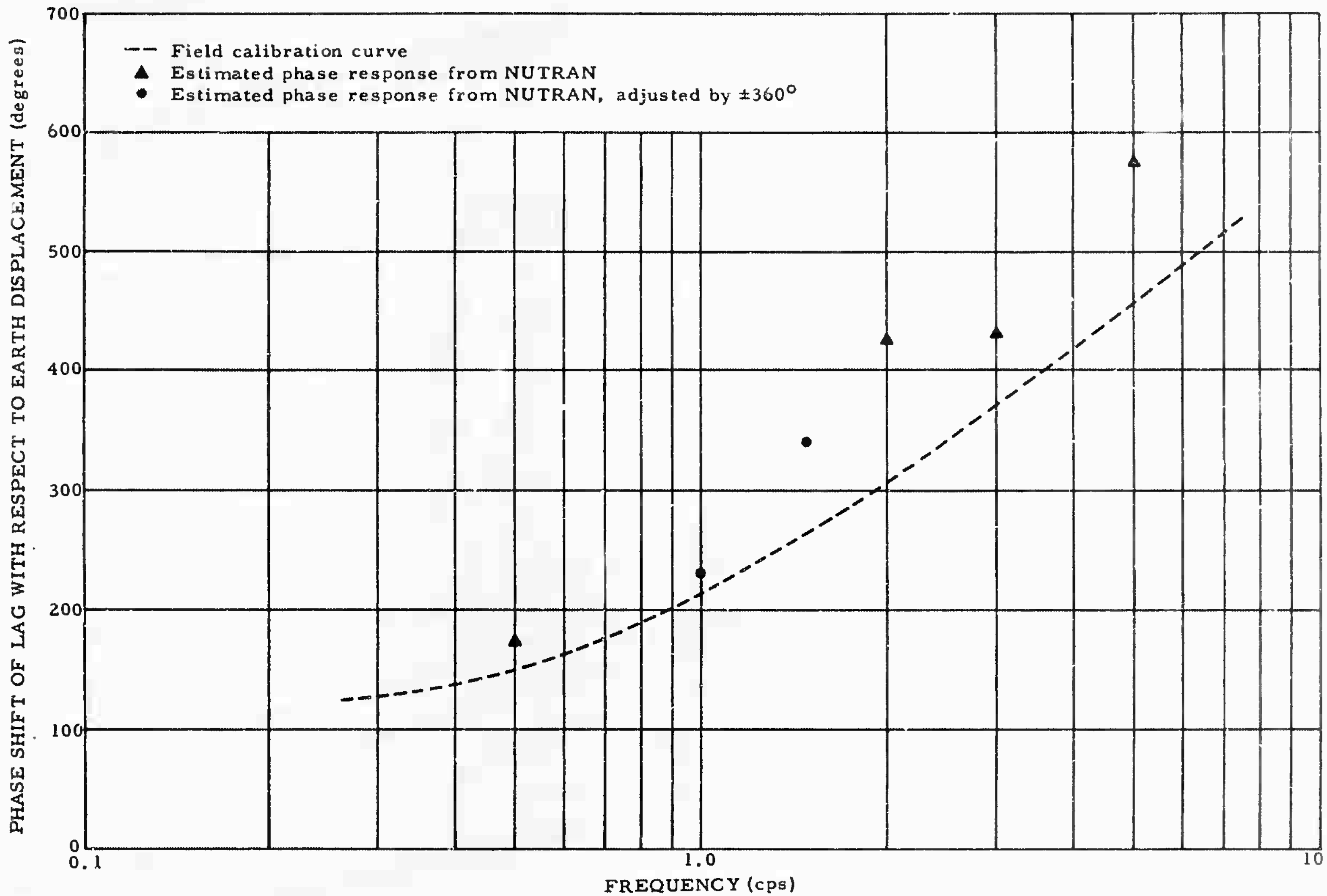

Figure 69. Phase calibration estimates at WO-AZ Z_2, 2 second case

G 408

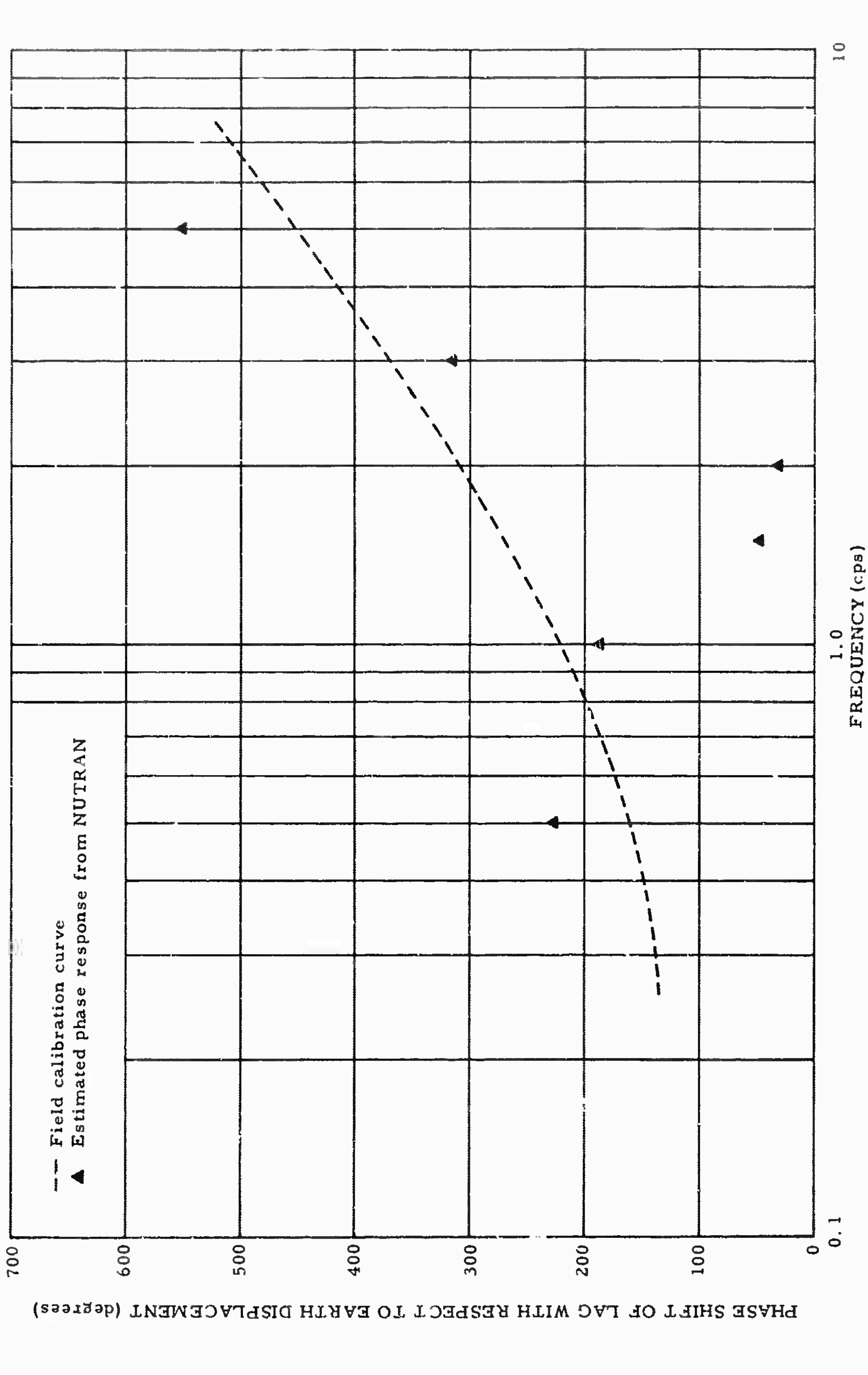

Figure 70. Phase calibration estimates at WO-AZ Z_3, 2 second case

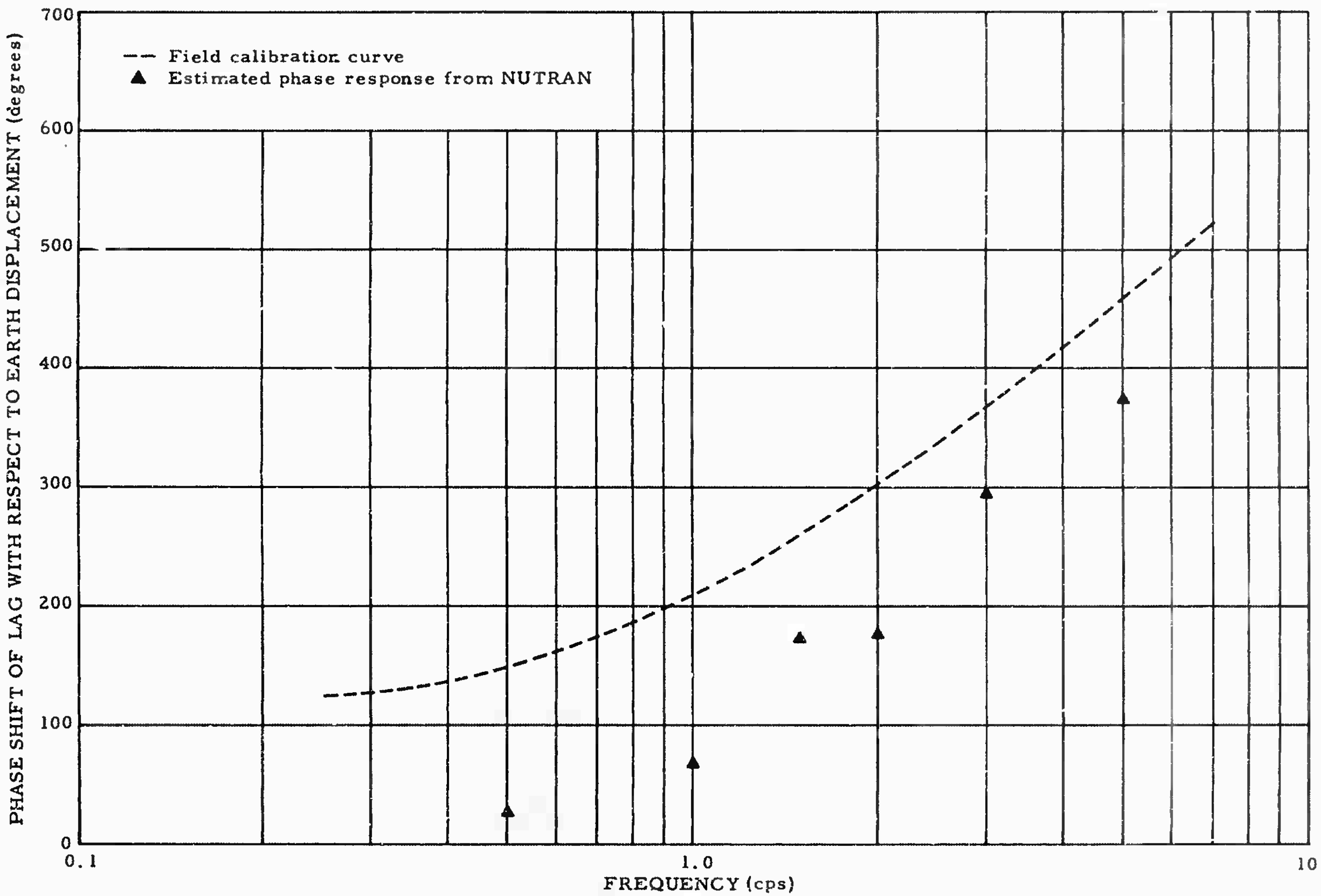

Figure 71. Phase calibration estimates at WO-AZ Z_4, 2 second case

G 410

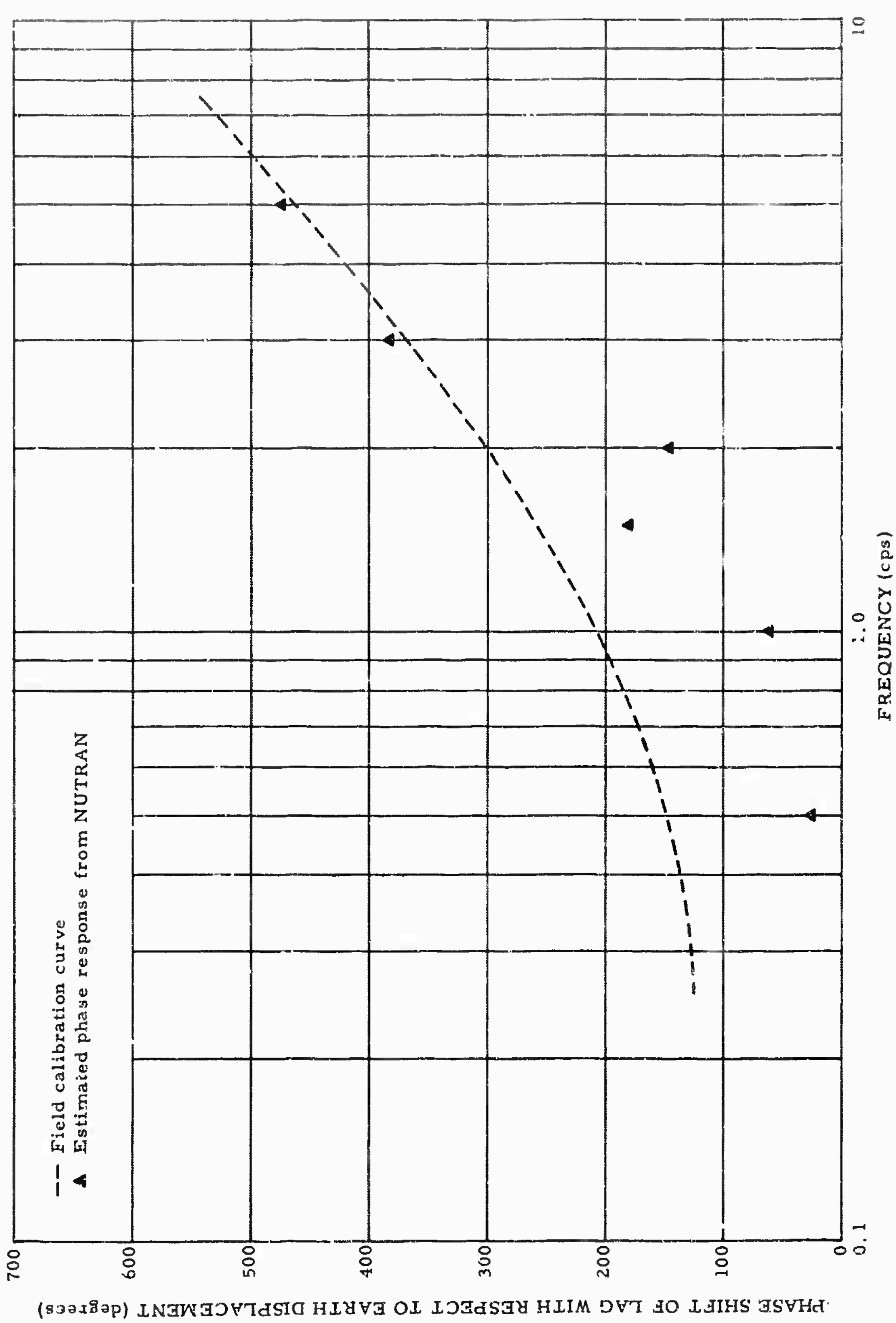

G 411

Figure 72. Phase calibration estimates at WO-AZ Z_5, 2 second case

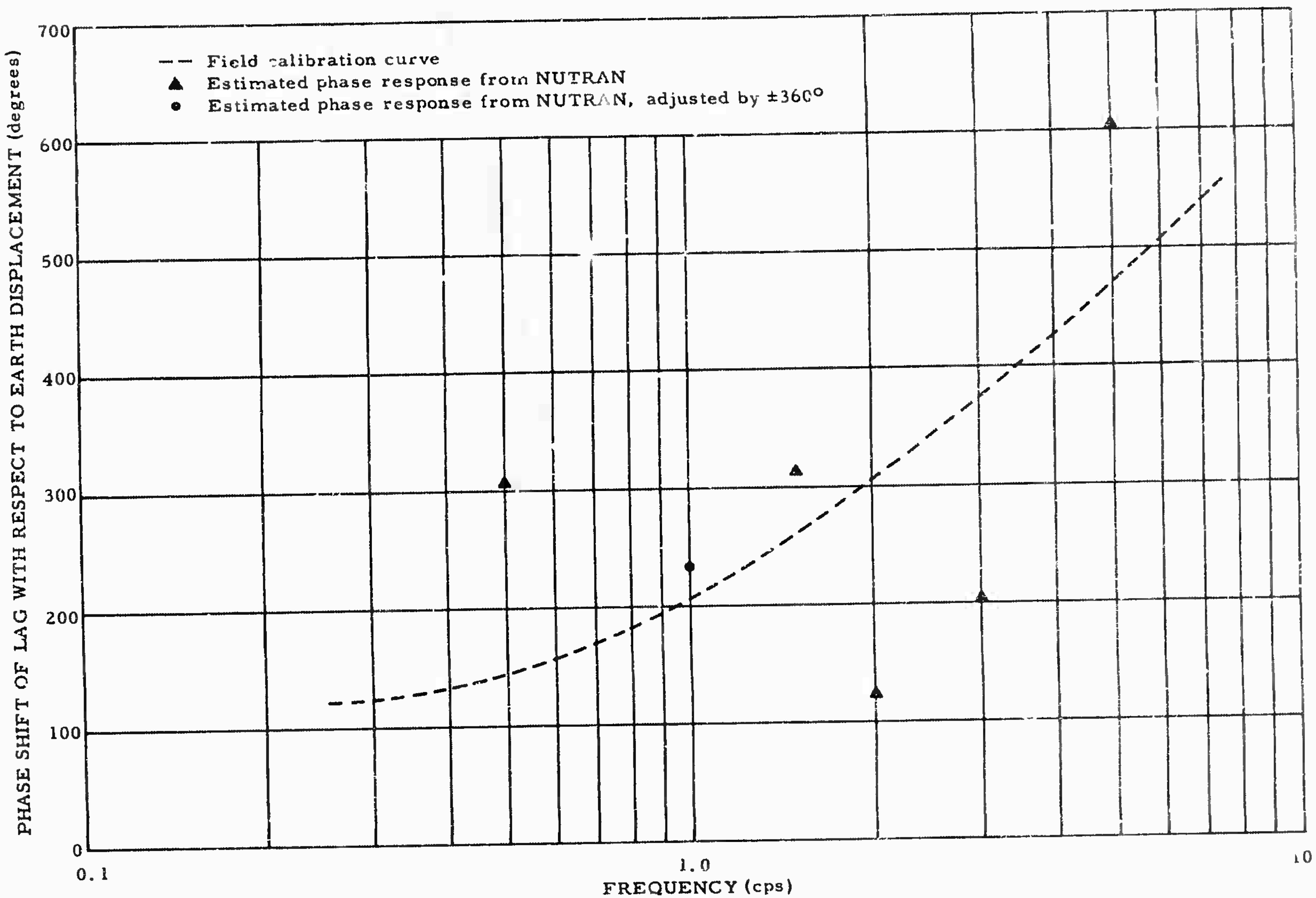

Figure 73. Phase calibration estimates at WO-AZ Z_6, 2 second case

G 412

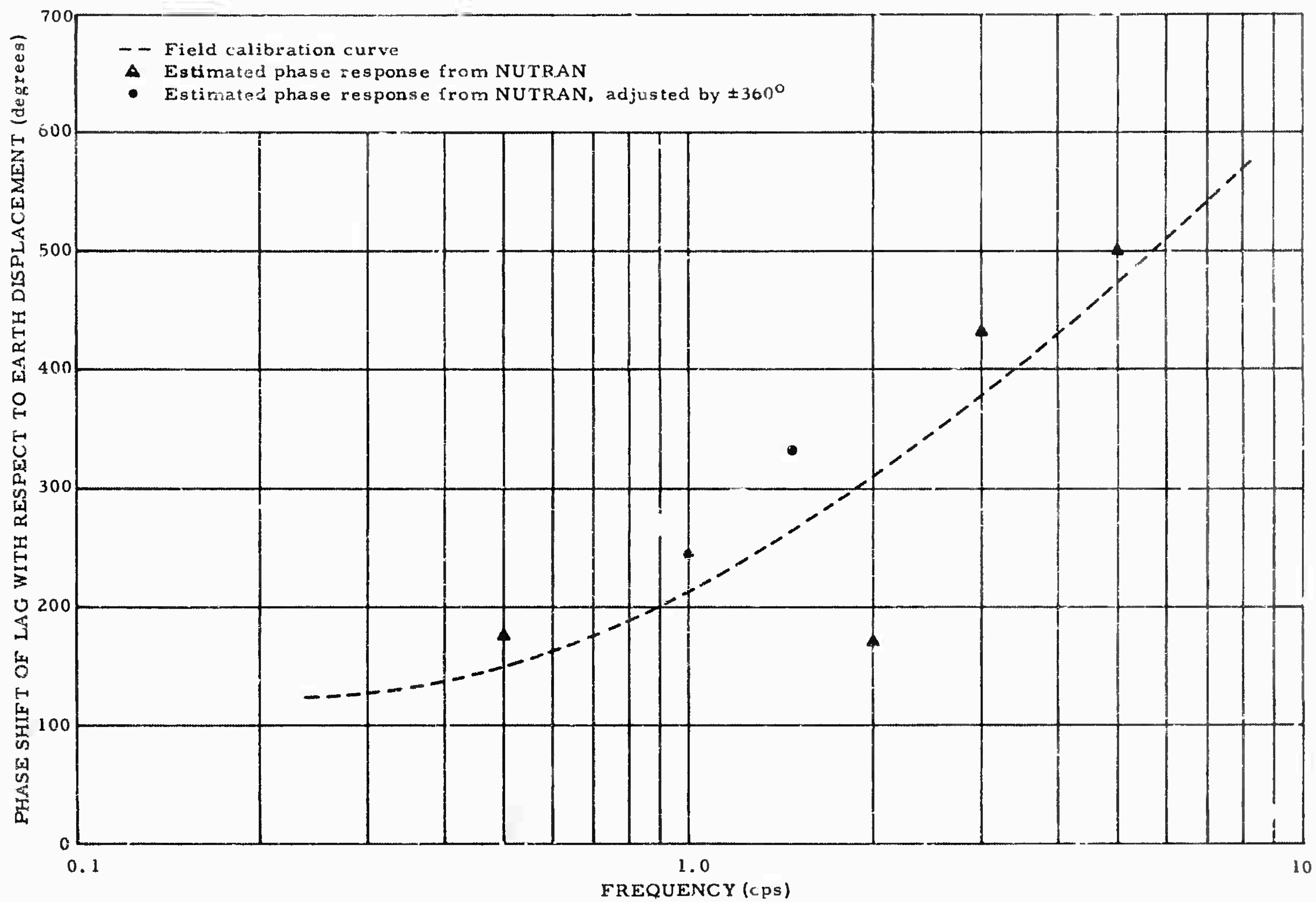

Figure 74. Phase calibration estimates at WO-AZ Z_7, 2 second case

G 413

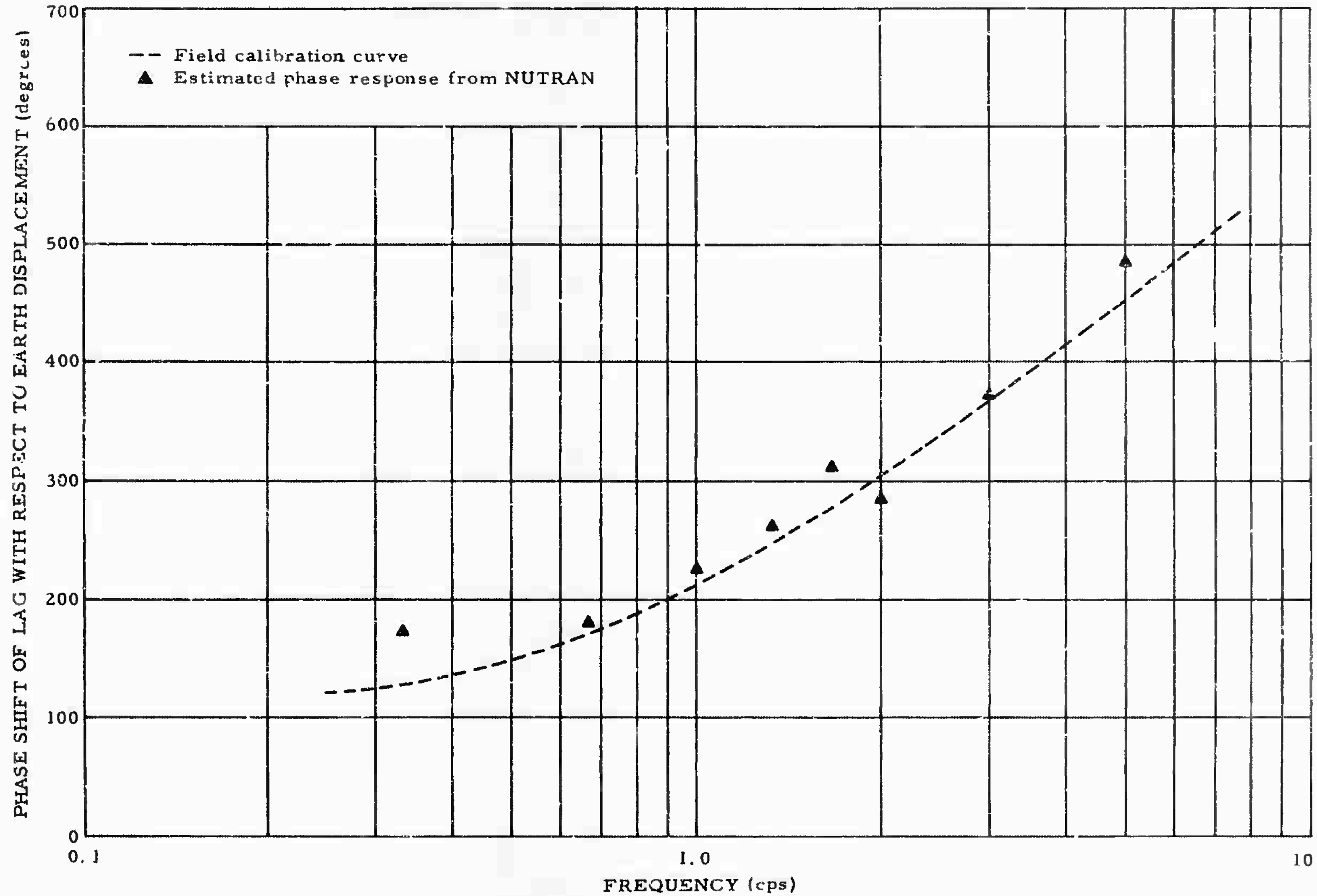

Figure 75. Phase calibration estimates at WO-AZ Z_2, 3 second case

G 414

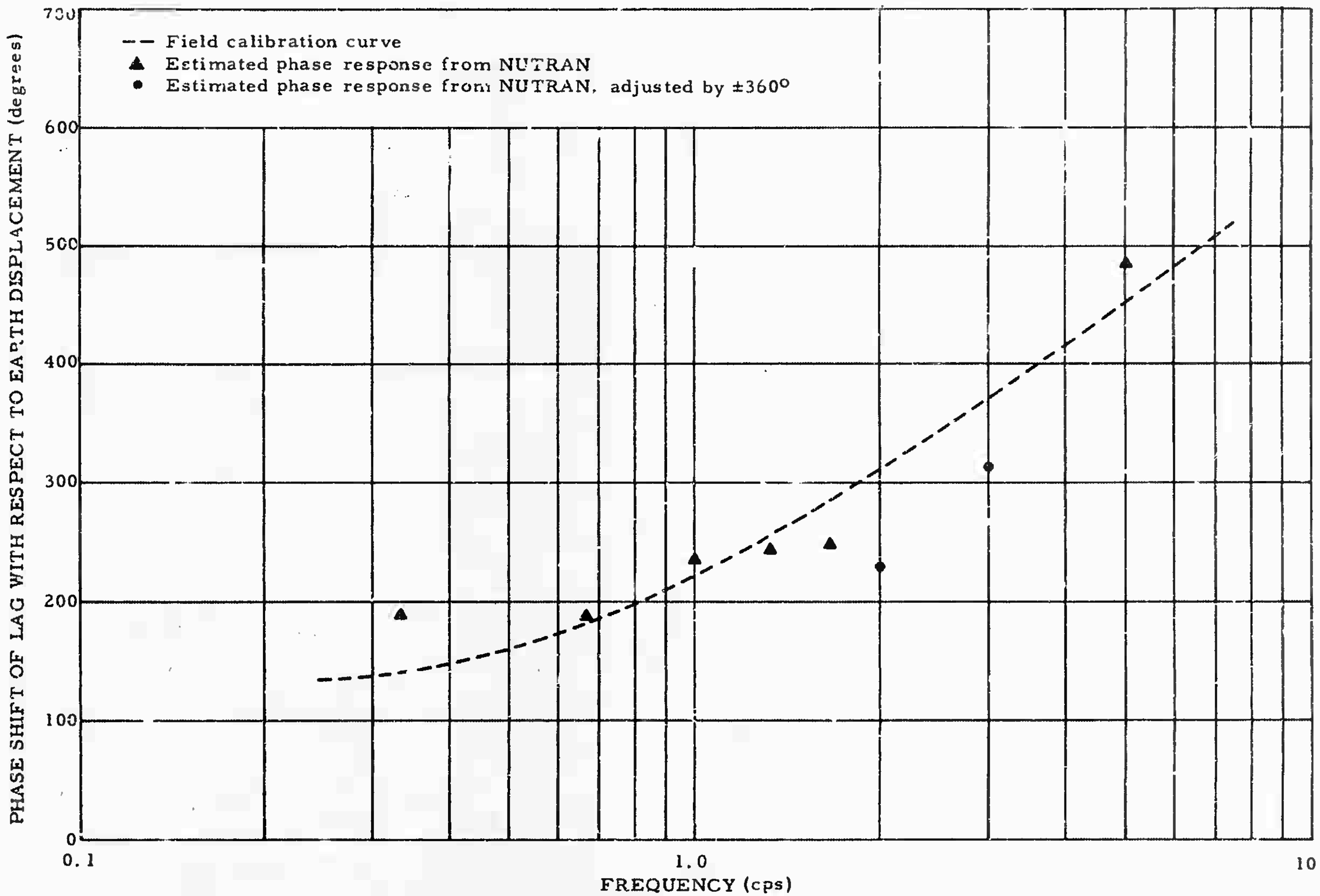

Figure 76. Phase calibration estimates at WO-AZ Z_3, 3 second case

G 415

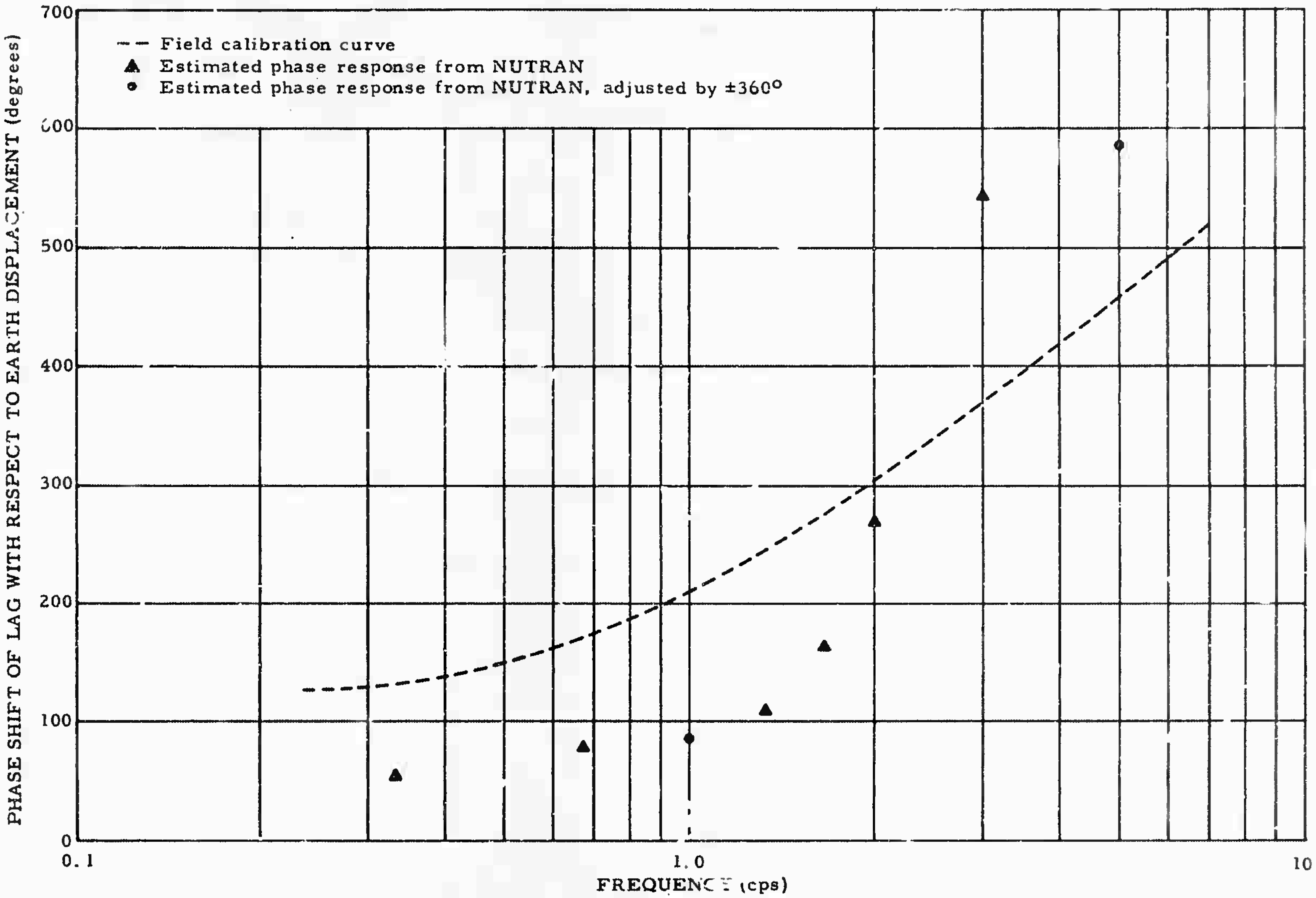

Figure 77. Phase calibration estimates at WO-AZ Z_4, 3 second case

G 416

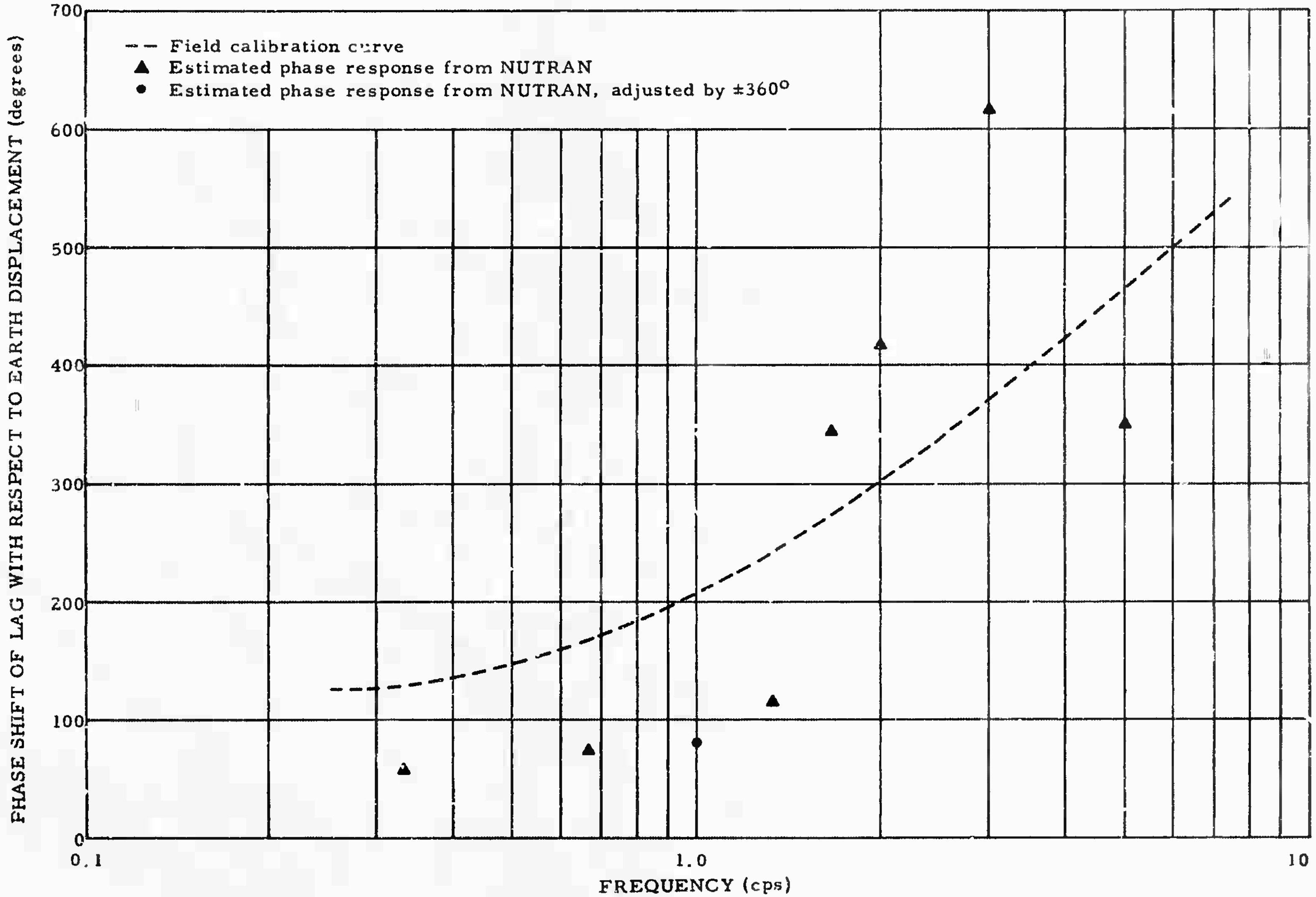

Figure 78. Phase calibration estimates at WO-AZ Z_5, 3 second case

G 417

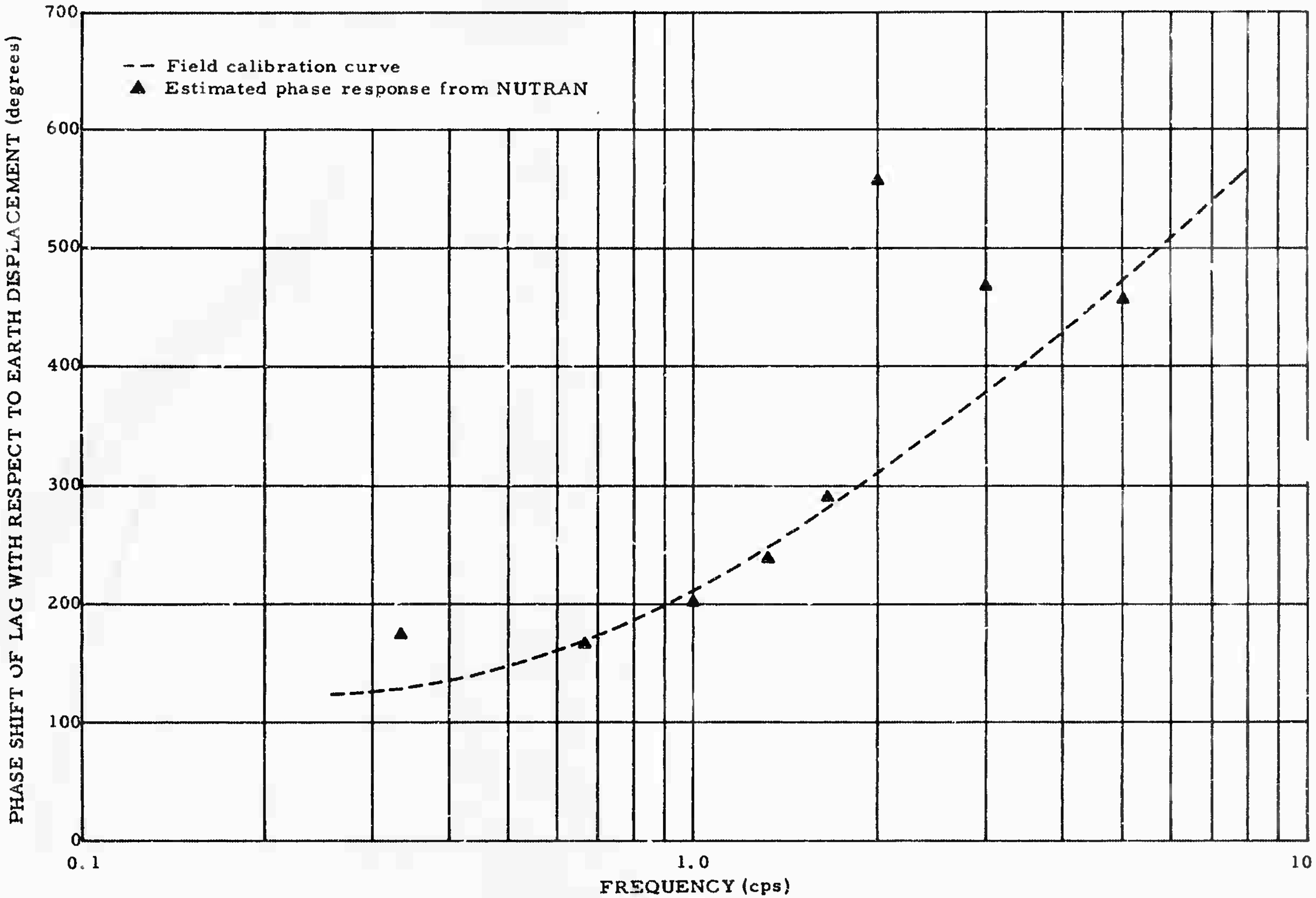

Figure 79. Phase calibration estimates at WO-AZ Z_6, 3 second case

G 418

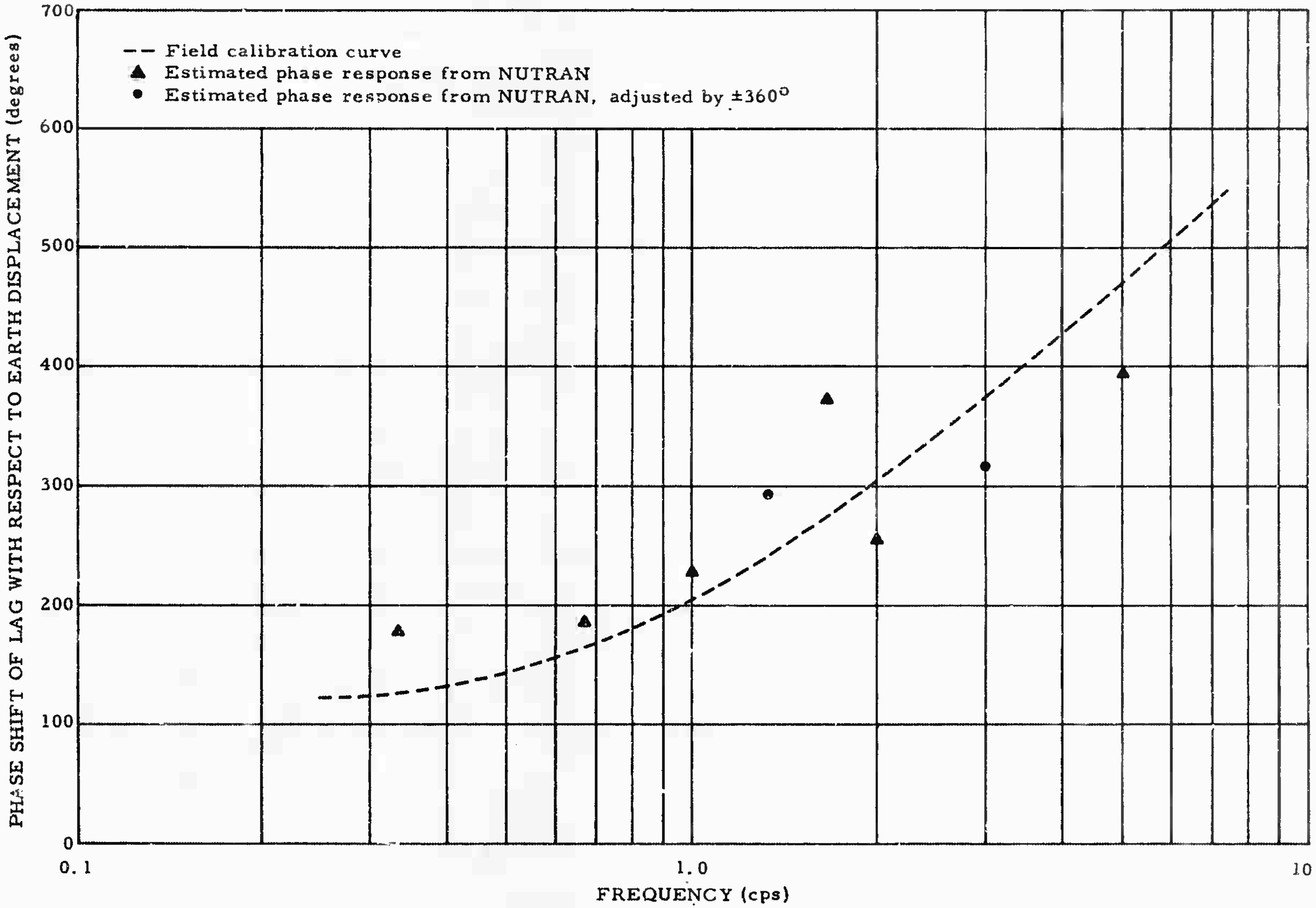

Figure 80. Phase calibration estimates at WO-AZ Z_7, 3 second case

G 419

4.2 PHASE RESPONSE

Figures 69 through 80 show the estimated phase response curves at WO-AZ using NUTRAN. The values with circles were the adjusted values (by an amount of $\pm 360^{\circ}$) to meet the multivalue requirement of the phase angle. The results are rather irregular and inconclusive. The corresponding curves at JR-AZ are not available due to lack of phase-calibration data for this date.

5. EFFECT OF NOISE

We wish to study the effect of noise contamination on our calibration results. Let us consider the existence of an additive noise, $n_i(t)$. The calibration model, in this case, can be represented by figure 81.

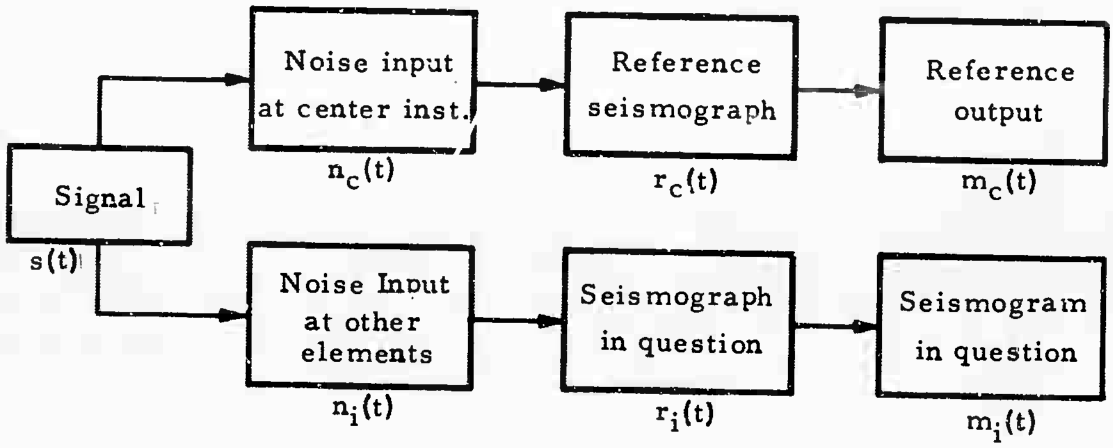

Figure 81. Noise contaminated calibration model

The inputs to the seismographs now become

$$f_c(t) = s(t) + n_c(t), \tag{13}$$

and

$$f_i(t) = s(t) + n_i(t). \tag{14}$$

Accordingly, the $m_c(t)$ and $m_i(t)$ become

$$m_c(t) = [\, s(t) + n_c(t) \,] \circledast r_c(t), \tag{15}$$

$$m_i(t) = [\, s(t) + n_i(t) \,] \circledast r_i(t), \tag{16}$$

where $r_c(t)$ and $r_i(t)$ are the seismograph impulse responses, and $\circledast$ denotes convolution.

In the spectral domain, we have respectively

$$M_c(\omega) = [\, S(\omega) + N_c(\omega) \,]\; R_c(\omega), \tag{17}$$

and

$$M_i(\omega) = [\, S(\omega) + N_i(\omega) \,]\, R_i(\omega). \tag{18}$$

Replacing $R_c(\omega)$ and $R_i(\omega)$ by

$$R_c(\omega) = A_c(\omega) e^{jB_c(\omega)}, \tag{19}$$

and

$$R_i(\omega) = A_i(\omega) e^{jB_i(\omega)}, \tag{20}$$

we will have expressions for $A_i(\omega)$ and $B_i(\omega)$ which correspond to the amplitude and phase response curves of the seismograph in question.

In terms of the modulus and phase, $M_c(\omega)$, $M_i(\omega)$, $N_c(\omega)$, and $N_i(\omega)$ can be rewritten by

$$\begin{aligned} M_c &= \rho_{mc} e^{j\theta_{mc}}, \qquad & M_i &= \rho_{mi} e^{j\theta_{mi}}, \\ N_c &= \rho_{nc} e^{j\theta_{nc}}, \qquad & N_i &= \rho_{ni} e^{j\theta_{ni}}. \end{aligned} \tag{21}$$

For the purpose of simplicity, the expressions (ω) are abbreviated. The $A_i(\omega)$ and $B_i(\omega)$ then become

$$A_i(\omega) = \frac{\rho_{mi}(\omega)A_c(\omega)}{\Delta(\omega)}, \tag{22}$$

and (23)

$$B_i(\omega)=B_c(\omega)+\theta_{mi}(\omega)-\tan^{-1}\left[\frac{\rho_{mc}\sin\theta_{mc}+\rho_{ni}A_c\sin(\theta_{ni}+B_c)-\rho_{nc}A_c\sin(\theta_{nc}+B_c)}{\rho_{mc}\cos\theta_{mc}+\rho_{ni}A_c\cos(\theta_{ni}+B_c)-\rho_{nc}A_c\cos(\theta_{nc}+B_c)}\right],$$

where

$$\Delta^2(\omega) = \rho^2_{mc} + \rho^2_{ni}A^2_c + \rho^2_{nc}A^2_c - 2\rho_{ni}\rho_{nc}A^2_c\cos(\theta_{ni} - \theta_{nc})$$

$$+ 2\rho_{mc}\rho_{ni}A_c\cos(\theta_{mc} - \theta_{ni} - B_c) - 2\rho_{mc}\rho_{nc}A_c\cos(\theta_{mc}-\theta_{nc}-B_c). \tag{24}$$

When

$N_c = N_i = \rho_n e^{j\theta_n}$, equation (24) yields

$$\Delta(\omega)\Big]_{N_c = N_i} = \rho_{mc}(\omega). \tag{25}$$

Equations (22) and (23) then become, respectively

$$A_i(\omega) = A_c(\omega) \cdot \frac{\rho_{mi(\omega)}}{\rho_{mc(\omega)}} , \tag{26}$$

and

$$B_i(\omega) = B_c(\omega) + \theta_{mi}(\omega) - \theta_{mc}(\omega), \tag{27}$$

which are the same expressions as equations (1) and (2).

The magnification curves are affected by $\Delta(\omega)$ of equation (24). Depending upon the sign of the quantity

$$E^2 = (\rho^2_{ni} + \rho^2_{nc})A^2_c + 2\rho_{mc}\rho_{ni}A_c\cos(\theta_{mc} - \theta_{ni} - B_c)$$

$$-2\rho_{nc}A_c[\rho_{ni}A_c\cos(\theta_{ni} - \theta_{nc}) + \rho_{mc}\cos(\theta_{mc} - \theta_{nc} - B_c], \tag{28}$$

the amplitude response can deviate from the normal response curve either upward or downward. For $E^2>0$, the estimated response will be smaller than the normal, whereas for $E^2<0$, the estimated response will become greater than the normal.

The condition for perfect match b[illegible]en the estimated and the field calibration results under the above modifications is

$$(\rho^2_{ni} + \rho^2_{nc})A_c + 2\rho_{mc}\rho_{ni}\cos(\theta_{mc} - \theta_{ni} - B_c)$$

$$= 2\rho_{nc}[\rho_{ni}A_c\cos(\theta_{ni} - \theta_{nc}) + \rho_{mc}\cos(\theta_{mc} - \theta_{nc} - B_c)]. \tag{29}$$

When the additive noise is absent, the relationship of equation (29) will be automatically satisfied. As we notice from equation (28), the expression for E^2 depends not only on the amplitude information of the received signal and the noise, but also requires the phase information. This situation is further complicated by other types of existing noise, for example, source-generated noise or noise due to local geology. In the next section, we shall examine the signal-to-noise ratio.

6. SIGNAL-TO-NOISE RATIO

By transforming equations (13) and (14) to the frequency domain, we may define a signal-to-noise ratio as a function of frequency. This expression is given by

$$\frac{S(\omega)}{N(\omega)} = \frac{F(\omega)}{N(\omega)} - 1, \tag{30}$$

where $F(\omega)$ is the spectrum of the noise-contaminated signal.

In figure 82, we have shown two examples of the signal-to-noise amplitude-ratio distribution at z_1 and z_6 of the JR-AZ subarray. Two-second noise samples immediately preceeding the 2-second signal event were analyzed. Interestingly enough, we observe

a. Irregular distribution of the signal-to-noise ratio with respect to different frequencies;

b. High signal-to-noise ratio (of more than 4) centers below 1.5 cps.

The good agreement between the estimated magnification curves and the field calibrations at frequencies below 1.5 cps may be interpreted from the point of view of the high signal-to-noise ratio in this range.

Figures 83 and 84 show the spectral distribution of noise amplitudes. The rather irregular distribution of this noise is a significant factor affecting our results. Two-second record lengths were taken for analysis.

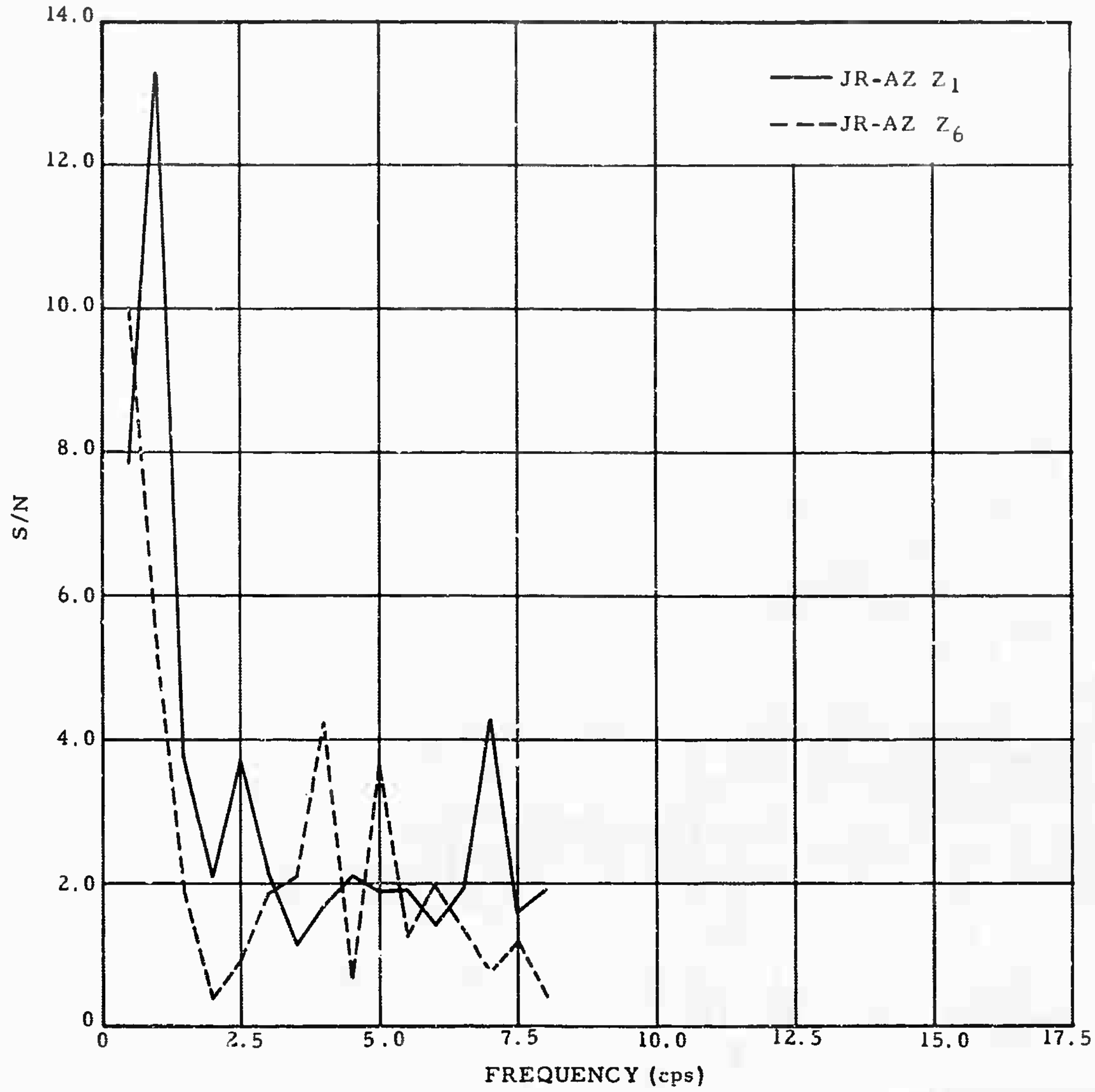

Figure 82. Distribution of signal-to-noise ratio when noise is assumed additive

G 420

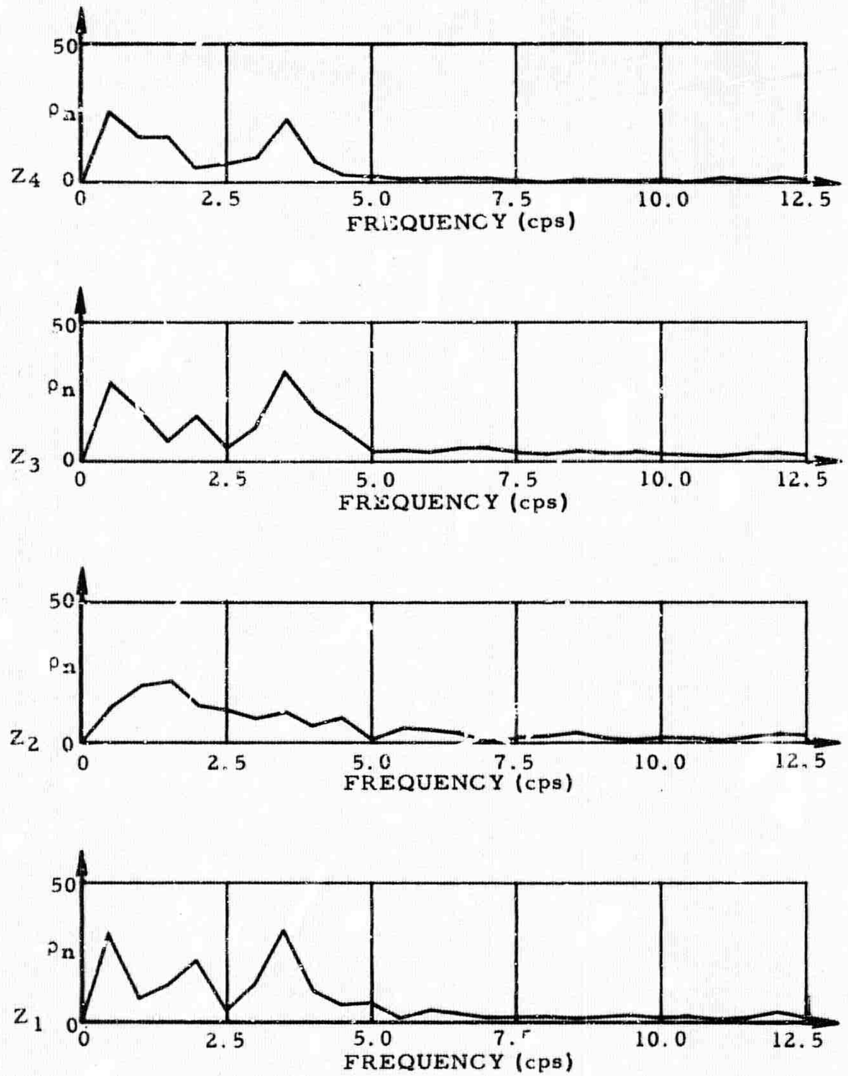

Figure 83a. JR-AZ Z_1 - Z_4, 2-second noise samples, Fourier amplitudes 2 June 1965 (no dc bias)

G 421

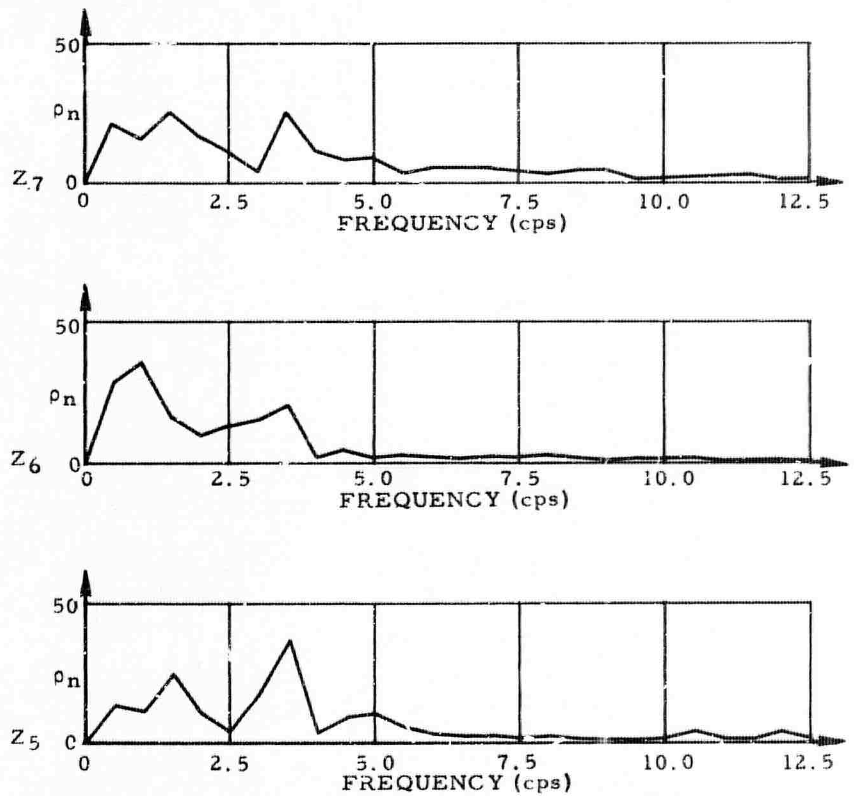

Figure 83b. JR-AZ Z_5 - Z_7, 2-second noise samples, Fourier amplitudes 2 June 1965 (no dc bias)

G 422

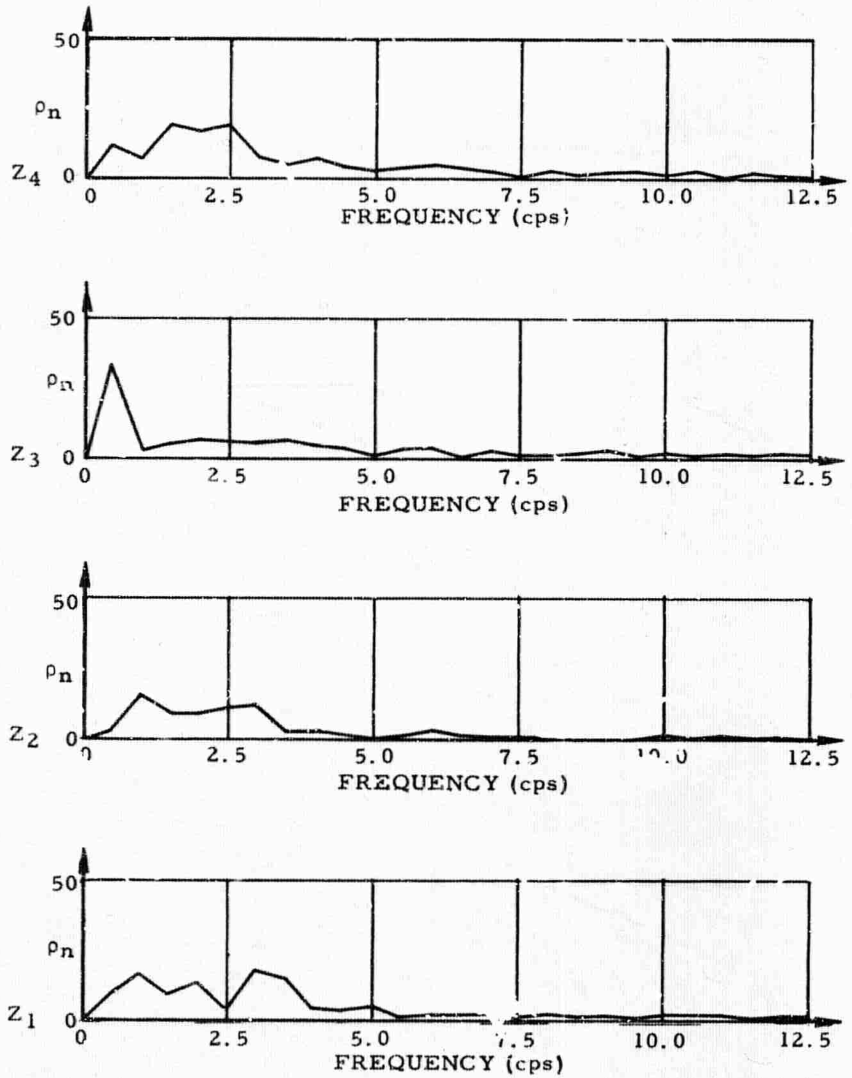

Figure 84a. WO-AZ Z_1 - Z_4, 2-second noise samples, Fourier amplitudes 2 June 1965 (no dc bias)

G 423

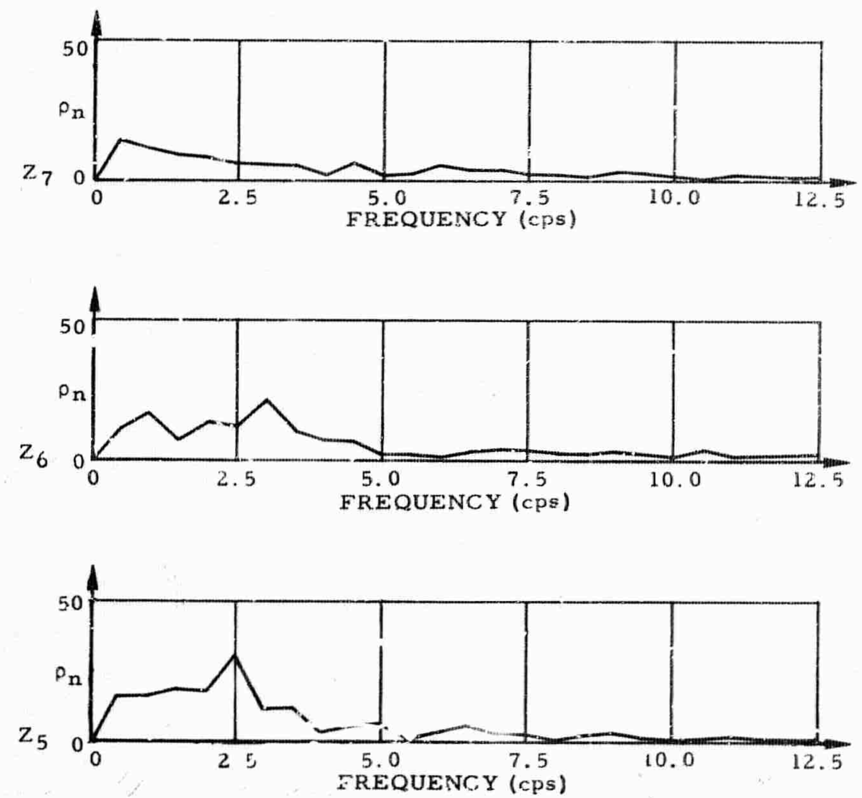

Figure 84b. WO-AZ Z_5 - Z_7, 2-second noise samples, Fourier amplitudes 2 June 1965 (no dc bias)

G 424

The power density spectra of noise at JR-AZ and WO-AZ are given in figures 85 and 86. A record length of 130 seconds, with a maximum lag of 10 seconds, was used in the analysis.

7. CONCLUSIONS

a. From these studies we learn that the proposed multiple-element array calibration technique (Whalen, 1965) works quite well for frequencies below 1.5 cps. For frequencies above 1.5 cps, the technique fails for the following reasons:

(1) The signal content in this frequency range is insufficient to support the assumption of a high signal-to-noise ratio.

(2) Signal distortion due to local geology is more susceptible to high frequencies.

(3) The noise amplitude distribution is different for different channels (figures 83 and 84). The larger the amplitude of the noise, the less reliable will be our calibration results.

b. It is quite possible that Arizona is not the best region for studying this calibration technique, since the local geological structures seem to attenuate much of the high frequency content (Willis, 1963). Other regions, for example, Northeastern U. S. A. suggested by Willis (Willis, 1964), may give significantly better results. In addition, a shallow-hole array or the examination of phases other than P may also yield better results.

c. As previously mentioned the smoothed calibration results gave better agreement with the field calibrations. The unsmoothed digital calibration gave somewhat erratic results. Our choice of a nine-point calibration, at 0.3, 0.5, 0.7, 1.0, 1.5, 2.0, 3.0, 5.0, and 7.0 cps, made extrapolation of the computed results necessary.

d. It seems that the success of the proposed calibration technique hinges on a successful solution of the noise problems. As previously concluded, the technique works better at a geologically homogeneous location, e.g., WO-AZ than at a heterogeneous location, e. g., JR-AZ.

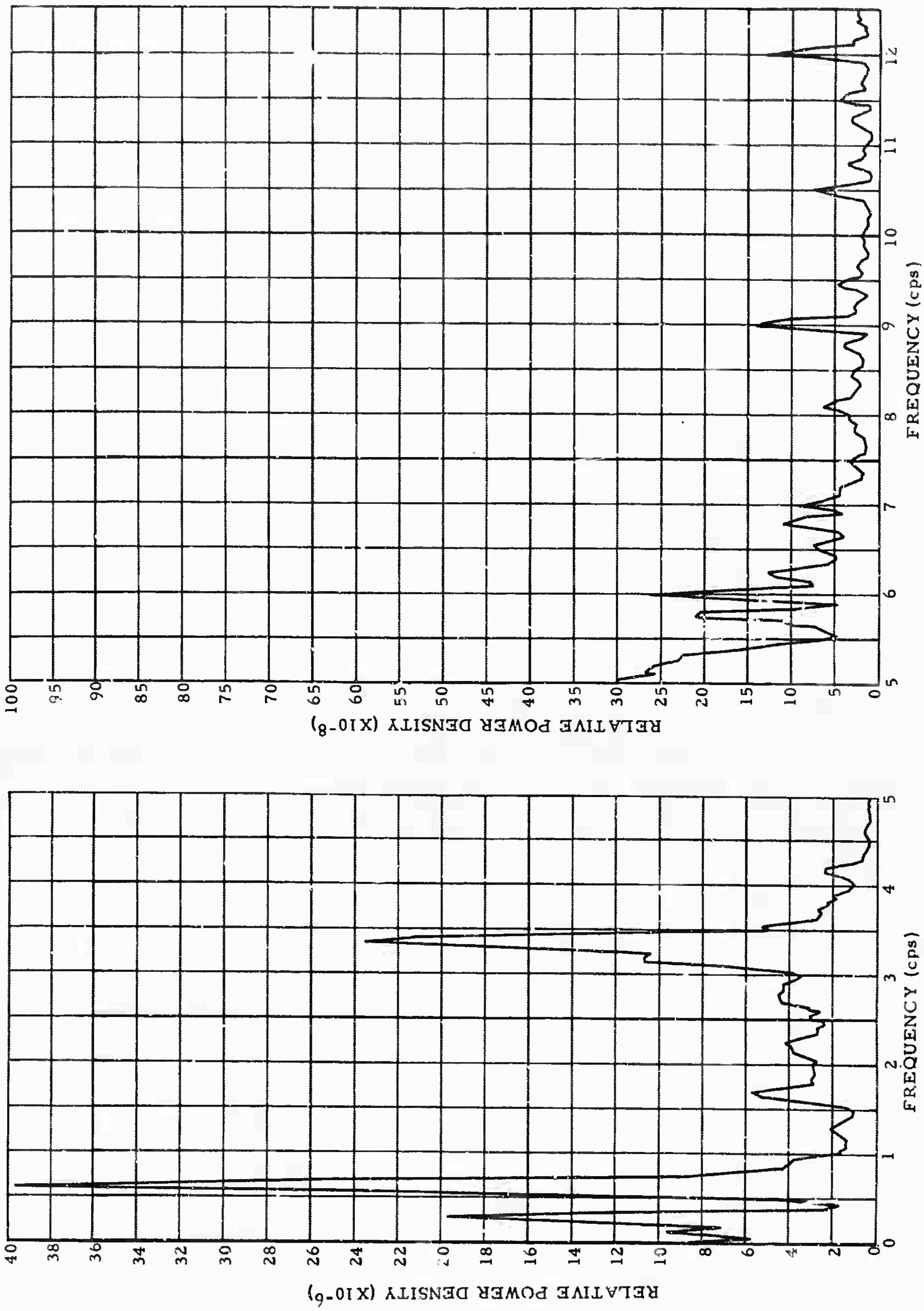

G 425

Figure 85. Power density spectrum of JR-AZ noise (Z_1)

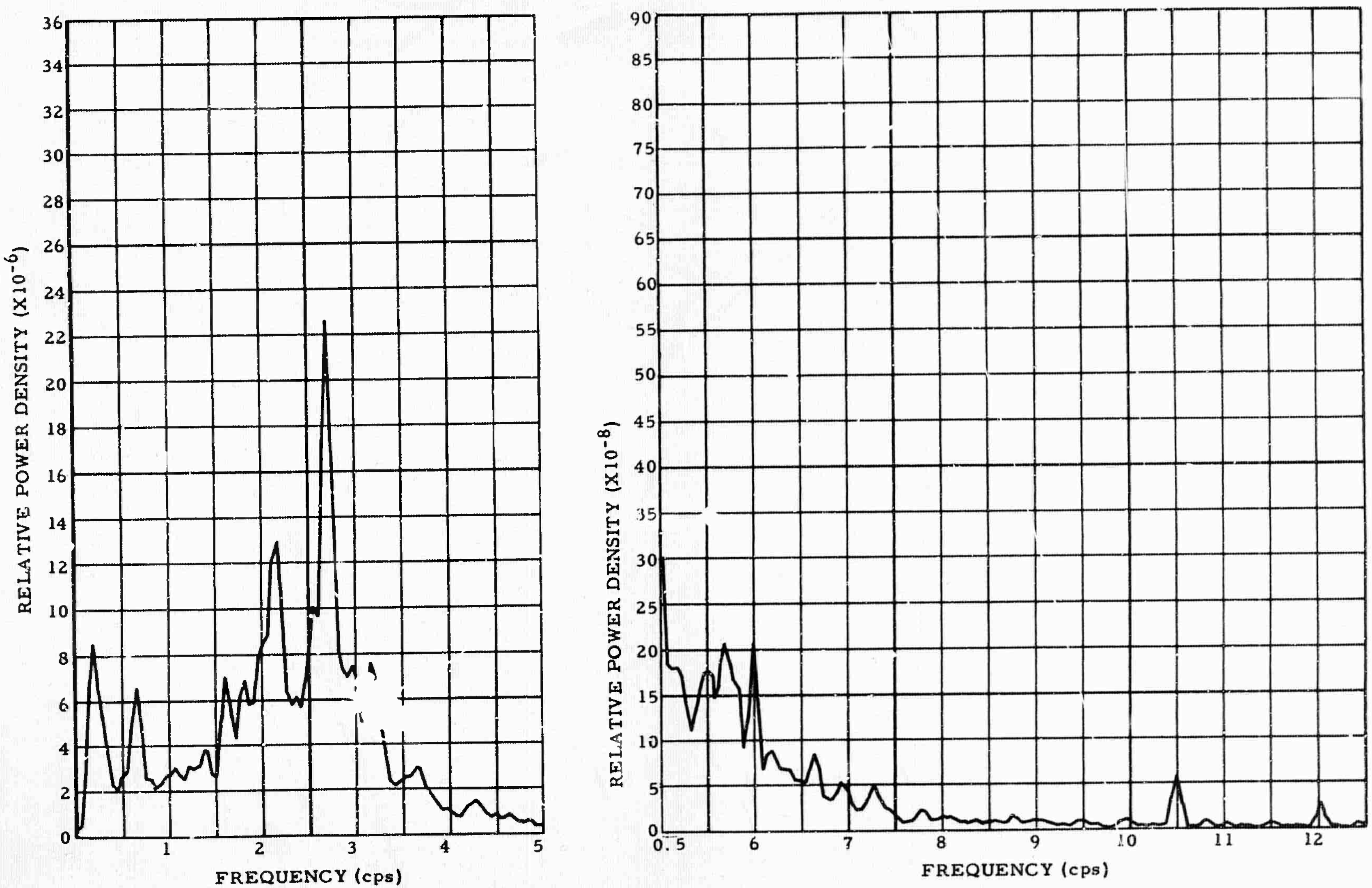

Figure 86. Power density spectrum of WO-AZ noise (Z_1)

G 426

e. Our study favors the deterministic approach over the statistical for signal analysis.

f. The following problems remain to be solved:

(1) Phase response calibration techniques;

(2) Azimuth and epicenter dependence of the station calibrations.

8. RECOMMENDATIONS

a. The same study should be conducted on long-period records. This would help to finalize our conclusions.

b. Further study should be centered on signals with wider high signal-to-noise ratio bands. This may require looking for a special phase, for example, iP, or a specific region and depth where much of the high frequencies are retained. (A recent study of 662 iP phases has shown the optimum recording distance of this phase to be between 70° - 90°.) The use of high explosives to create signals of high frequency content may also be considered.

c. A record length of about two seconds using smoothed output of the NUTRAN program, which gave better results, should be used for actual application of the technique.

d. Other time-saving approaches for multiple-element array calibration systems should be investigated.

9. ACKNOWLEDGEMENT

Paul Kozsuch, Herb Travis, Rich Simons, and Rudy Weisbrich, all of the LRSM Special Study Group, Geotech Division of Teledyne Industries, participated in this study. I am also grateful to the personnel at the JR-AZ and WO-AZ LRSM sites who contributed by recording the seismic data and the calibrations.

10. REFERENCES

Blackman, R. B. and Tukey, J. W., 1958, The measurement of power spectra: Dover Publications

Carpenter, E. W., January 1965, Explosion seismology: Science, vol. 147

Huang, Y. T., 1965a, Spectral analysis of digitized seismic data: Geotech TR 65-48

__________ 1965b, Preliminary evaluation of a calibration technique for multiple-element array systems: Geotech TR 65-111

Simons, R. S. and Whyte, W. W., 1965, Geotech analog spectrum analyzer: Geotech TR 65-68

Whalen, J. M., 29 January 1965, Letter to Captain N. A. Orsini

Willis, D. E., 1963, Comparison of seismic waves generated by different types of source: BSSA, vol. 53, no. 5, p. 965-987

__________ 1964, Short-period spectral measurements of seismic waves in the Northeastern U.S.A.: Earthquake notes, vol. 35, no. 1-2

APPENDIX 1 to TECHNICAL REPORT NO. 65-127

CALIBRATION CURVES AT SUBARRAY CENTERS

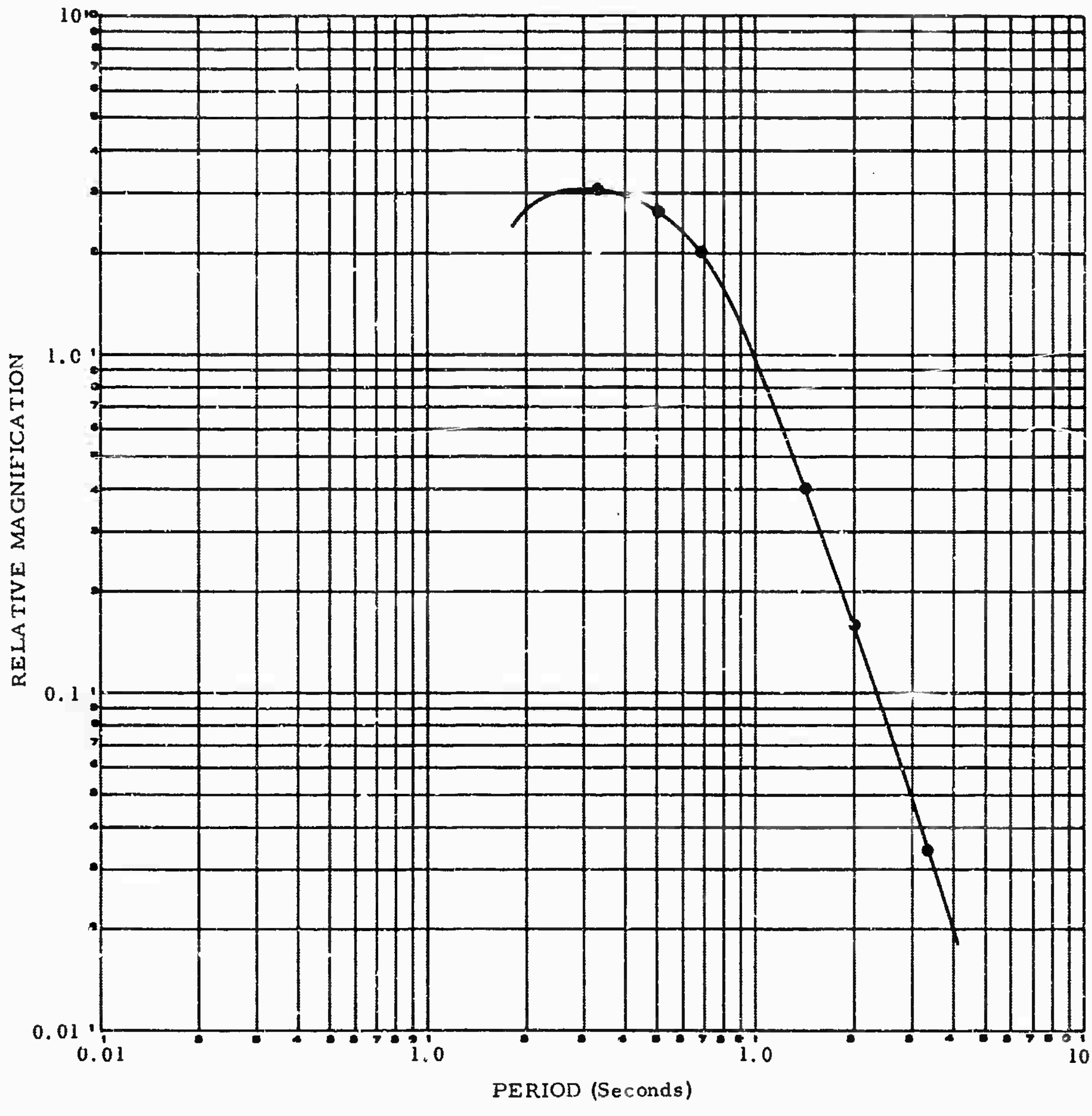

Figure 1. Station Z_1 at JR-AZ 6-2-65

G 427

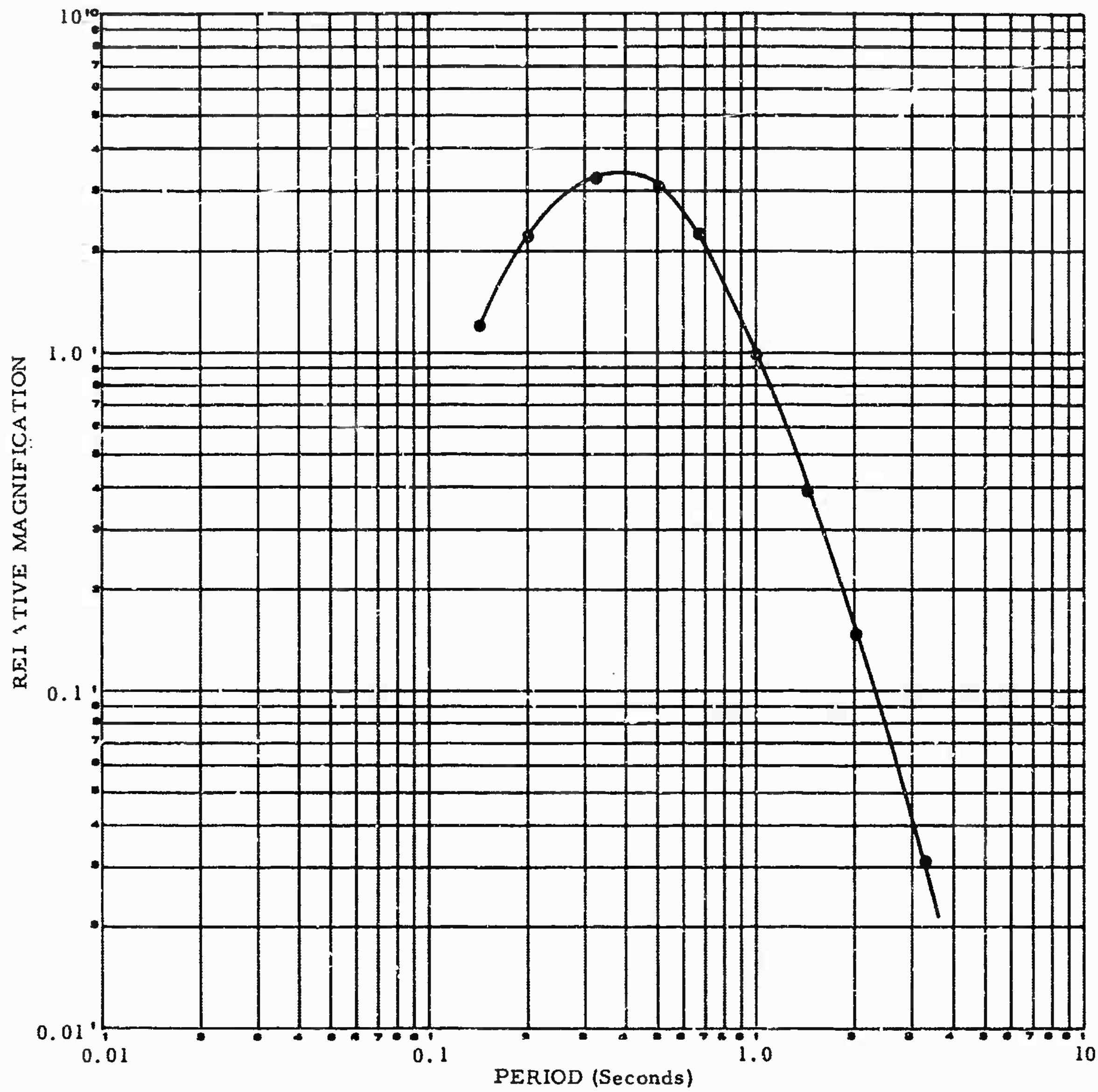

Figure 2. Station Z_1 at WO-AZ 6-2-65

G 428

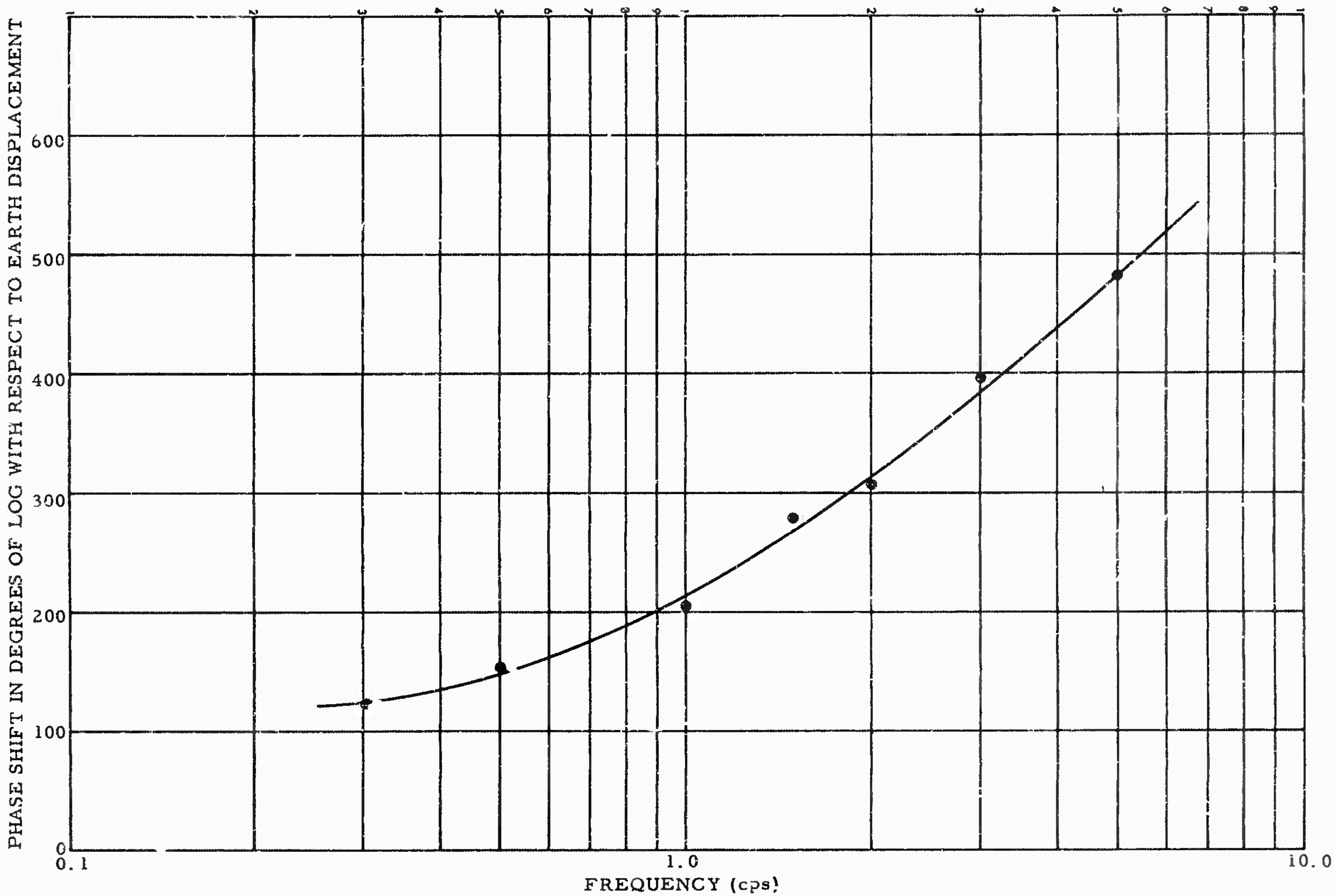

Figure 3. Seismograph Z_1 located at WO-AZ 2 June 1965

G 429

Station WO-AZ
2 June 1965 - end of May calibration

Phase shift in degrees of lag

	Seismograph						
Frequency	Z_1	Z_2	Z_3	Z_4	Z_5	Z_6	Z_7
0.3 cps	124.2	124.0	135.5	126.8	127.7	125.8	127.7
0.5 cps	154.1	149.6	164.9	153.3	148.7	148.1	148.0
0.7 cps	174.8	171.5	192.9	174.0	166.5	169.0	172.3
1.0 cps	206.7	199.6	226.4	205.9	199.9	203.7	203.7
1.5 cps	280.0	264.5	280.8	270.0	264.5	270.0	270.0
2.0 cps	309.5	297.2	307.2	304.8	302.5	307.8	309.5
3.0 cps	397.2	378.0	369.9	372.6	378.0	378.0	378.0
5.0 cps	484.0	454.5	450.0	450.0	454.5	472.5	472.5

APPENDIX 2 to TECHNICAL REPORT NO. 65-127

NUTRAN PROGRAM LISTING

```
*     NUTRAN 1
      DIMENSION ROW(126),THET(126),G(132)
    1 FORMAT(1X,A4)
    2 FORMAT(23X,A4)
    3 FORMAT(I4)
    4 FORMAT(1X,5I2,I3,2I6,3I1,I5,I4,4F3.0,3I5,I4,4I2)
    5 FORMAT(1H1)
    6 FORMAT(1X,4HSITE,1X,5HEVENT,1X,1HZ,1X,4HCASE,1X,3HNEC,1X,3HROW,
     13X,4HDATE,3X,4HTIME,1X,2HDC,1X,1HP,1X,1HQ,5X,1HM,1X,2HDR,3X,
     22HDF,2X,3HDDF,3X,2HDT,2X,3HDDT,1X,5HBEGIN,3X,3HEND,3X,3HMAX,3X,
     32HNO,1X,6HOPTION,1X,7HCONTROL,2X,3HJOB,//)
    7 FORMAT(1X,I4,2X,I4,I2,1X,I4,1X,I3,1X,I3,1X,I6,1X,I6,I3,2I2,I6,
     1I3,4F5.0,3I6,1X,I4,4X,I3,5X,I3,2X,I3,//)
    8 FORMAT(1X,10F7.0)
    9 FORMAT(21X,4HG(I),22X,1HI,//)
   10 FORMAT(18X,F7.0,16X,I7)
   11 FORMAT(6X,I6,2X,I6,3X,I1,3X,I1)
   12 FORMAT(I5)
   13 FORMAT(24F5.0)
   14 FORMAT(10X,4HA(N),8X,4HB(N),9X,3HMOD,7X,5HPHASE,8X,
     118HACCUMULUTIVE PHASE,8X,8HROTATION,8X,9HFREQUENCY,8X,1HN,//)
   15 FORMAT(4X,F10.4,2X,F10.4,2X,F10.4,2X,F10.4,16X,F10.4,6X,F10.4,
     17X,F10.4,1X,I8,/)
   16 FORMAT(2X,I2,2X,I6,2X,I6,3X,I4,2X,I4,2X,I3,2X,I4,2X,I2,2X,I2,
     12X,I2,2X,I2,2X,I2)
   17 FORMAT(12F10.4)
   18 FORMAT(3X,5HTREND)
   19 PAUSE 1111
      READ 1,NO
B     IF(NO/20202020)26,29,26
   26 READ INPUT TAPE 3,2,NNO
   27 IF(NO-NNO)26,28,26
   28 READ INPUT TAPE 3,3,IDUMB
      IF(XEOF(3))29,28,29
   29 READ 4,NS,IEV,INST,ICASE,INEC,NM,ID,IT,IK,IP,IQ,M,MR,DF,DDF,DT,
     1DDT,IN,IM,MAX,NO,IOP,IL,JOB,IEC
      IF(M)55,55,30
   30 PRINT 5
      PRINT 6
      PRINT 7,NS,IEV,INST,ICASE,INEC,NM,ID,IT,IK,IP,IQ,M,MR,DF,DDF,DT,
     1DDT,IN,IM,MAX,NO,IOP,IL,JOB
      DF=DF/DDF
      DT=DT/DDT
      PI=3.14159265
      PPI=2.0*PI
      ACCUM=0.0
      AM=M
   31 IF( IL)32,60,60
   32 IF(JOB)33,34,40
   33 READ 8,(G(I),I=1,MAX)
      PRINT 9
      IF(IOP)200,300,500
  300 PRINT 10,(G(I),I,I=IN,IM)
      GO TO 41
```

```
 34 READ INPUT TAPE 2,11,JD,JT,JNST,JEC
    IF(ID-JD)34,35,34
 35 IF(IT-JT)34,36,34
 36 IF(INST-JNST)34,37,34
 37 IF(IEC-JEC)34,38,34
 38 PRINT 11,JD,JT,JNST,JEC
    DO 39 I=1,NM
    READ INPUT TAPE 2,12,KDUMB
 39 CONTINUE
    READ INPUT TAPE 2,13,(G(I),I=1,MAX)
    PRINT 9
    IF(IOP)200,600,500
600 PRINT 10,(G(I),I,I=IN,IM)
    GO TO 41
200 GK=0.0
    DO 201 K=IN,IM
    GK=GK+G(K)
201 CONTINUE
    KDIFF=(IM-IN)+1
    ADIFF=KDIFF
    GK=GK/ADIFF
    DO 202 K=IN,IM
    G(K)=G(K)-GK
202 CONTINUE
    IF(JOB)300,600,40
500 PRINT 18
 60 PRINT 9
 61 PRINT 10,(G(I),I,I=IN,IM)
 40 CONTINUE
 41 RM=2.0/AM
    DEC=1.0/2.0
    BPRIME 1.0/(DF*DT)
    P=IP
    Q=IQ
    AP=BPRIME*P
    NPRIME=AP
    PRINT 5
    PRINT 14
    DO 52 N=1,NPRIME
    K=N-1
    AN=0.0
    BN=0.0
    CK=K
    FREQ=CK*DF
    ARGN=(2.0*PI*CK)/BPRIME
    DO 42 I=IN,IM
    II=(I-IN)+1
    AI=II
    ARG=ARGN*AI
    TRIG=COSF(ARG)
    TRAG=SINF(ARG)
    AN=AN+G(I)*TRIG
    BN=BN+G(I)*TRAG
 42 CONTINUE
```

```
      AN=AN*RM
      BN=BN*RM
      ROW(N)=SQRTF(AN*AN+BN*BN)
      IF(AN)43,47,43
   43 THET(N)=ATANF(BN/AN)
      IF(AN)44,47,51
   44 IF(BN)45,45,46
   45 THET(N)=THET(N)-PI
      GO TO 51
   46 THET(N)=THET(N)+PI
      GO TO 51
   47 IF(BN)48,49,50
   48 THET(N)=-PI/2.0
      GO TO 51
   49 THET(N)=0.0
      GO TO 51
   50 THET(N)=PI/2.0
   51 IF(N-1)114,114,117
  114 IF(THET(N))115,116,116
  115 THETL=PPI+THET(N)
      GO TO 106
  116 THETL=THET(N)
      GO TO 106
  117 IF(THETM)101,110,112
  101 IF(THET(N))105,105,109
  102 THETL=THET(N)
      GO TO 106
  105 IF(THETM-THET(N))108,107,104
  104 THETL=PPI-ABSF(THETM-THET(N))
  106 ACCUM=ACCUM+THETL
      ROTA=ACCUM/PPI
      GO TO 63
  107 THETL=0.0
      GO TO 106
  108 THETL=ABSF(THETM-THET(N))
      GO TO 106
  109 THETL=ABSF(THETM)+THET(N)
      GO TO 106
  110 IF(THET(N))111,102,102
  111 THETL=THET(N)+PPI
      GO TO 106
  112 IF(THET(N))113,113,105
  113 THETL=PPI-(ABSF(THET(N))+THETM)
      GO TO 106
   63 PRINT 15,AN,BN,ROW(N),THET(N),ACCUM,ROTA,FREQ,K
      THETM=THET(N)
   52 CONTINUE
      IF(JOB)54,53,54
   53 WRITE OUTPUT TAPE 3,16,NS,ID,IT,NO,M,MR,NPRIME,IEV,INST,INEC,IK,
     1ICASE
      WRITE OUTPUT TAPE 3,17,(ROW(N),THET(N),N=1,NPRIME)
      END FILE 3
      REWIND 2
   54 IF(IL)29,29,55
```

```
55 IF(JOB)58,56,58
56 REWIND 2
57 REWIND 3
58 CONTINUE
   GO TO 19
   END
```

```
*     PROGRAM NUTRAN II
      DIMENSION TABLX(4),TABLY(4),DEL(4),RHO1(10),RHO2(075),RHO3(075),
     1THETA1(10),THETA2(075),THETA3(075),PERIOD(10)
   10 FORMAT(A4)
   11 FORMAT (I3)
   15 FORMAT(3F10.4)
   17 FORMAT (23X,A4)
   18 FORMAT (50X,I2,10X,I2)
   20 FORMAT (12F10.4)
   25 FORMAT (2X,I2,2X,A6,2X,A6,9X,I4,2X,F3.0,2X,I4,6X,I2,10X,I2)
   30 FORMAT(1H1,///,40X,22HLASA CALIBRATION STUDY////)
   31 FORMAT (07X,15HUNSMOOTHED DATA)
   32 FORMAT (07X,13HSMOOTHED DATA)
   35 FORMAT (07X,13HCORRECTED AND)
   37 FORMAT(7X,1HT,7X,2HRL,7X,1HX,7X,2HR1,7X,2HR2,7X,2HR3,7X,10H(R1*R3)
     1/R2, 7X,2HA1,7X,2HA2,7X,2HA3,7X,10H(A1+A3-A2))
   38 FORMAT (30X,41HCOMPARISON OF AMPLITUDE AND PHASE SPECTRA/
     .37X,18HFOR INSTRUMENTS Z ,I2,7H AND Z ,I2/
     242X,14HFOR CASE STUDY,I3/
     344X,10HAT STATION,I3////)
   40 FORMAT(25X,I4,6X,F10.3,4X,F10.3,4X,F10.3,4X,F10.3)
   41 FORMAT(5X,F5.2,3X,F5.2,1X,F7.2,2X,F6.2,2X,F8.2,1X,F8.2,6X,F8.3,
     13X,F10.3,2F9.3,4X,F10.3)
 6666 PAUSE 6666
      REWIND 2
C     READ INSTRUMENT CORRECTION FACTORS
  100 READ 11,LEGT
      READ 15,(PERIOD(I),RHO1(I),THETA1(I),I=1,LEGT)
      READ 10,NEVENT
  120 READ INPUT TAPE 2,17,IEVENT
      IF(NEVENT-IEVENT)120,125,120
  125 BACKSPACE 2
      JCASE=0
  130 READ INPUT TAPE 2,25,KSITE,DATE,TIME,NPTS,DIGR,NPRIME,INST,ICASE
      JPTS=NPTS-1
      IINST=1
      PTS=NPTS+.0001
      RL= PTS*(1./DIGR)
      JFLAG=0
  135 READ INPUT TAPE 2,20,(RHO2(I),THETA2(I),I=1,NPTS)
      CALL ANGSUM(THETA2,NPTS)
      IINST=IINST+1
      IMAGE=0
  140 READ INPUT TAPE 2,18,JINST,NCASE
      IMAGE=IMAGE+1
      IF(XEOF(2))140,145,140
  145 IF(JINST-IINST)140,150,140
  150 IF(NCASE-ICASE)140,155,140
  155 IINST=IINST+1
      IMAGE=IMAGE+(NPTS/6)+1
      READ INPUT TAPE 2,20,(RHO3(I),THETA3(I),I=1,NPTS)
      CALL ANGSUM(THETA3,NPTS)
      PRINT 30
      PRINT 40,(I,RHO2(I),THETA2(I),RHO3(I),THETA3(I),I=1,NPTS)
```

```
      IF(SENSE SWITCH 1)380,200
200   IF(JFLAG)220,205,220
205   RI      =(0.5*RHO2(I))+(0.5*RHO2(2))
      R2          =(0.5*RHO2(NPTS-I))+(0.5*RHO2(NPTS))
      R3        =(0.5*THETA2(1))+(0.5*THETA2(2))
      R4              =(0.5*THETA2(NPTS-I))+(0.5*THETA2(NPTS))
      R5=RHO2(1)
      R6=THETA2(I)
      DO 210 I=2,JPTS
      R7=RHO2(I)
      R8=THETA2(I)
      RHO2(I)=(0.25*R5)+(0.5*R7)+(0.25*RHO2(I+I))
      THETA2(I)=(0.25*R6)+(0.5*R8)+(0.25*THETA2(I+I))
      R5=R7
      R6=R8
210   CONTINUE
      RHO2(I)=RI
      RHO2(NPTS)=R2
      THETA2(1)=R3
      THETA2(NPTS)=R4
      JFLAG=1
220   RI      =(0.5*RHO3(I))+(0.5*RHO3(2))
      R2          =(0.5*RHO3(NPTS-I))+(0.5*RHO3(NPTS))
      R3        =(0.5*THETA3(I))+(0.5*THETA3(2))
      R4              =(0.5*THETA3(NPTS-I))+(0.5*THETA3(NPTS))
      R5=RHO3(1)
      R6=THETA3(1)
      DO 230 I=2,JPTS
      R7=RHO3(I)
      R8=THETA3(I)
      RHO3(I)=(0.25*R5)+(0.5*R7)+(0.25*RHO3(I+1))
      THETA3(I)=(0.25*R6)+(0.5*R8)+(0.25*THETA3(I+I))
      R5=R7
      R6=R8
230   CONTINUE
      RHO3(1)=R1
      RHO3(NPTS)=R2
      THETA3(1)=R3
      THETA3(NPTS)=R4
      PRINT 30
      PRINT 40,(I,RHO2(I),THETA2(I),RHO3(I),THETA3(I),I=I,NPTS)
380   PRINT 30
      IF(SENSE SWITCH 1)430,435
430   PRINT 38,INST,JINST,NCASE,KSITE
      PRINT 35
      PRINT 31
      GO TO 436
435   PRINT 38,INST,JINST,NCASE,KSITE
      PRINT 35
      PRINT 32
436   PRINT 37
      IF(SENSE SWITCH 2)6666,437
437   DO 600,J=1,LEGT
      X=RL/PERIOD(J)
```

```
      IF(X-NPTS)900,900,901
  901 IX=X/NPTS
      M=RL
      X=X-IX*M
  900 NN=X
      IF(NN)452,453,452
  452 MIN=NN-1
      MAX=NN+2
      IF(MIN-1)453,453,454
  453 MIN=1
      MAX=4
      GO TO 456
  454 IF(MAX-NPTS)456,455,455
  455 MIN=NPTS-3
      MAX=NPTS
  456 CALL LAGRAN(RHO2,MIN,MAX,TABLX,TABLY,DEL,X,Y)
      RAMP=Y
      CALL LAGRAN(RHO3,MIN,MAX,TABLX,TABLY,DEL,X,Y)
      CAMP=Y
      IF(RAMP)458,457,458
  457 AMPRAT=0.
      GO TO 459
  458 AMPRAT=RHO1(J)*CAMP/RAMP
  459 CALL LAGRAN(THETA2,MIN,MAX,TABLX,TABLY,DEL,X,Y)
      RANG=Y
      CALL LAGRAN(THETA3,MIN,MAX,TABLX,TABLY,DEL,X,Y)
      CANG=Y
      ANGRAT=THETA1(J)+CANG-RANG
      PRINT 41,PERIOD(J),RL,X,RHO1(J),RAMP,CAMP,AMPRAT,THETA1(J),RANG,
     1CANG,ANGRAT
  600 CONTINUE
  605 IF(IINST-8)140,610,610
  610 IMAGE=IMAGE-1
      GO TO 6666
      DO 620,KBACK=1,IMAGE
      BACKSPACE 2
  620 CONTINUE
      JCASE=JCASE+1
      IF(JCASE-2)130,6666,6666
      END
C     LAGRANIAN INTERPOLATION SUBROUTINE
      SUBROUTINE LAGRAN(BUFFER,MIN,MAX,TABLX,TABLY,DEL,X,Y)
      DIMENSION BUFFER(075),TABLX(4),TABLY(4),DEL(4)
      LL=0
      DO 460 L=MIN,MAX
      LL=LL+1
      TABLY(LL)=BUFFER(L)
      TABLX(LL)=L
  460 DEL(LL)=TABLX(LL)-X
      Y=(DEL(2)*DEL(3)*DEL(4)*TABLY(1))/((DEL(1)-DEL(2))*(DEL(1)-DEL(3))
     1*(DEL(1)-DEL(4)))
      Y=Y+(DEL(1)*DEL(3)*DEL(4)*TABLY(2))/((DEL(2)-DEL(1))*(DEL(2)-DEL
     1(3))*(DEL(2)-DEL(4)))
      Y=Y+(DEL(1)*DEL(2)*DEL(4)*TABLY(3))/((DEL(3)-DEL(1))*(DEL(3)-DEL
```

```
   1(2))*(DEL(3)-DEL(4)))
    Y=Y+(DEL(1)*DEL(2)*DEL(3)*TABLY(4))/((DEL(4)-DEL(1))*(DEL(4)-DEL
   1(2))*(DEL(4)-DEL(3)))
    Y=-Y
    RETURN
    END
    SUBROUTINE ANGSUM(BUFFER,NPTS)
    DIMENSION BUFFER(075)
    PI=3.14159265
    ACCUM=0.
    DO 200,N=1,NPTS
    IF(N-1)114,114,117
114 IF(BUFFER(N))115,116,116
115 THETL=2.*PI+BUFFER(N)
    GO TO 106
116 THETL=BUFFER(N)
    GO TO 106
117 IF(THETM)101,110,112
101 IF(BUFFER(N))105,105,109
105 IF(THETM-BUFFER(N))108,107,104
104 THETL=2.*PI-ABSF(THETM-BUFFER(N))
106 ACCUM=ACCUM+THETL
    THETM=BUFFER(N)
    BUFFER(N)=ACCUM
    GO TO 200
107 THETL=0.
    GO TO 106
108 THETL=ABSF(THETM-BUFFER(N))
    GO TO 106
109 THETL=ABSF(THETM)+BUFFER(N)
    GO TO 106
110 IF(BUFFER(N))111,102,102
102 THETL=BUFFER(N)
    GO TO 106
111 THETL=BUFFER(N)+2.*PI
    GO TO 106
112 IF(BUFFER(N))113,113,105
113 THETL=2.*PI-(ABSF(BUFFER(N))+THETM)
    GO TO 106
200 CONTINUE
    DO 300,I=1,NPTS
300 BUFFER(I)=BUFFER(I)*57.295779
    RETURN
    END
```